INTERNATIONAL ATOMIC ENERGY AGENCY
UNITED NATIONS EDUCATIONAL, SCIENTIFIC AND CULTURAL ORGANIZATION

INTERNATIONAL CENTRE FOR THEORETICAL PHYSICS
34100 TRIESTE (ITALY) - P.O.B. 586 - MIRAMARE - STRADA COSTIERA 11 - TELEPHONE: 2240-1
CABLE: CENTRATOM - TELEX 460392-1

H4.SMR.203 - 15

" SPRING COLLEGE ON GEOMAGNETISM AND AERONOMY "

(2 - 27 March 1987)

" Parameters that can be measured by incoherent scatter "

" Thermal fluctuations in a plasma "

" Scattering of E.M. waves from dielectric density fluctuations "

" Digital techniques used in radar scattering studies of the ionosphere and atmosphere "

presented by :

R.F. Woodman
Instituto Geophysico del Peru
Apartado 3747
Lima 100
Peru

These are preliminary lecture notes, intended for distribution to participants only.

MAX-PLANCK-INSTITUT FÜR PHYSIK UND ASTROPHYSIK

INSTITUT FÜR EXTRATERRESTRISCHE PHYSIK

JANUARY 1984

LECTURE NOTES

ON

INCOHERENT SCATTER TECHNIQUES

originating from

THE EISCAT WINTER SCHOOL

AT OBERSTDORF/GERMANY 1979

8046 GARCHING BEI MÜNCHEN

FOREWORD

The following notes cover the main tutorial lectures given at an introductory course to EISCAT, the European Incoherent Scatter Radar Facility, held at Oberstdorf/Germany from January 8 to 12, 1979 under the sponsorship of the Max-Planck-Gesellschaft. The conveners of the course were G. Haerendel and R. Boswell. 23 lectures were presented on the incoherent scatter technique, on major radar facilities, on r.f. heating, on plasma waves and instabilities and on the geophysical plasma environment. Specific emphasis was given to the operational aspects of EISCAT and how to use it.

Originally, it was intended to issue a volume covering all lectures. However, several major contributions were not turned in, and the plan was abandoned. The fact that the completion of EISCAT was delayed by several years certainly had an impact on the temporal loss of impetus in dealing with the subject. Many of the 46 attendants of the Winter School have meanwhile turned their interest to other tasks or facilities. However, since Fall 1983 regular operation of the UHF system of EISCAT has been possible. Completion of the VHF facility is expected for about one year after the time of this writing. An EISCAT workshop in France in September 1983 has demonstrated a very enthusiastic acceptance of the unique plasma diagnostic capabilities offered by EISCAT, in particular among the young generation. The former Chatanika radar has been moved to Søndre Strømfjord/Greenland in 1983 and is operating very successfully. This development encouraged me to dig out the old lecture notes from Oberstdorf and edit at least the four major contributions on the incoherent scatter technique which have not been superseded by more recent individual publications in the open literature. Taken together, these notes probably present an excellent basis for a first and rather deep penetration into the subject of incoherent scatter.

The final trigger for editing of the lecture notes from Oberstdorf five years later was the organization of a School on Radar Techniques for Remote Sensing of the Atmosphere in Lima/Peru by Ronald Woodman. My apologies for this long delay in printing and for the omission of a few of the supplied manuscripts which were of less educational value and had appeared in somewhat different form elsewhere are combined with my repeated thanks to all lecturers of the EISCAT School at Oberstdorf and my best wishes for a successful school in Lima.

Garching, January 11, 1984

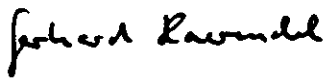

CONTENTS

PARAMETERS THAT CAN BE MEASURED BY INCOHERENT SCATTER

J.V. Evans

Lincoln Laboratory MIT
Lexington, Mass. 02173 , USA

1. INTRODUCTION

A number of earlier papers (Evans, 1969, 1974, 1975 ; Farley, 1970) have described the application of the incoherent scatter (or Thomson scatter) technique to studies of the earth's ionosphere and upper atmosphere. Other reviews have described contributions to studies of the dynamics of the F-region (Evans, 1972), the dynamics of the lower thermosphere (Evans, 1978) or the properties of the thermosphere (Evans et al., 1979). This paper will not attempt to restate all this material in detail, but instead will provide a simple overview of what can be accomplished using the technique.

The classical Appleton-Hartree equation describing the propagation of a radio wave in the ionosphere treats the medium as a continuous dielectric and predicts that, at wave frequencies f substantially higher than the plasma frequency f_p anywhere along the path, there will be no reflected energy. In the absence of density irregularities such as those created by plasma instabilities, this is true to first and second approximation. However, as Thomson (1906) showed, electrons are capable of scattering electromagnetic waves at all frequencies; thus a plasma illuminated by such waves will scatter a small amount of energy back toward the transmitter. Fabry (1928) pointed out that the random motion of the electrons should give rise to a Doppler broadening of the reflected signals and this would cause the intensity of the scattered power to fluctuate about a mean value determined by the sum of the reflected powers (not voltages). For this reasons the scattering has been termed 'incoherent', though a variety of other names (e.g. Thomson scatter, radar backscatter) have been employed.

The electromagnetic energy scattered by an electron into unit solid angle per unit incident flux may be shown to be $(r_e \sin \psi)^2$ where r_e is the classical electron radius and ψ is the angle between the direction of the incident electric field and the direction of the observer. Radar engineers have adopted the convention of defining the cross section of a target as the total scattered energy from an equivalent isotropic scatterer. Using this convention, the radar cross section σ_e of an electron is (Evans, 1969)

$$\sigma_e = 4\pi(r_e \sin \psi)^2$$

$$\approx 10^{-28} \sin^2 \psi [m^2].$$

Since this value is extremely small, it was long thought that the incoherent scattering of the ionospheric electrons could not be detected by modern radio methods. The first to contest this view was Gordon (1958) who showed that by constructing a parabolic reflector antenna of 1000-foot diameter and coupling this to a high-power VHF radar system, it should be possible to detect the back-scattered signals. This could then be exploited as a means of probing the distribution of the electrons throughout the ionosphere and measuring their temperature T_e (from the Doppler broadening of the signals).

The first reported detection of incoherent scattering by the ionosphere was made by Bowles (1958, 1961) using a newly completed high-power VHF radar system intended for meteor studies at Havana, Illinois. Bowles made the important discovery that the Doppler broadening of the signals was considerably

less than expected from the random thermal velocity $\bar{v}_e$ of the electrons ($\bar{v}_e = \sqrt{2k\,T_e/m_e}$, where k is Boltzmann's constant, T_e is electron temperature and m_e the electron mass). Bowles correctly deduced that this was caused by the presence of the ions in the plasma. This observation prompted a number of theoretical investigations of the phenomena, which despite the different approaches employed, yielded the same results.

The theory showed that for meter and decimeter length radio waves used to observe incoherent scatter from the ionosphere, the principal reflections arise from density irregularities in the electron gas impressed by the presence of the ions, and accordingly, exhibit a Doppler broadening that is governed by the random motion of the ions (and is, therefore, considerably less than had been anticipated). This result had important consequences for the signal-to-noise ratio, since this is determined, in part, by the receiver bandwidth. Since the bandwidth need only be wide enough to accommodate all the echo power, a considerable improvement in the signal-to-noise ratio is achieved by narrowing the receiver bandwidth to just match the ion Doppler broadening. Consequently, it is possible to obtain useful incoherent scatter returns from the ionosphere with a radar considerably smaller than that contemplated by Gordon (1958).

2. INCOHERENT SCATTER THEORY

2.1. Spectra

The scattering of radar signals by density irregularities in the ionosphere is illustrated in Fig. 2. The signals will be scattered through an angle ϕ by the presence of irregularities having a spacing (measured along the perpendicular bisector of the angle between the incident and scattered waves) of λ_p where

$$\lambda_p = \frac{\lambda}{2 \sin(\phi/2)} \qquad (1)$$

in which λ is the radar wavelength. Equation (13) is simply the Bragg scattering formula for a crystal. Thus radar scattering measurements may be thought of as providing a Fourier analysis of the medium to determine the intensity of density fluctuations of scale λ_p.

As shown by Fejer (1960), Dougherty and Farley (1960), Salpeter (1960a,b), and Hagfors (1961) ions are capable of organizing electron density fluctuations in the plasma over scales larger than the electron Debye length D_e where

$$D_e = 69\sqrt{T_e/N\ m^3}. \qquad (2)$$

Accordingly, the ions play an important role in the scattering when $\lambda_p \gg D_e$. The parameter $\alpha = 2\ D_e/\lambda_p$ may be used to describe

the ratio between the electron Debye length and the wavelength. (For backscatter experiments $\lambda_p = \lambda/2$ and the parameter $\alpha = 4\pi D_e/\lambda$.)

For the case $\alpha \gg 1$ the scattering will be from the individual electrons as envisaged by Fabry and Gordon. Under these circumstances the Doppler broadening will cause the echoes to have a Gaussian-shaped frequency power spectrum with a half power width W_e of

$$W_e = 1.42\ \Delta f_e \qquad (3)$$

where

$$\Delta f_e = \frac{\bar{v}_e}{\lambda_p} \qquad (4)$$

is the Doppler shift of an electron approaching the radar at the mean thermal speed of the electrons $\bar{v}_e (= \sqrt{2k\ T_e/m_e})$. For backscatter Δf_e becomes

$$\Delta f_e = \frac{11\ (T_e)^{1/2}}{\lambda}\ [\mathrm{kHz}]. \qquad (5)$$

In the ionosphere below ~ 2000 km D_e is usually less than 1-2 cm. Thus for decimeter or meter-wave radars $\alpha \ll 1$. Under these circumstances the scattering may best be thought of as

arising from the transient local increases in electron density surrounding each ion. As such, the Doppler broadening W_i is commensurate with the ion thermal speed

$$W_i \simeq 2\Delta f_i \tag{6}$$

where

$$\Delta f_i = \frac{\bar{v}_i}{\lambda_p} \tag{7}$$

is the Doppler shift of an ion approaching at the mean speed $\bar{v}_i$ of the ions. For backscatter experiments when the plasma contains O^+ ions (7) reduces to

$$\Delta f_i = 65(T_i)^{1/2}\,[\mathrm{Hz}]\,. \tag{8}$$

Figure 2 provides a sketch of the spectrum for the case $\alpha \ll 1$ and $T_e = T_i$. It can be seen that for $\alpha \to 0$ the spectrum narrows and becomes double humped. A small amount of energy associated with free electron scattering then appears in two lines displaced above and below the frequency of the radar by an amount approximately equal to the local plasma frequency. These are termed 'plasma lines' and may be thought of as density fluctuations with scale λ_p arising as a result of the (electrostatic) interaction of the electrons with themselves.

The spectrum of Figure 2 may be interpreted as reflections from sound waves in the ion gas with wavelength λ_p that are approaching and receeding from the radar with the mean thermal speed of the ions $\bar{v}_i$. Actually the scattering is from the electrons, and the reflections really represent the ability of the ions to organize density fluctuations among the electrons through electrostatic forces. As might be expected the coupling between the ions and electrons depends upon their relative speeds and thus the spectrum changes shape when $T_e > T_i$ as is found to be the case in the ionosphere. This is illustrated in Figure 3 for the cases $1{:}0 \leq T_e/T_i \leq 4{:}0$.

It can be seen from Figure 3 that for $T_e > T_i$ the wing in the spectrum grows more pronounced as a consequence of the fact that the ion accoustic wave is now subject to less damping. In addition the spectrum is seen to broaden. This last effect is due to the fact that the overall doppler broadening depends up the ratio $(T_e/T_i)^{1/2}$. This is illustrated in Figure 4 where spectra for $T_e/T_i = 1.0$, 2.0 and 3.0 are plotted for O^+, He^+, and H^+ on a scale with units of $\Delta f_i\ (T_e/T_i)^{1/2}$. It can be seen that the spectra have shapes that do not depend greatly upon the ion. Combining Eq. 8 with $(T_e/T_i)^{1/2}$ we see that the density peak occurs at

$$\Delta f = 65\ (T_e)^{1/2}\ [\mathrm{Hz}] \tag{9}$$

That is we can think of the scattering as being from sound waves in a gas of fictitious particles having the scattering cross section and temperature of the electrons and the mass of the ions.

The spectra of Figure 4 when plotted on an absolute frequency scale (e.g. one normalized in units of Δf_e) are shown in Figure 5. Since He^+ ions are 4 times lighter than O^+ ions their spectra are twice as wide [Since $\bar{v}_i = (2k\,T_i/m_i)^{1/2}$ in Eq. 7] . Similarly the H^+ spectra are twice as wide as those of He^+.

2.2. Total Power

The volume scattering cross section for the case $\alpha >> 1$ is simply $N_e\tau_e$ where N_e is the electron concentration. That is the total reflected power depends upon the density and not the square of the density as in the case of coherent reflections. This is because the random thermal motion of the particles causes the phases of the signals scattered by each electron to be unrelated one to another, and hence the powers add <u>not</u> the voltages.

For a vertically directed radar it may be shown that the total reflected power P_s depends upon

$$P_s = P_t \cdot (N_e \sigma_e \frac{c\,\tau}{2}) \frac{A}{h^2} \qquad (10)$$

where P_t is the peak transmitted power, $c\tau/2$ is the height occupied by the exploring pulse (length τ seconds), A is the collecting area of the antenna and h is the height from which the scattering occurs. Note that P_s does not depend upon the gain of the antenna. This is because increasing the antenna

gain, increases the power incident on each electron but reduces the number of electrons illuminated by a compensating factor.

The theory shows that when $\alpha \to 0$ the total scattering cross section (i.e. the area under the curve of Figure 2) becomes $N_e\tau_e/2$. As can be seen from Figure 3 the area under the curves becomes still smaller for $T_e > T_i$.

The scattering cross section per electron of the plasma is shown in Figure 6 for O^+ and H^+ ions. An approximation due to Buneman (1962) is also shown, viz

$$\sigma \simeq \frac{\sigma_e}{(1 + T_e/T_i)} \quad , \alpha = 0 \; . \qquad (11)$$

It can be seen that this holds for $T_e \leq 3\,T_i$. The increase in the cross section for very large valves of T_e/T_i arises because the Debye length is increasing causing the assumption $\alpha \to 0$ to be violated and the spectrum to broaden as $\alpha > 1$ and the total cross section to tend towards $\sigma = \sigma_e$.

In practice values T_e/T_i outside the range $1.0 < T_e/T_i < 3.0$ are rarely if ever encountered in the ionosphere so that Eq. (11) provides a good estimate of the dependence of the echo power with T_e/T_i provided $\lambda_p >> 4\pi D_e$ (i.e. $\alpha \to 0$). At great heights in the F-layer the electron density decrease and T_e increases causing D_e to become $\gtrsim 1$ cm. It may then no

longer be possible to assume $\alpha \to 0$ and one must be concerned with the effect of a finite Debye length. Figure 7 shows the effect on the ion line of increasing α , in the case $T_e/T_i = 1.0$. It can be seen that the power under the curves decreases as $\alpha \to$ large. The power reflected in the ion component then varies as N_e where

$$\sigma \approx \frac{\sigma_e}{(1+\alpha^2)\,(1+\alpha^2+T_e/T_i)}, \quad \begin{matrix} \alpha \lesssim 1.0 \\ \frac{T_e}{T_i} \lesssim 3.0 \end{matrix} \qquad (12)$$

(Buneman, 1962).

3. MEASUREMENTS OF N_e, T_e, T_i

3.1. Electron Density N_e

Using a pulsed radar it is relatively straightforward to measure the echo power P_s as a function of height h. Figure 8 shows a typical A-scope display. The receiver contributes an amount of unwanted noise power P_n which can be estimated from samples taken as $h \to$ large. Since both P_s and P_n are randomly fluctuating the uncertainty in their estimates depends as

$$\Delta P_n = \frac{P_n}{\sqrt{m}} \qquad (13)$$

where m is the number of independent estimates. The uncertainty of samples of power taken in the region where signal is present is

$$\Delta P = \frac{P_s + P_n}{\sqrt{n}} \qquad (14)$$

where n is the number of radar sweeps. By sampling the noise at many ranges (i.e. making $m \gg n$ it is possible to reduce the uncertainty in P_n in (14) so that useful estimates can be made of the echo power even when $P_s \ll P_n$.

From Eq. (10) it can be seen that

$$N_e \propto P_s\, h^2\, \sigma \qquad (15)$$

so that by allowing for the h^2 dependence it is possible to recover a profile of electron density. Figure 9 shows an example of such a profile obtained using σ = 100 μsec ($c\tau/2$ = 15 km) pulses. The increase in uncertainty with altitude is evident. To overcome this it is usually necessary to employ longer pulses to explore increasing heights. In this reduction it was assumed that τ = const. (i.e. T_e/T_i = const, $\alpha \to 0$). As such the profile may be in error if T_e/T_i varies with altitude. It is usual to call such measurements "power profiles".

To establish the absolute density scale one may make absolute power measurements and employ a carefully calibrated radar, or one may use an ionosonde to determine the plasma frequency f_p at the maximum of the layer.

The measurements of Figure 9 were made by transmitting right-hand circularly polarized waves and receiving the left-hand reflected signal. By using linearly polarized waves it is possible to measure N_e vs h by observing the Faraday rotation of the waves as a function of reflected height h (Evans, 1969). This method is an absolute one but tends to become inaccurate at $h >> h_{max}$ where the rate of change of the Faraday rotation becomes small.

Actual measurements of the spectra of the signals reveal that $T_e > T_i$ in the F-region during the day-time, requiring that a connection be applied (Eq. 11) for the variation of σ with T_e/T_i in order to get accurate results.

3.2. Electron and Ion Temperature

By measuring the spectrum (or the autocorrelation function of the signals) as a function of height it is possible to measure N_e, T_e and T_i simultaneously as illustrated in Figure 10. In comparing the observed and measured spectra one must allow for instrumental smearing caused by the finite length of the transmitter pulses and/or the width of the filters in the receiver.

As can be seen from Figure 7 the effect of $\alpha \to 1.0$ is to change the shape of the spectrum making it difficult to

recover T_e/T_i. The value β for T_e/T_i deduced from the spectrum neglecting this effect and the true value T_e/T_i are related approximately by

$$\frac{T_e}{T_i} = (1 + \alpha^2)\ \beta\ ,\ \alpha < 1 \qquad (16)$$

and

$$\sigma = \frac{\sigma_e}{1 + \beta} \qquad (17)$$

thus by successive approximations it is possible to correct the power profile for the dependence upon T_e/T_i and α (Eq. 17) and thereby deduce N_e and hence estimate α and obtain correct estimates of T_e/T_i (Eq. 16). The measurements of Figure 10 were secured in this way. An alternative approach presently employed at Millstone is to use a computer to search for the best matching spectrum for the case $\alpha \neq 0$, $T_e/T_i > 1.0$ using the observed echo power and f_0F2 to establish one of the unknowns ($N\sigma$).

3.3. Contour Plots

The measurements of Figure 10 took 30 minutes to complete. By making such observations over 24 hours it is possible to construct countour diagrams of N_e, T_e, and T_i vs height and time. Figure 11a-c shows such contours obtained for Millstone where the data points have been fitted to a smooth (polynomial) surface in a least mean square sense. The method has been described by Evans and Holt (1976) and provides smoothly varying estimates of all three quantities as functions of both height and time. Considerable effort has been devoted

to examining the manner in which each of the three parameters depends on the other two, and has been the subject of many papers (e.g. Evans, 1965)

4. DERIVED THERMAL PROPERTIES

4.1. Introduction

The discovery that during the daytime $T_e > T_i$ prompted considerable interest and study of the thermal properties of the ionosphere and this work has been reviewed by Banks (1969) among others. Here we summarize some of the heat transfer rates that can be deduced from the measurements of N_e, T_e, T_i described in Section 3.

In the daytime the creation of ionization by absorption of photons serves to heat the thermosphere. Fast photoelectrons are created which carry away any excess energy of the original photon over the amount needed to ionize the atom or molecule. The excess energy is lost by collisions with neutrals and by exciting vibrational or rotational states of some molecules (e.g. N_2). In this way most electrons are slowed to < 1 eV. This remaining energy is given to the electron gas via Coulomb encounters serving to heat it. This process is complicated to calculate because many photoelectrons travel considerable distances before losing all their energy. They can for example escape the local ionosphere and travel along the flux tube to the conjugate point losing energy all along the way. In this manner the entire flux tube is heated and develops a temperature maximum at the equator.

Figure 12 shows early efforts to account for the observed behavior of the electrons and ions by adjusting the total heat input Q into the electron gas and the flux of heat Q_M from the magnetosphere at 1000 km.

It can be seen that the electrons become hotter than the ions above about 140 km. The ions by contrast remain close to the neutral temperature T_n until about 300 km. This is because the two species have like masses and hence collisions between them can effectively transfer heat. Above about 300 km the ions assume a temperature intermediate between T_e and T_n because they are heated by the electrons (via Coulomb encounters) at a rate that they can no longer lose to the neutrals because collisions are no longer frequent.

4.2. Protonospheric Heat Flux

The existence of a positive temperature gradient in T_e (Figure 10) indicates the existence of a downward flux of heat conducted by the electron gas. The value of this flux depends only on the electron temperature and its gradient

$$Q_m \propto T_e^{5/2} \frac{d T_e}{dz} \sin I \qquad (18)$$

where I is the dip angle of the magnetic field. In Figure 13 it was necessary to set $Q_m = 4 \times 10^9$ eV/cm^2/sec to match the observed temperatures.

Figure 14 shows values of Q_M computed from average temperature profiles constructed for 5-hour intervals near noon and midnight at Millstone Hill in 1969. During the day the flux was typically ~ 5×10^9 eV/cm^2/sec and showed little seasonal variation (Figure 14a). At night there is a marked variation because at Millstone the conjugate point remains sunlit in winter. The large peak in October 1967 was a result of a magnetic storm which caused the ring current to be driven in as far as the L-shell (L = 3.2) for Millstone and greatly increased the heating of the flux tube (probably through ion-cyclotron damping). Thus we see that Q_M can be a sensitive indicator of ring current heating - especially at night.

The results of Figure 14a show that the winter day values of Q_m are slightly larger than the summer ones and this appears to be a consistent feature as can be seen in Figure 15. In this figure the average of 6 months data for summer and winter are plotted for 5 years. It is clear that the flux increases with sunspot number (or solar flux) and this presumably reflects a greater photoelectron escape at sunspot maximum.

4.3. Heat Transfer Between Electrons and Ions

Heat is transferred between the electrons and ions at a rate Q_{ei} where

$$Q_{ei} \propto \frac{N_i N_e (T_e - T_i)}{T_e^{3/2}} \qquad (19)$$

Since above the D-layer $N_i = N_e$ all the quantities in (19) can be determined by radar and Q_{ei} computed quite reliably.

4.4. Heat Transfer Between Ions and Neutrals

Heat given to the ions by the electrons is transferred to the neutrals and conducted to lower altitudes. The transfer rate to atomic oxygen (which is the dominant species in the F-region) proceeds at a rate

$$Q_{in} \propto N_i N(O) (T_i - T_n) (T_i + T_n)^{1/2} . \qquad (20)$$

4.5. Exospheric Temperature T_∞

At F-region altitudes an estimate can be made of the neutral temperature T_n by setting

$$Q_{ei} = Q_{in} . \qquad (21)$$

This is possible because local heat transfer is much more important than conduction for the ions. This yields

$$T_i - T_n = \frac{4.82 \times 10^7 \, N_e \, (T_e - T_i)/T_e^{3/2}}{6.6 \, N(N_2) + 5.8 \, N(O_2) + 0.21 \, N(O) \, (T_i + T_n)^{1/2}} \quad (22)$$

The neutral number densities required to solve Eq. (22) may be obtained from an empirical model of thermosphere, e.g., Jacchia (1965). In this approach T_n initially is set to T_i in the denominator on the right hand side of Eq. (22), and in a second iteration it is set to the value computed from the first iteration, so that the difference $T_i - T_n$ is estimated. If the solution is obtained for an altitude > 400 km, the value of T_n obtained may be taken equal to the exospheric temperature with little error. Alternatively, T_n may be estimated at several altitudes in the range 250-500 km from the radar observations, and them employed to give several independent estimates of this exospheric temperature, assuming a Bates profile

$$T_n = T_\infty - (T_\infty - T_0) \exp [-s \, (h - 120)] \quad (23)$$

where s is the inverse scale height parameter and h the height in km. T_0 is the temperature at the lower boundary (120 km). In this approach errors in T_0 of $\pm$ 100°K and in s of $\pm$.005 introduce less than $\pm$ 3% errors in T_∞ . Similarly large errors in N(O) (in Eq. 22) can be tolerated since they contribute only to the correction to be applied to T_i to get T_n.

The alternative method of obtaining the exospheric temperature utilizes the fact that atomic oxygen is the most abundant neutral species in the upper thermosphere (> 300 km). Accordingly, it is valid to simplify Eq. (1) by including only the term representing the heat transferred to atomic oxygen. Then, given radar estimates of T_e, T_i and N_e, there remain only two unknowns, namely, N(O) and T_n. Assuming N(O) to be in diffusive equilibrium and T_n to follow the Bates profile (Eq. 23), one can solve by regression analysis for T_∞, s and $N(O)_{z_{ref}}$, where z_{ref} is the reference altitude for the diffusive equilibrium distribution of atomic oxygen. In this second method, it is preferable to employ radar measurements at many altitudes in the thermosphere, say between 100 and 500 km, obtained with good height resolution (see Figure 16). This is important since one must solve for three parameters simultaneously, and may as well solve for a fourth parameter, namely T_0, to anchor the temperature profile adequately. The method may be applied successfully during the daytime hours when there is adequate energy imbalance, i.e., $(T_i - T_n)$ is large, say 100-200°K. At night, the first method must be used, but then is almost independent of N(O) since $T_i \approx T_n$.

The principal source of random error is introduced by the experimental uncertainty in determining T_i, since errors in the determination of N_e and T_e contribute only errors in the correction applied to T_i to obtain T_n. With care, T_i can be determined to an uncertainty of < $\pm$5% from observations extending over several minutes. By combining observations made at several altitudes, the error in the derived estimate of T_∞ will be less. Systematic errors therefore probably have been a more serious limitation in most of the measurements made to date.

Figure 17 shows values of T_∞ obtained vs local time for different times of year. It is clear that the temperature maximizes near 1500 hrs in winter, 1600 hours at equinox and 1700 hours in summer. Results for T_∞ from all the incoherent scatter stations have been incorporated into the Mass Spectrometer/Incoherent Scatter (MSIS) model of the neutral atmosphere of Hedin et al. (1977) and Evans et al. (1979) have reviewed the contributions of incoherent scatter to our understanding of the diurnal, seasonal and sunspot cycle variations of the temperature of the thermosphere.

4.6. Neutral Temperature Below 300 km

The solution for the neutral temperature below 300 km (Figure 16) is aided by the fact that between about 115 km and 135 km $T_e = T_i = T_n$ and in this interval O_2^+ and N_2^+ are the dominant ions. By adopting a mean ionic mass $m_i = 31$ or 31.5 amu it is possible to reduce the spectra obtained in this region and obtain reliable estimates of temperature. This work has been reviewed by Evans (1978), and has contributed considerably to the study of propagating tides.

5. PROPERTIES OF THE NEUTRAL ATMOSPHERE

5.1. Atomic Oxygen

In Figure 16 a solution was obtained for the abundance of atomic oxygen at 400 km. This depends upon the observed rate

of change of ion temperature with height and is the parameter least reliably obtained. Nevertheless the French group have attempted to determine $N(O)_{400}$ by this method (Bauer et al., 1970, Alcayde et al. (1971). Figure 18 compares results obtained by the method with the OGO-6 and Jachia 71 models. While it appears that the method yields reasonable results near midday the values at sunrise and sunset seem too low. The reason for this discrepancy is not known.

5.2. Molecular Nitrogen

Below about 115 km (depending somewhat upon the radar wavelength) collisions between ions and neutrals begin to modify the shape of the spectrum. This effect, which was ignored in Section 2 is illustrated in Figure 19 for various values of ψ_2 where

$$\psi_i = \frac{\lambda_p}{2\pi \ell_i} \qquad (24)$$

where ℓ_i is the mean free path of the ions.

As can be seen the effect of collisions is to narrow the spectrum eventually causing it to be Gaussian in shape at an altitude below 100 km.

In the region 115 to 100 km approximately it is possible to estimate both $T_i (= T_e = T_n)$ and the ion neutral collision

frequency ν_{in}. This may be used to estimate the abundance of the dominant species (N_2) at these altitudes via

$$\nu_{in} = 0.9 \times 10^{-15} N(N_2) \quad [sec^{-1}] \qquad (25)$$

(Wand and Perkins, 1968). Figure 20 shows estimates of the N_2 concentration at 100 km observed in France vs local time for six days in 1969. The time variation probably is caused by diurnal and semidiurnal tides which dominate the behavior of the thermosphere at this altitude (Evans, 1978). Figure 21 shows the seasonal variation in N_2 concentration at 100 km altitude. It is clear that these types of measurements can contribute greatly to models of the neutral atmosphere but to-date they have not been made at enough stations to warrant this.

6. IONIC COMPOSITION

6.1. Introduction

Over some altitudes of the ionosphere mixtures of ions are present. These complicate the interpretation of the spectra from these regions. Where only a single ion is present one may determine what the species is if the ion temperature is known (cf. Figure 5). Usually, however, the reverse process is employed, i.e., based on mass spectrometer results it is assumed that:

$90 < h < 140$ km	O_2^+ and N_2^+ ions present
	$m_i = 31.5$ AMU
$200 < h < 1000$ km	O^+ ions present
	$m_i = 16.0$ AMU
$h > 1500$ km	H^+ ions present
	$m_i = 1.0$ AMU

so that temperatures can be obtained for these regions unambiguously. We discuss next what can be done in the intermediate regions where mixtures are encountered.

6.2. Light Ions

Above about 600 km depending upon time of day and latitude He^+ and H^+ ions are encountered. Figure 22 shows how the spectrum changes shape for a mixture of O^+ and H^+ ions when $T_e/T_i = 1.5$. For mixtures of O^+ and either He^+ or H^+ it is usually possible to determine T_e, T_i and the percentage abundance of the light ions. In the more general case when all three ions are present (illustrated in Figure 23) it is difficult to separate the relative abundance of each unless T_e/T_i is known. Thus, for example, at Arecibo it becomes difficult to deduce the ionic composition except at night when it can be assumed $T_e = T_i$. Figure 24 shows results obtained for late evening in February 1972.

At the latitude of Millstone it appears (from mass spectrometer measurements) that H^+ is always much more abundant than H_e^+. Accordingly, it is possible to solve for the H^+ abundance (by assuming H_e^+ % = 0) even when T_e/T_i is not known. Figure 25 shows results for a winter night. During the day at Millstone and at night in summer only a small percentage of H^+ is detectable (~ 1-2%) near about 800 km. This is because at such times the H^+ flux is close to its limiting escape value (Under such conditions the H^+ concentration peaks near 800 km and then decreases again as shown in Figure 26. At such times O^+ may be the dominant ion to altitudes h > 2000 km.

6.3. Heavy Ions

The transition between O^+ ions and molecular species (NO^+ and O_2^+) observed from rocket measurements at various times is illustrated in Figure 27. Unfortunately, mixtures of these ions produce spectra which are indistinguishable from spectra produced by a single species with an appropriate change in temperature.

The best method for solving for the ion composition in the region 140 < h < 240 km appears to be that employed by Oliver (see Evans et al., 1979) in which appeal is made to the photochemical theory for this region. This describes the shape of the transition curve with only two free parameters namely the height of 50% O^+ (z_{50}) and the optical depth of the atmosphere at this level τ_{50}. It now becomes possible to solve for z_{50} and τ_{50} if it is assumed that the ion and neutral temperatures are the same in this region and

given by the Bates formula (Eq. 23). That is all the spectra obtained between 120 ≤ h ≤ 500 km are used to solve for T_∞, T_o, s, $N(O)_{400}$, z_{50} and τ_{50}. Figure 28 illustrates the basis of the method. Composition curve a clearly produces unrealistic temperatures, while curve b is consistent with expectation. Figure 29 shows results obtained for one day by this method. Some of the results of an analysis of data gathered at St. Santin de Meurs using this approach have been given by Evans et al. (1979).

7. MEASUREMENTS OF NEUTRAL WINDS

7.1 Introduction

All the measurements discussed thus far (in Sections 3-6) depend upon measuring only the shape of the signal spectrum, or equivalently the autocorrelation function (i.e., its Fourier transform). Stated differently if $a(\tau)$ and $b(\tau)$ are respectively the real and imaginary parts of the echo autocorrelation function the information on the shape is contained in the amplitude part $p(\tau)$ where

$$p(\tau) = \sqrt{a^2(\tau) + b^2(\tau)} \qquad (26)$$

If the spectrum is truly symmetric and centered exactly on the radar frequency then $b(\tau) \rightarrow 0$. If, however, the plasma is moving as a whole the spectrum will exhibit an overall doppler shift as illustrated in Figure 30 where the shift Δf_d is given by

$$\Delta f_d = \frac{v_d}{\lambda_p} \quad . \qquad (27)$$

In the case of monostatic measurements the drift velocity observed is the component along the radar line-of-sight. For bistatic measurements it is the component along the perpendicular bisector of the two beams (i.e. the direction OP in Figure 1).

If the autocorrelation has been measured the doppler shift can be recovered from the rate of change of the phase ϕ with τ , where

$$\Delta f_d = \frac{1}{2\pi} \left(\frac{d\phi}{d\tau}\right)_{av} \qquad (28)$$

in which

$$\phi = \arctan\left(-\frac{b(\tau)}{a(\tau)}\right) \qquad (29)$$

7.2. E Region Winds

At altitudes below about 115 - 120 km where the ion neutral collision frequency is larger than the ion gyrofrequency it is possible for neutral winds to drive ions across the field lines. Under these circumstances the ion motion serves as a tracer allowing neutral winds at these altitudes to be determined. Figure 31 shows observations of the southward component of the horizontal wind at 103 km observed over Millstone Hill on several days in 1976. The results show clear evidence of semi-diurnal tides and have been reviewed by Evans (1978).

7.3. F Region Winds

In the F region neutral winds are thought to be unable to drive the ions across field lines. This is because such motion would produce a Hall drift thereby polarizing the layer. The polarization field would be communicated to the E region where it will be shorted. At the equator (and perhaps at other latitudes at night) the polarization field may not be shorted in which case the ions will move as a result of the induced polarization electric field. When they have achieved the same speed as the wind they no longer experience any acceleration (i.e. in the rest frame of the wind they see no field), and thus the wind does set the ions moving with the same speed and direction.

Except under these unusual circumstances a neutral wind U in the magnetic meridian serves only to drive ions upwards or downwards along the field line as shown in Figure 32 . In the daytime neutral air winds blow polewards (i.e. away from the equator) tending to drive the F layer to lower heights while the reverse happens at night.

The force exerted by the component of the neutral wind along the field line must compete with the tendency of the plasma to diffuse downwards under the influence of gravity at a rate that depends upon the ambipolar diffusion coefficient D, and the pressure gradients in the plasma. This diffusion velocity v_D proceeds at a rate (Vasseur, 1969 a,b).

$$v_D = - D \sin^2 I \left(1 + \frac{T_e}{T_i}\right) \left[\frac{1}{N_e}\frac{d N_e}{dz} + \frac{1}{T_e+T_i} \cdot \frac{d(T_e+T_i)}{dz} + \frac{1}{H_i}\right] \quad (30)$$

where H is the scale height the plasma would adopt in diffusive equilibrium

$$H_i = \frac{k (T_e + T_i)}{m_i g} \quad (31)$$

where k is Boltzmann's constant. In (30) all the parameters needed to compute v_D are known except D which depends upon the neutral density. However, by appeal to a model atmosphere D can be determined. The observed vertical velocity v_z may then be used to compute the horizontal neutral wind U_x in the magnetic meridian via

$$v_z = U_x \cos I \sin I + v_D \quad . \quad (32)$$

Eq. (32) neglects any vertical motion imparted to the ions by electric fields (See 9.). These can be measured if the drift velocity perpendicular to the field line B in the magnetic meridian can be measured. Alternatively, if the velocity parallel to the field B is observed ($v_\parallel$) Eq. (32) and (31) can be reformulated to the drift velocity in this direction which is independent of any electric field effects.

Figure 33 shows (top panel) measured values of v_z over Millstone at 300 km. In the center panel the vertical diffusion velocity v_D computed from the measured values of N_e, T_e, T_i (via Eq. 30) is shown. The lower panel shows the wind U_x computed via (32). Figure 34 shows winds computed for a winter and summer day. These exhibit differences resulting from the variation of the global heating with season.

8. F REGION VERTICAL ION FLUXES

8.1. Introduction

Vertical fluxes of the ionization in the F region arise from the competing effects of production, loss, and diffusion. As noted above winds can modify the rate of diffusion. In order to measure the wind velocity it is necessary to do so at the altitude where production loss and diffusion are all comparable, i.e. at or somewhat below the F region peak.

8.2. Velocities Above h_{max} F2

Well above the F region peak diffusion dominates, i.e. the diffusion coefficient D in (30) becomes very large making it difficult to determine v_D. Accordingly, at these altitudes measurements of v_z tend to be sensitive primarily to he effects of the growth and decay of the layer at down and sunset. This is illustrated in Figure 35 for an altitude of 600 km. Besides the large vertical velocities when the layer is growing or decaying one can also see short period fluctuations at are due to gravity waves which produce travelling ionospheric disturbances (TIDs) which introduce fluctuations in the neutral wind velocity alternately raising and lowering the layer as a whole.

8.3. F Region Vertical Fluxes Under Equilibrium Conditions

Measurements made near noon when the layer is in equilibrium allow the vertical fluxes to be observed that depend only on production and loss. Figure 36 shows average midday fluxes

over Millstone for summer and winter. Below ~ 600 km ionization diffuses downwards from the level where it is created to levels below 300 km where it is lost. Above this altitude O^+ diffuses upwards to a level where it charge exchanges with H^+ and so supports an escape flux. The escape flux observed in Figure 36 appears to be ~ 5×10^7 ions/cm^2/sec but depends upon sunspot cycle (and hence the neutral H abundance).

9. ELECTRIC FIELDS AND CURRENTS

9.1. Introduction

In the F region it is believed that plasma moves across field lines only as a result of an electric field-induced Hall drift. The perpendicular velocity is

$$\vec{v}_\perp = \frac{\vec{E} \times \vec{B}}{B^2} \quad . \qquad (33)$$

This is the so-called "frozen field" concept. Evidently if three components of the drift velocity can be measured for the plasma in one region (e.g. using three intersecting beams) it will be possible to determine orthogonal components of the electric field. With a monostatic radar it is usually not possible to observe normal to $\vec{B}$ and in any event the same region of the plasma can be viewed from only one direction. It then becomes necessary to assume spatial uniformity over the region under study. This is clearly undesirable where the field might be varying rapidly (e.g. in the vicinity of an auroral arc) but after one component dominates and can be measured in one place continuously.

It is usually considered that the plasma moves according to (33) at all altitudes in the F region above about 160 km, hence $\vec{E}_\perp$ is the one parameter that can be measured at any altitude.

9.2. Electric Field Measurements

The earliest observations of electric field were those made over Jicamarca where the E-W polarization field established by dynamo action in the E region produces vertical drifts in the F region (i.e. in the $\vec{E} \times \vec{B}$ direction). These results are illustrated in Fig. 37. Subsequently electric fields have been measured at all other latitudes and this capability of the incoherent scatter technique is of great value at auroral latitudes allowing the convection of the magnetosphere to be studied by means of ionospheric plasma drift measurements.

9.3. E Region Measurements

In the altitude between about $110 < h < 160$ km ions respond to bothneutral winds and to electric fields. Since, however, $E_\perp$ can be determined from F region observations the E region neutral winds $(\vec{u})_E$ can be determined from observations of horizontal ion drifts at these altitudes.

Given the neutral air motion it is possible to compute the electric field seen by the ions in the rest frame of the air, provided that the ratio of the ion neutral collision frequency ν_{in} to the ion gyro-frequency w_i is known. This requires appeal to a model for the neutral atmosphere.

By appeal to the same neutral air model and the measured electron density profile N_e it is possible to deduce the Hall σ_H and Pedersen σ_P conductivities. Knowledge of the electric field in the rest frame of the air then allows the calculation of the currents that must flow. Figure 38 shows results obtained by Harper (1977) for the currents flowing over Arecibo near noon as a consequence of the combined effect of the winds and electric fields. The winds in this case are of tidal origin and hence rotate with altitude. The broken line shows the current that would have been calculated neglecting the effects of the winds. The expressions for these currents are of the form

$$J_x = \frac{\sigma_P}{\sin I} (E_x - U_y B \sin I) + \frac{\sigma_H}{\sin I} (E_y + U_x B \sin I) \quad . \quad (34)$$

The currents flowing in the E region at auroral latitudes (auroral electrojet) are of particular significance for heating the thermosphere (Joule heating). The rate of heating can be computed from $\sigma_P (E^M)^2$ where E^M is the electric field in the rest frame of the air (i.e. $E_x - U_y B \sin I$).

10. RECAPITULATION

Figure 39 shows a diagram that traces how the various parameters that have been discussed are derived. In this diagram N_e^M is the electron density "power profile", i.e. uncorrected for altitude variations of T_e/T_i or α. It represents the only parameter that can be determined by measuring only the total power versus height P(h). All other parameters require measurements of the signal spectra (or equivalently their autocorrelation functions) versus height. T_e, T_i, ν_{in} and ion composition information depend only on the shape of the spectrum. They can be used to obtain thermal properties (e.g. Q_M, T_∞) and neutral densities (e.g. $N(O)_{400}$ $N(N_2)_{100}$) as described in Sections 4 and 5. These contribute to defining a model for the neutral atmosphere which together with measurements of N_e, allows the E region conductivities to be calculated (σ_P, σ_H).

Also shown in Figure 39 is the recovery of information on the spectrum F(E), mean energy $\langle E \rangle$, and heating rate Q_E of particles precipitating into the E region by unfolding the production function g(h) needed to sustain E region ionization at night (at auroral latitudes). Much use has been made of this capability at Chatanika and from these data attempts have been made to estimate the parallel current $J_\parallel$ into auroral arcs.

Measurement of the overall doppler shift of the spectra (or equivalently the rate of change of phase in the autocorrelation function) provides estimates of ion drift. The component parallel to $\vec{B}$ ($v_\parallel$) in the F region when combined with estimates of the diffusion velocity v_D provides a measure of the horizontal thermospheric wind in the magnetic meridian.

Measurements of the components perpendicular to $\vec{B}$ provide estimates of the F region polarization electric field $\vec{E}_\perp$. When combined with measurements of the horizontal drift $\vec{v}_h$ of the ions in the E region these allow the E region neutral wind $(\vec{u})_E$, E region currents and Joule heating to be calculated (Figure 39).

11. PLASMA LINES

11.1. Introduction

When $\alpha \to 0$ the only contribution of density fluctuations among the electrons to the scattering that results from electron-electron interactions is a weak component due to a plasma resonance. This component appears as two lines displaced from the radar frequency by an amount f_r , which is close to the plasma frequency f_p . In the absence of a magnetic field f_r is given by

$$f_r = \pm f_p (1 + \alpha^2)^{1/2} \qquad (35)$$

where $\alpha = 2\pi D_e/\lambda_p$.

At night the amount of power associated with each line is of the order of α^2 times that in the ionic component, and presently is detectable only by the radar at Arecibo. During the daytime the lines are enhanced by the presence of fast photoelectrons (Perkins and Salpeter, 1965), and by studying the echo intensity it is possible to detect the lines over a range of values of f_r that depends upon the radar wavelength. By locating the altitude at which a particular line is detected the plasma frequency vs height can be determined (and hence N_e). This is illustrated in Figure 40.

Since the intensity of the line depends upon the properties of the velocity distribution of the electrons by studying this it is possible to learn something about the photoelectron energy distribution. A detailed review has recently been presented by Cicerone (1974) and here we only outline the approach.

The plasma line echoes are caused by scattering from weakly damped longitudinal electrostatic plasma oscillations with frequency f_r , wavelength λ_p , and phase velocity v_{ph} $(= f_r \lambda_p)$. Photo-

electrons which overtake the waves can transfer energy to them and it is this process that gives rise to the enhancement during the daytime. The required energy of the electrons is

$$E_{ph} = \frac{1}{2} m_e (v_{ph})^2 = \frac{1}{2} m_e (f_r \lambda_p)^2 \qquad (36)$$

and hence for a given radar is a function only of the electron density prevailing at the height under study.

Electrons that are overtaken by the waves will remove energy (Landau damping), and thus at each height the wave intensity will depend upon the ratio of the number of electrons with energy slightly greater than E_{ph} to the number with energy slightly less, i.e. on the slope of the velocity distribution function of the photoelectrons $F_p(v)$ in the vicinity of v_{ph}. The radar results may be used to determine the ratio R by which the plasma line echo intensity has been enhanced by this process, where (Yngvesson and Perkins, 1968)

$$R = \frac{F_m (v_{ph}) + \chi + F_p (v_{ph})}{F_m(v_{ph}) + \chi - kT_e \, dF_p (v_{ph})/dE_{ph}} . \qquad (37)$$

In this equation $F_m (v_{ph})$ describes the effects of plasma wave-thermal electron interaction, and in the case of the ionosphere must include the effect of gyrorotation which allows relatively slow thermal electrons to damp and excite plasma waves. Depending somewhat on the direction of the radar beam with respect to the magnetic field this process places a lower limit on the frequency f_r at which the enhancement may be

seen, which is of the order of $f_r = 1/\lambda_p$ when λ_p is expressed in meters. The term χ in (37) describes electron-ion collisional excitation and damping of the waves and serves to place an upper limit on the frequency range of the enhancement of the order of $f_r = 3/\lambda_p$ MHz (Yngvesson and Perkins, 1968).

Figure 41 shows the range of plasma frequencies over which the plasma line can be expected to be enhanced for wavelengths of 70 cm, 23 cm, and 200 cm and for directions along ($\phi = 90^o$), 40^o ($\phi = 50^o$) and at 80^o ($\phi = 10^o$) to the field direction $\vec{B}$. In these plots the lowest frequency at which the enhancement occurs is set by the rule of thermal electrons dominating the energy distribution and the high frequency limit is imposed by electron-ion collisional damping.

Figure 42 shows measurements of the plasma line intensity kT_p for various plasma frequencies in the region above h_{max} F2. From these measurements it is possible to deduce the derivative of the one-dimensional velocity distribution at many heights. If it is then assumed that, at these altitudes all the photoelectrons are escaping, and hence the velocity distribution is height independent, it is possible to combine all the results to determine what the distribution is for the photoelectrons. Figure 43 provides an example of the particle and energy fluxes computed in this manner. (In Figure 39 the energy distribution function for the photoelectrons is shown as a box F(E) connected to the plasma line observations.

An alternate approach employed by Cicerone and Bowhill (1971) is to model the photoelectron production and transport processes and adjust the results to reproduce the observed values of R. The results appear to be reasonably consistent with direct measurements of photoelectron fluxes using satellites (Cicerone,

1974). Other uses of plasma line measurements have been in the study of the transport of photoelectrons from the magnetically conjugate point (Evans and Gastman, 1970; Carlson, 1972).

REFERENCES

Alcayde, D., P. Bauer, C. Jaeck and J.L. Falin, J. Geophys. Res. 76, 7814, 1971

Bowles, K.L., Phys. Res. Lett. 1, 451, 1958

Bowles, K.L., J. Res. NBS 65D, 1, 1961

Buneman, O., J. Geophys. Res. 67, 2050, 1962.

Carlson, H.C., Annls. Gèophys. 28, 179, 1972

Cicerone, R.J., Revs. Geophys. Space Res. 12, 1974

Cicerone, R.J. and Bowhill, S.A., Radio Sci. 6, 957, 1971

Dougherty, J.P. and Farley, D.T., Proc. R. Soc. A259, 79, 1960

Dougherty, J.P. and Farley, D.T., J. Geophys. Res. 68, 5473, 1963

Evans, J.V., Proc. IEEE, 57, 496, 1969

Evans, J.V., W.L. Oliver and J.E. Salah, J. Atmos. Terr. Phys. 41, 259, 1979

Evans, J.V., J. Atmos. Terr. Phys. 34, 175, 1972

Evans, J.V. and Gastman, I.J., J. Geophys. Res. 75, 807, 1970

Evans, J.V., J. Atmos. Terr. Phys., 36, 2183, 1974

Evans, J.V., Revs. Geophys. Space Phys. 16, 195, 1978

Evans, J.V., Proc. IEEE 63, 1636, 1974

Evans, J.V., Planet. Space Sci. 13, 1031, 1965

Evans, J.V. and J.M. Holt, Lincoln Lab. Tech Rep. 522, Lexington, Mass., USA, 1976

Evans, J.V. and G.P. Martas, J. Atmos. Terr. Phys. 30, 563, 1968

Fabry, C., C.r. Acad. Sci., Paris 187, 777, 1928

Farley, D.T., J. Atmos. Terr. Phys. 32, 693, 1970

Fejer, J.A., Can. J. Phys. 38, 1114, 1960

Gordon, W.E., Proc. IRE 46, 1824, 1958

Hagfors, T., J. Geophys. Res. 66, 1699, 1961

Hagen, J.B. and Hsu, P.Y.S., J. Geophys. Res. 79, 4269, 1974

Harper, J. Geophys. Res. 82, 3233, 1977

Hedin, A.E. and D. Alcayde, J. Geophys. Res. 79, 1579, 1974

Hedin, A.E. et al., J. Geophys. Res. 75, 4825, 1970

Moorcroft, D.R., J. Geophys. Res. 68, 4870, 1963

Moorcroft, D.R., J. Geophys. Res. 69, 995, 1964

Perkins, F.W. and Salpeter, E.E., Phys. Rev. 139A, 59, 1965

Rosenbluth, M.N. and N. Rostoker, Phys. Fluids 5 , 776, 1962

Salpeter, E.E., Phys. Rev. 120, 1528, 1960a

Salpeter, E.E., J. Geophys. Res. 65, 1851, 1960b

Vasseur, G., J. Atmos. Terr. Phys. 31, 397, 1969a

Vasseur, G., Annls. Géophys. 25, 517, 1969b

Waldteufel, P., J. Geophys. Res. 76, 6995, 1971

Wand, R.H. and F.W. Perkins, J. Geophys. Res. 73, 6370, 1968

Yngvesson, K.O. and Perkins, F.W., J. Geophys. Res. 73, 97, 1968

FIGURE CAPTIONS

Figure 1 — Diagram showing the direction of incident and reflected waves and the components of the plasma drift that can be observed for a bistatic radar system. In the direction OP the important spatial scale for density fluctuations is λ_p .

Figure 2 — Sketch of the frequency power spectrum of incoherent scatter signals for the case $\alpha \to 0$ and $T_e = T_i$. The radar frequency is f .

Figure 3 — Spectra (one side only) of the reflected power for the case $\alpha \to 0$ and $T_e/T_i \geq 1.0$ (cf. Figure 2).

Figure 4 — Spectra (one side only) of the reflected power for the case $\alpha \to 0$ and $T_e/T_i = 1.0, 2.0, 3.0$, for three ions plotted on a normalized frequency scale (after Moorcroft, 1964).

Figure 5 — The spectra of Figure 4 are here plotted on an absolute frequency scale to illustrate the increase in width that accompanies the reduction in ion mass (after Moorcroft, 1964).

Figure 6 — The variation of the observed electron cross section σ_e as a function of T_e/T_i for the case $\alpha \to 0$ at $T_e/T_i \to 0$ (after Moorcroft, 1963). The dashed curve shows the variation predicted by Eq. (11) given by Buneman (1962).

Figure 7 — Effect of increasing the Debye length D_e on the ion component of the spectrum for the case $T_e = T_i$ (after Rosenbluth and Rostoker, 1962).

Figure 8 — A-scope display showing incoherent scatter returns from the ionosphere (between 200 and 500 km) and receiver noise.

Figure 9 — Electron density profile obtained from measurements of echo power vs delay using 100 μsec pulses. In this case it has been assumed that σ = const.

Figure 10 — Plots of N_e , T_e , T_i obtained for Millstone Hill from measurements using pulses of 100, 500 and 1000 μsec.

Figure 11 — Contour diagrams showing the variation as functions of height and time the electron density, electron and ion temperature obtained from plots such as Fig. 10.
a) $\text{Log}_{10} N_e$; b) T_e ; c) T_i

Figure 12 — Early efforts to account for the observed electron and ion temperatures (points) observed at Millstone Hill by adjusting the total heat input Q and flux from the magnetosphere Q_M . N_e is the measured electron density profile (Evans and Mantas, 1968).

Figure 14 — Average daytime and nighttime values of the heat flux Q_M from the magnetosphere over Millstone in 1967.
a) Daytime; b) Nighttime

Figure 15 — Variation of average daytime magnetospheric heat flux for 6 summer and 6 winter months with year. Also shown is the average 10.7 cm radio flux from the sun.

Figure 16 Values of electron density, electron and ion temperture measured at Millstone Hill together with the variation of the neutral temperature T_n (Eq. 23) deduced from these measurements. The parameters for the solution are given in the right-hand panel.

Figure 17 Variation of exospheric temperature deduced from the incoherent scatter technique for different times of year.

Figure 18 Atomic oxygen density at 400 km as a function of local time for 8 Oct 1969 over St. Santin de Maurs (45^{o} N) based on incoherent scatter and satellite measurements (after Hedin and Alcayde, 1974).

Figure 19 Effect of ion neutral collisions on the spectrum shape for the case $T_e = T_i$. Here ψ_i is a measure of the ratio of the scale λ_p explored by the radar to the mean-free path of the ions (Dougherty and Farley, 1963).

Figure 20 Estimates of N_2 concentration at 100 km obtained (via Eq. 25) from estimates of ν_{in} in France. The variation with local time is due to diurnal and semi-diurnal tides (Waldteufel, 1971).

Figure 21 Estimates of N_2 concentration (cf. Fig. 20) vs time of year obtained from observations at St. Santin de Maurs (Waldteufel, 1971).

Figure 22 Variation of spectrum shape for a mixture of O^+ and He^+ (N_2) for $T_e/T_i = 1.5$ (after Moorcroft, 1964).

Figure 23 Variation of spectrum shape for mixtures of O^+ , He^+ and H^+ for $T_e/T_i = 2.0$ (after Moorcroft, 1964).

Figure 24 Composition results obtained over Arecibo at night when it can be assumed $T_e = T_i$ (Hagen and Hsu, 1974).

Figure 25 Measurements of electron density, H^+ concentration, T_e , and T_i at night over Millstone in winter when the proton flux is downwards.

Figure 26 Theoretical curves for the H^+ concentration for various values of the proton flux. In this plot the critical escape flux that can be supported by vertical diffusion is 1.35×10^8 ions/cm^2/sec.

Figure 27 The transition between O^+ and molecular ions (NO^+ and O_2^+) according to various rocket measurements.

Figure 28 Illustrating how the composition variation in the F1 region can be obtained if a variation is assumed for the ion temperature such as the Bates formula (Eq. 23).

Figure 29 Variation of the six parameters T_∞ , T_0 , s , $N(O)_{400}$, z_{50} and τ_{50} obtained on one day from a simultaneous solution for all the spectra over the height interval $120 \leq h \leq 500$ km obtained at St. Santin by Oliver (see Evans et al., 1969).

Figure 30 Effect of a drift of the ions on the spectra of the signals.

Figure 31 Horizontal neutral winds observed in the E region over Millstone Hill on several days in 1976 (Wand, R.H., unpublished).

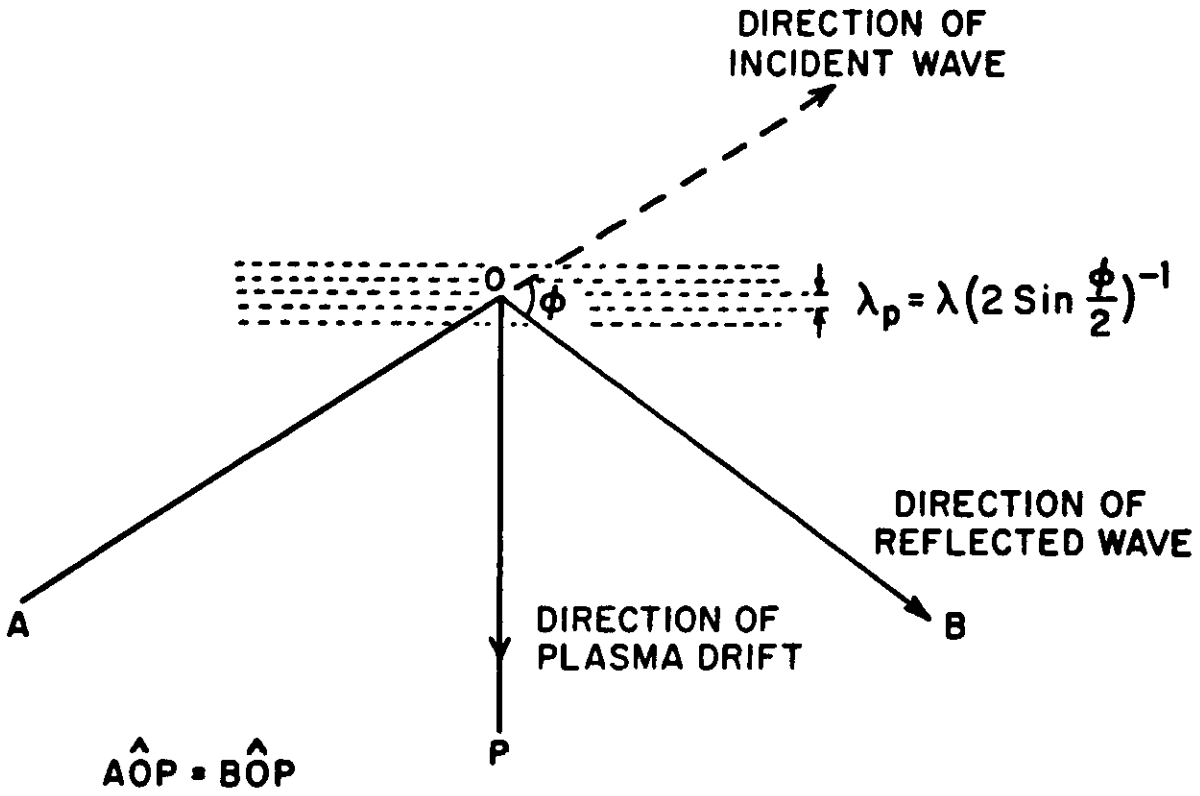

Fig. 1

$T_e = T_i$

$\Delta f_i = \frac{2\bar{v}_i}{\lambda}$

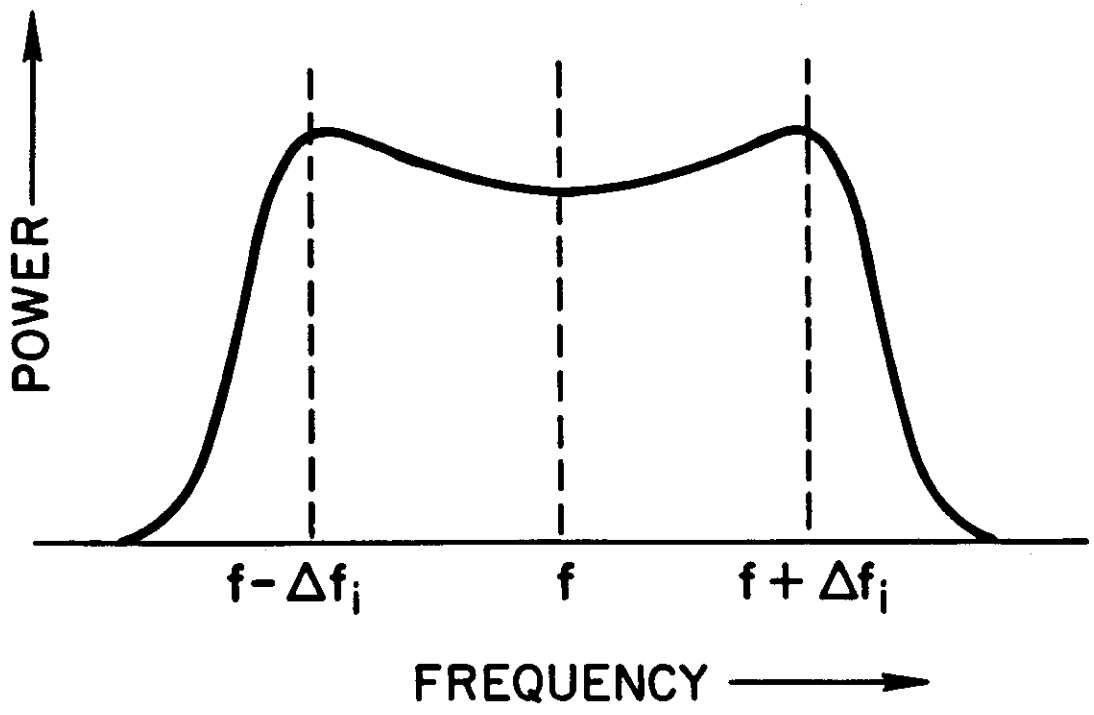

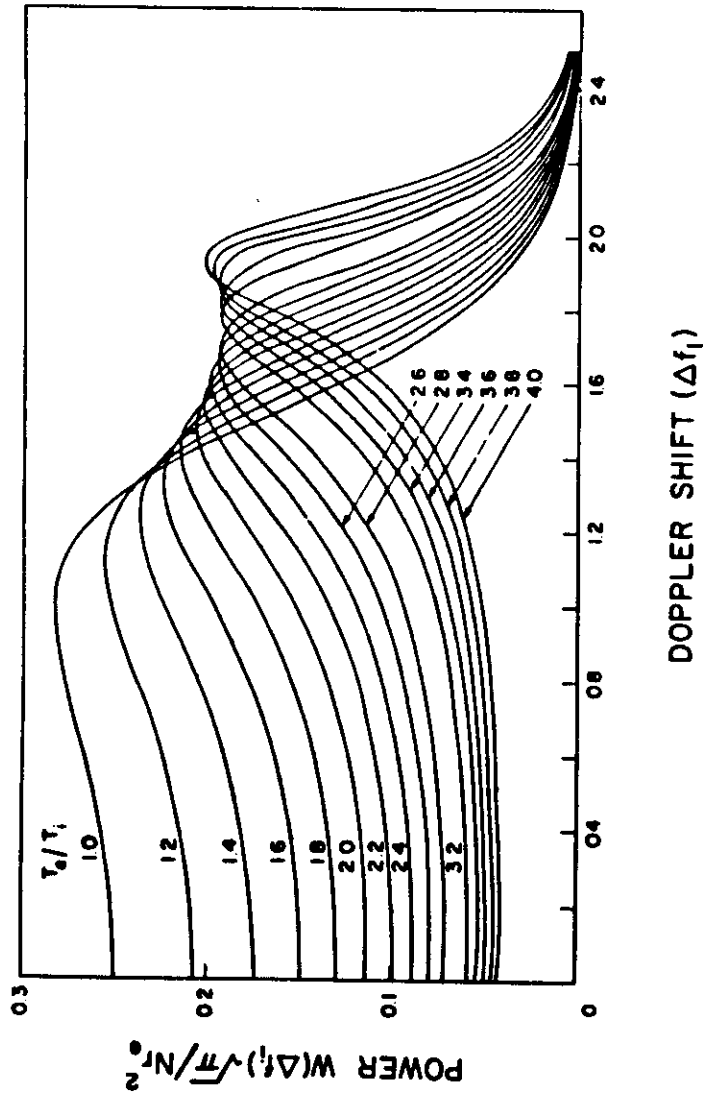
POWER W(Δf_i)√π/Nr_e²
0.3
0.2
0.1
0
DOPPLER SHIFT (Δf_i)
0.4
0.8
1.2
1.6
2.0
2.4
T_e/T_i
1.0
1.2
1.4
1.6
1.8
2.0
2.2
2.4
3.2
2.6
2.8
3.4
3.6
3.8
4.0

Fig. 3

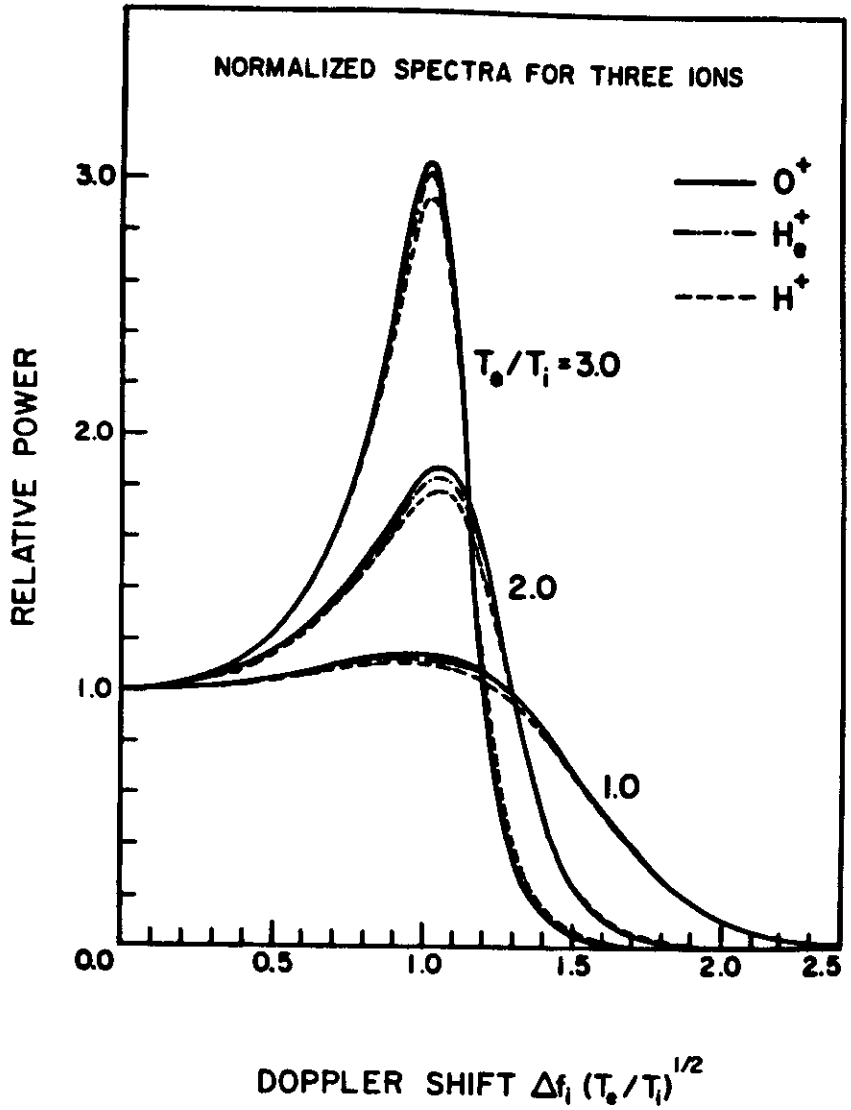
NORMALIZED SPECTRA FOR THREE IONS
O+
He+
H+
T_e/T_i = 3.0
2.0
1.0
RELATIVE POWER
3.0
2.0
1.0
0.0
0.5
1.0
1.5
2.0
2.5
DOPPLER SHIFT Δf_i (T_e/T_i)^1/2

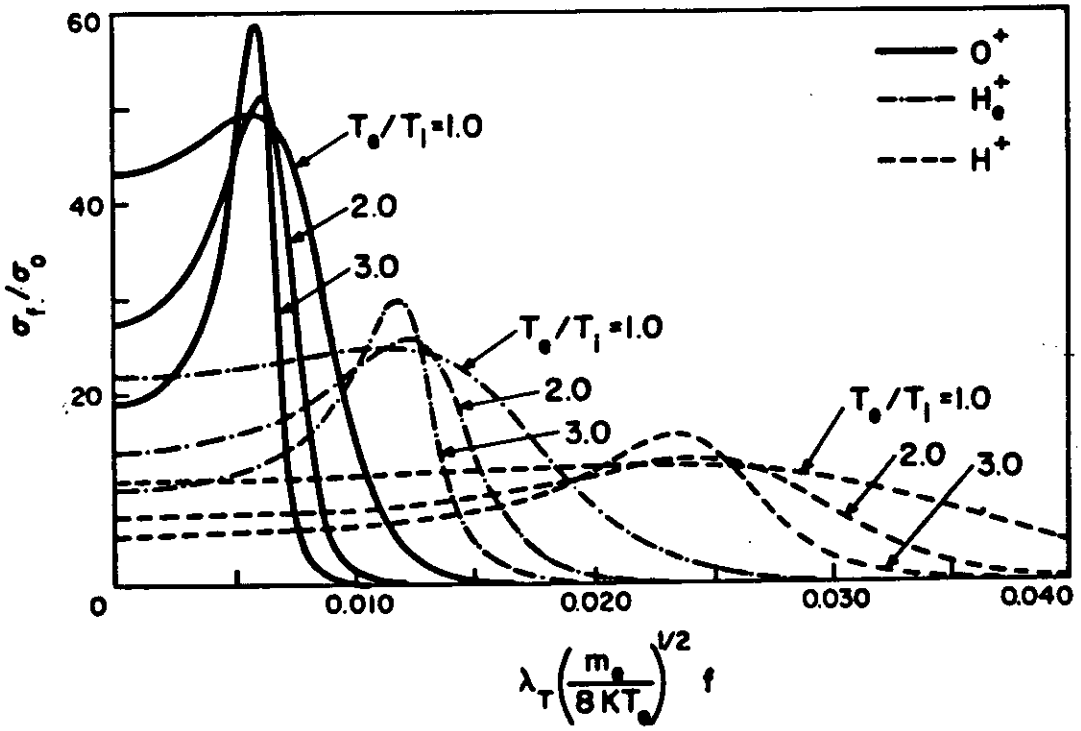
60
40
20
0
σ_i/σ_o
O^+
H_e^+
H^+
T_e/T_i=1.0
2.0
3.0
T_e/T_i=1.0
2.0
3.0
T_e/T_i=1.0
2.0
3.0
0.010
0.020
0.030
0.040
$\lambda_T\left(\frac{m_e}{8KT_e}\right)^{1/2} f$

Fig. 5

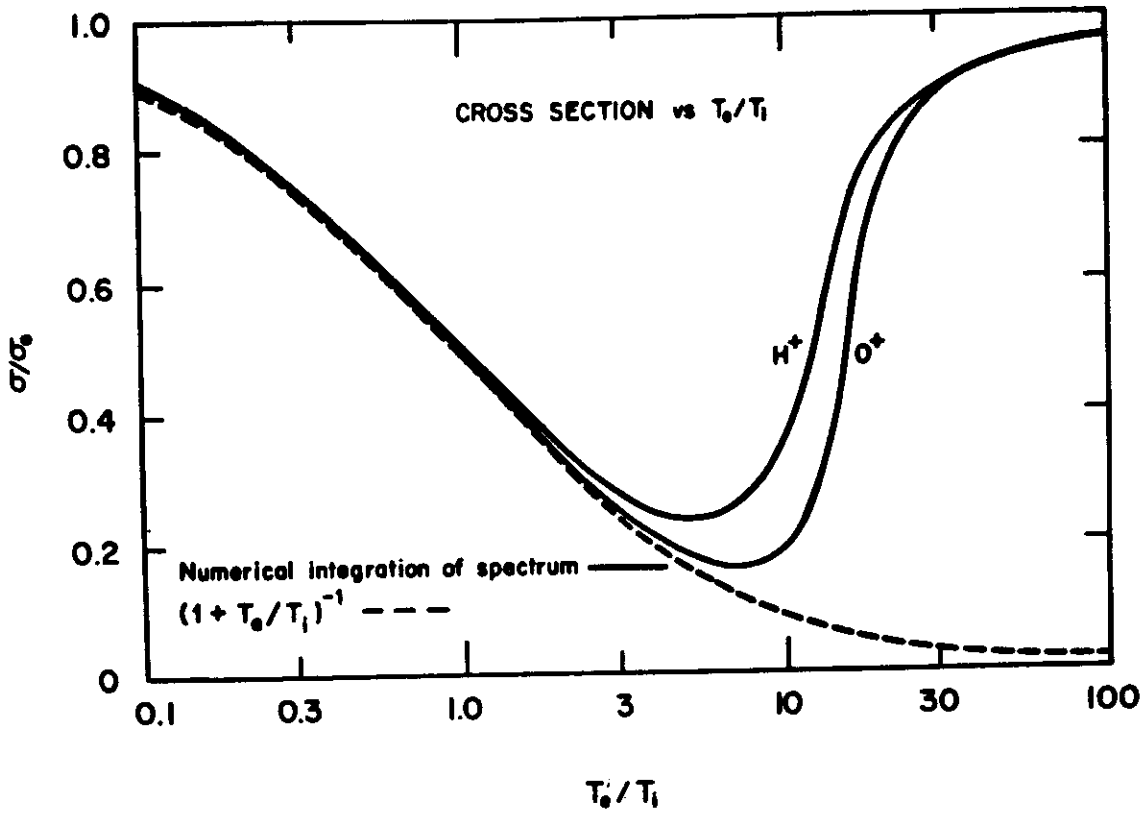
1.0
0.8
0.6
0.4
0.2
0
σ/σ_e
CROSS SECTION vs T_e/T_i
H^+
O^+
Numerical integration of spectrum
$(1+T_e/T_i)^{-1}$
0.1
0.3
1.0
3
10
30
100
T_e/T_i

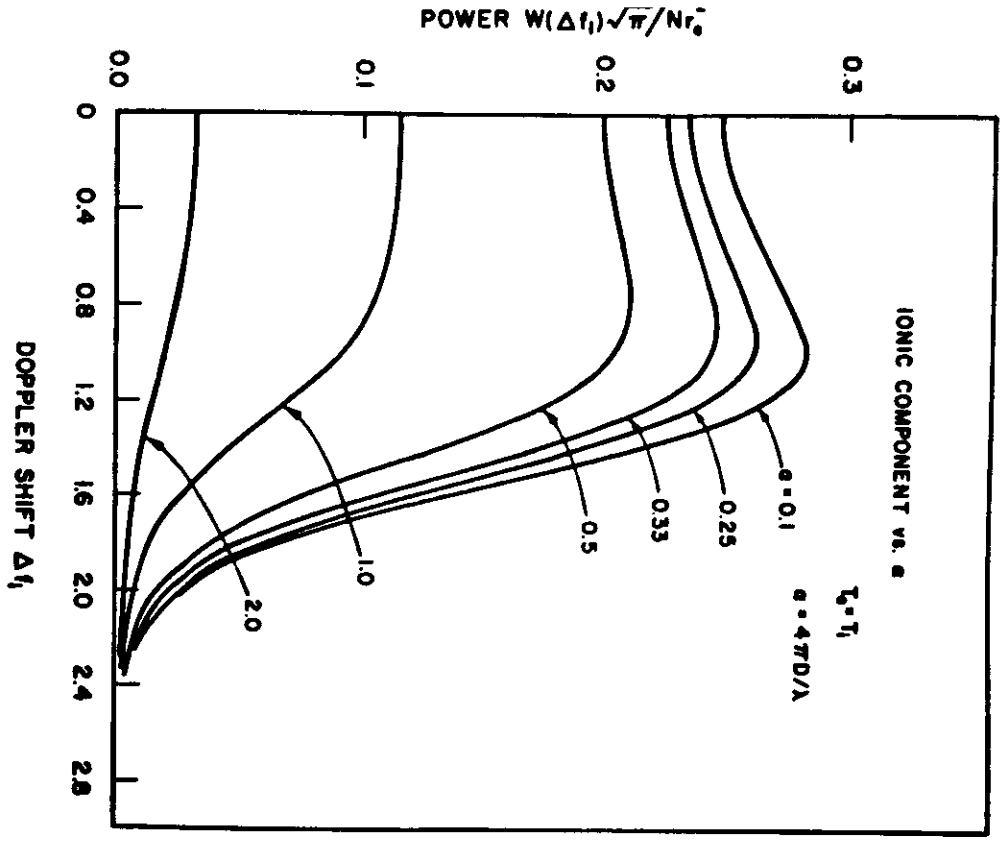

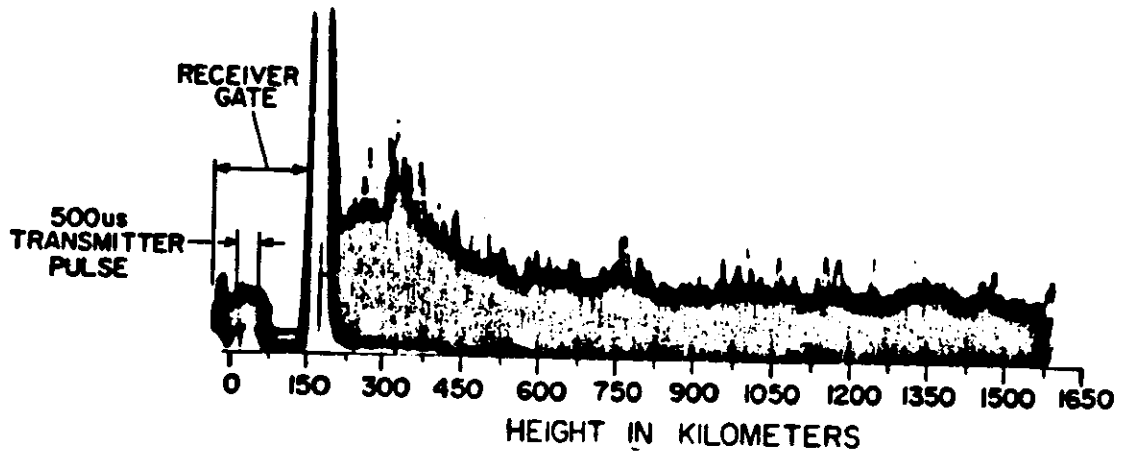

VERTICAL INCIDENCE BACKSCATTER AT 440mc/s
OBSERVED AT 1434 hrs E.S.T., FEB. 8, 1960.

Fig. 8

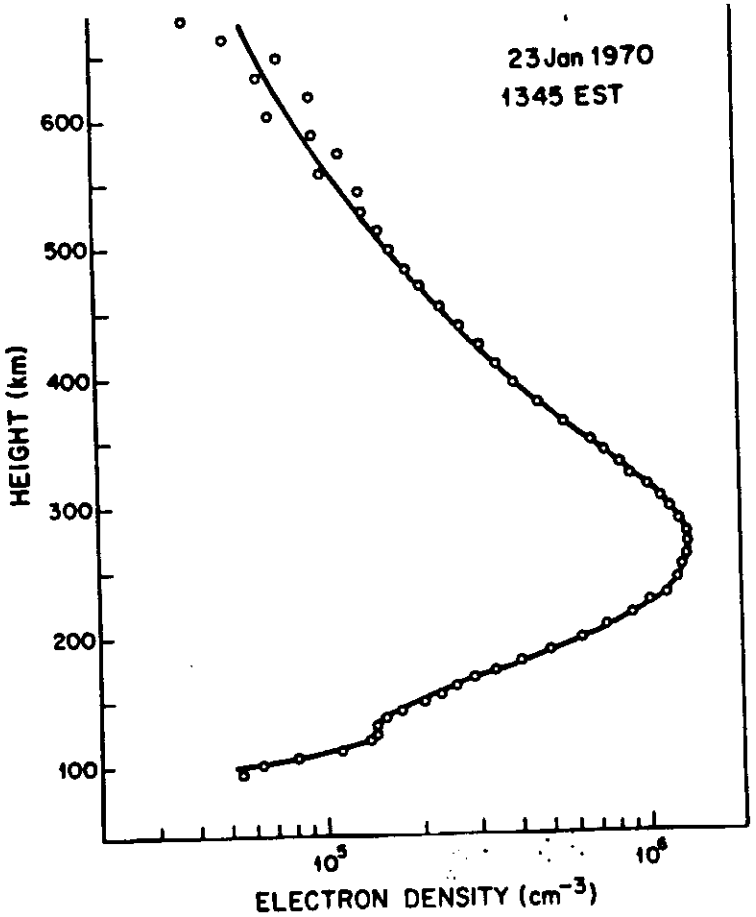
23 Jan 1970
1345 EST
HEIGHT (km)
600
500
400
300
200
100
10^5
10^6
ELECTRON DENSITY (cm^{-3})

Fig. 9

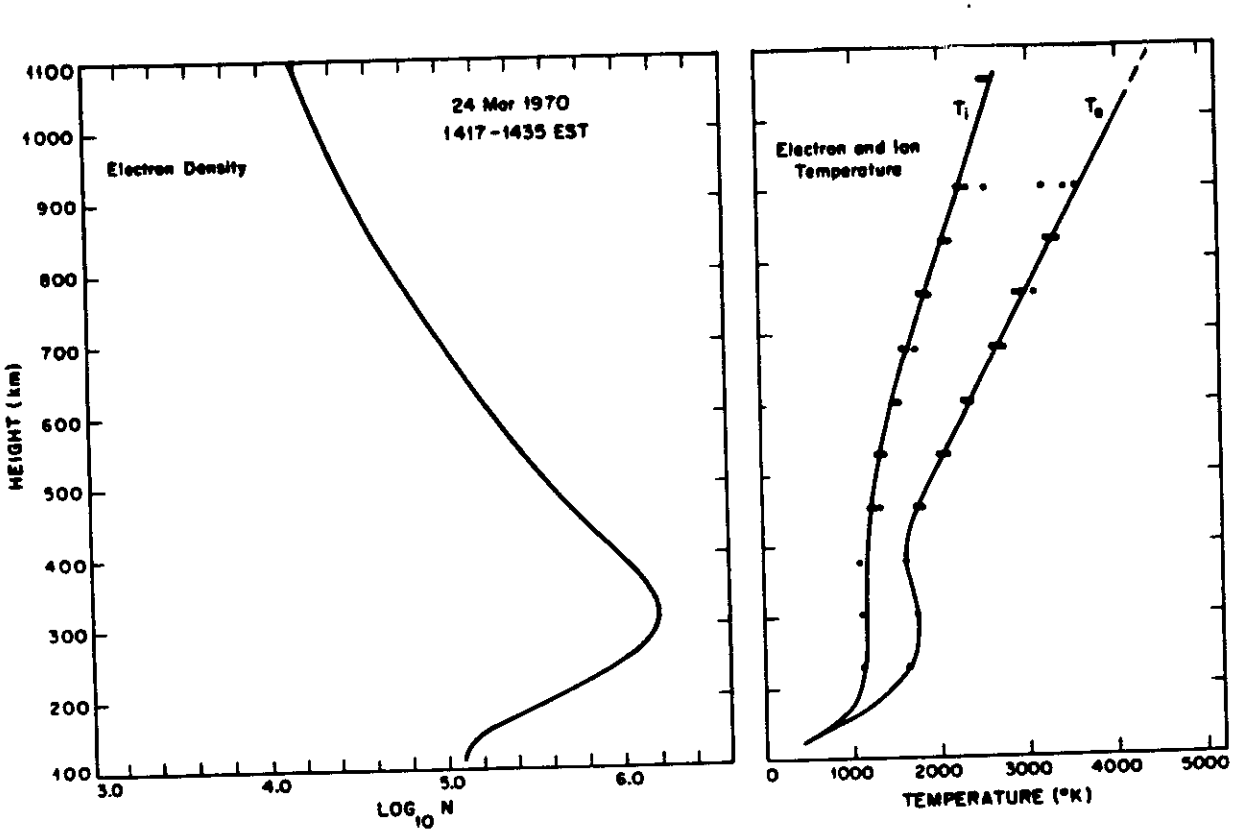
24 Mar 1970
1417-1435 EST
Electron Density
HEIGHT (km)
1100
1000
900
800
700
600
500
400
300
200
100
3.0
4.0
5.0
6.0
LOG_{10} N
Electron and Ion Temperature
T_i
T_e
0
1000
2000
3000
4000
5000
TEMPERATURE (°K)

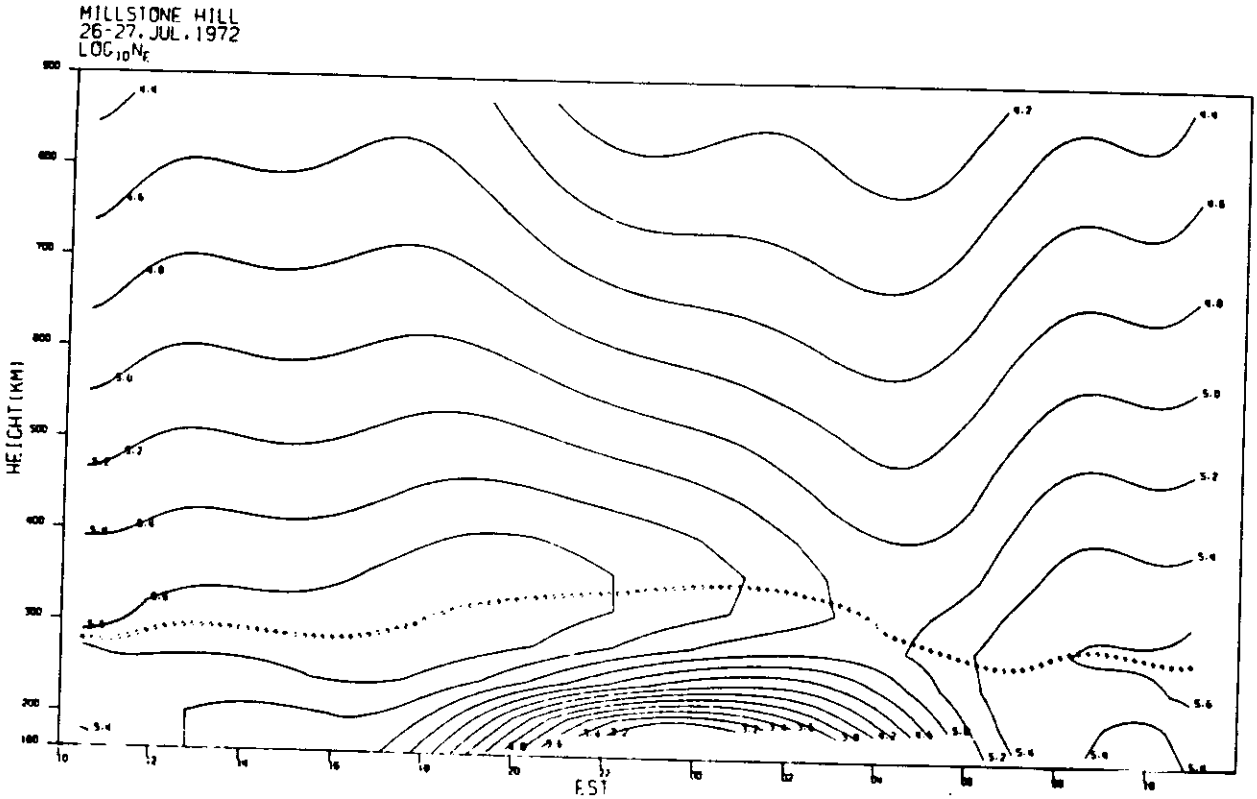
MILLSTONE HILL
26-27, JUL. 1972
$LOG_{10}N_E$
HEIGHT (KM)
EST

Fig. 11a

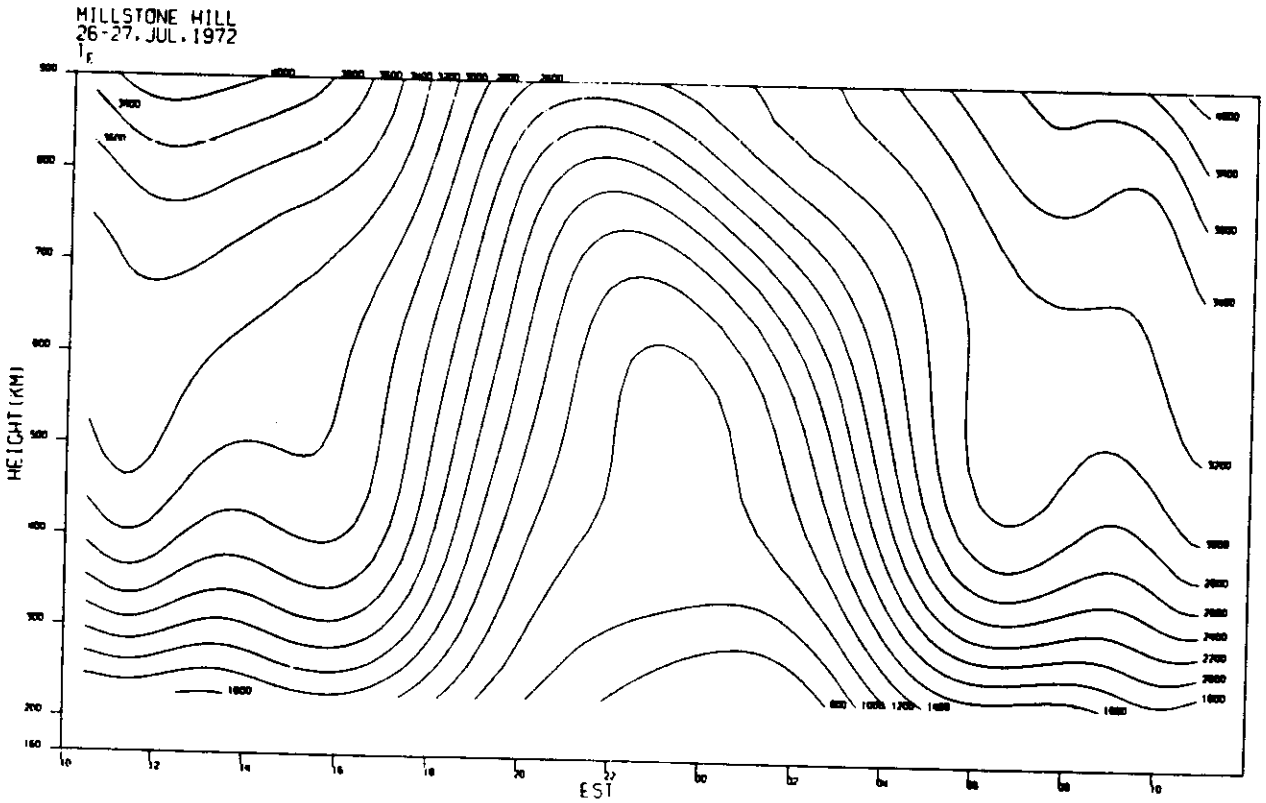
MILLSTONE HILL
26-27, JUL. 1972
T_E
HEIGHT (KM)
EST

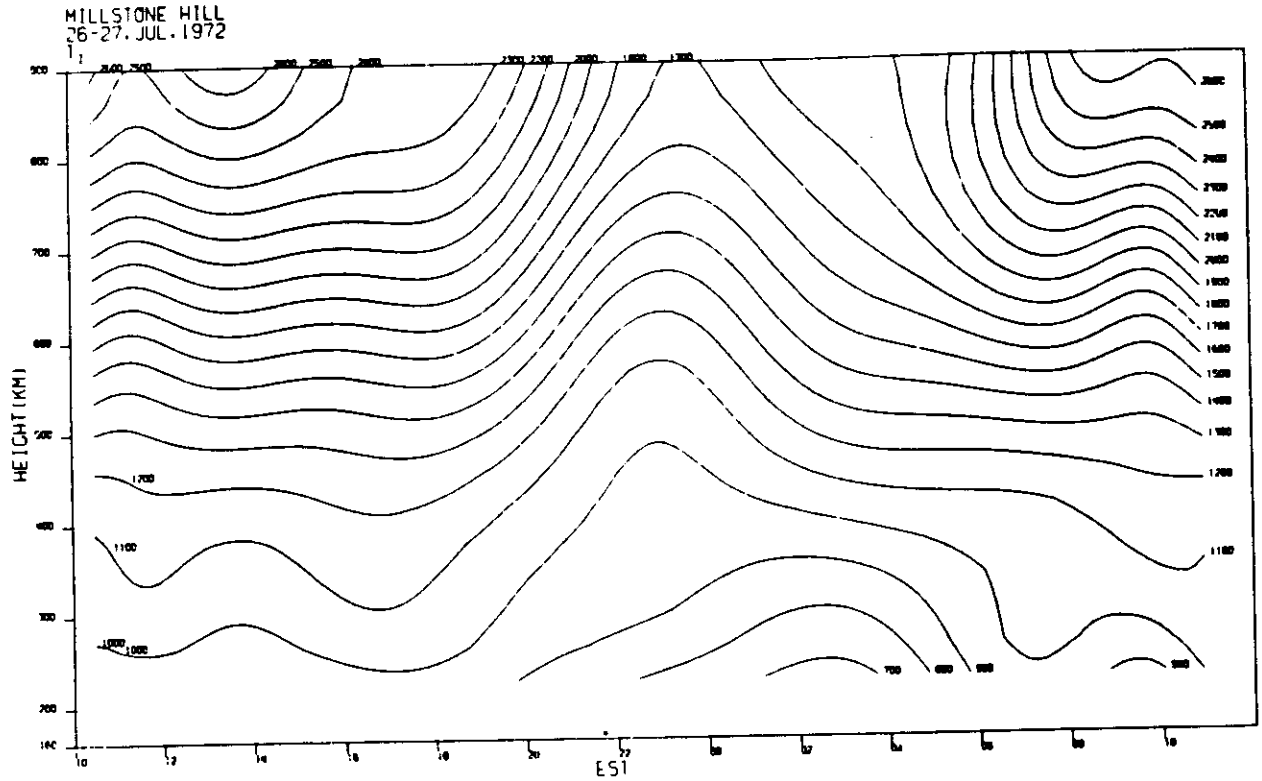
MILLSTONE HILL
26-27. JUL. 1972
HEIGHT (KM)
EST

Fig. 11c

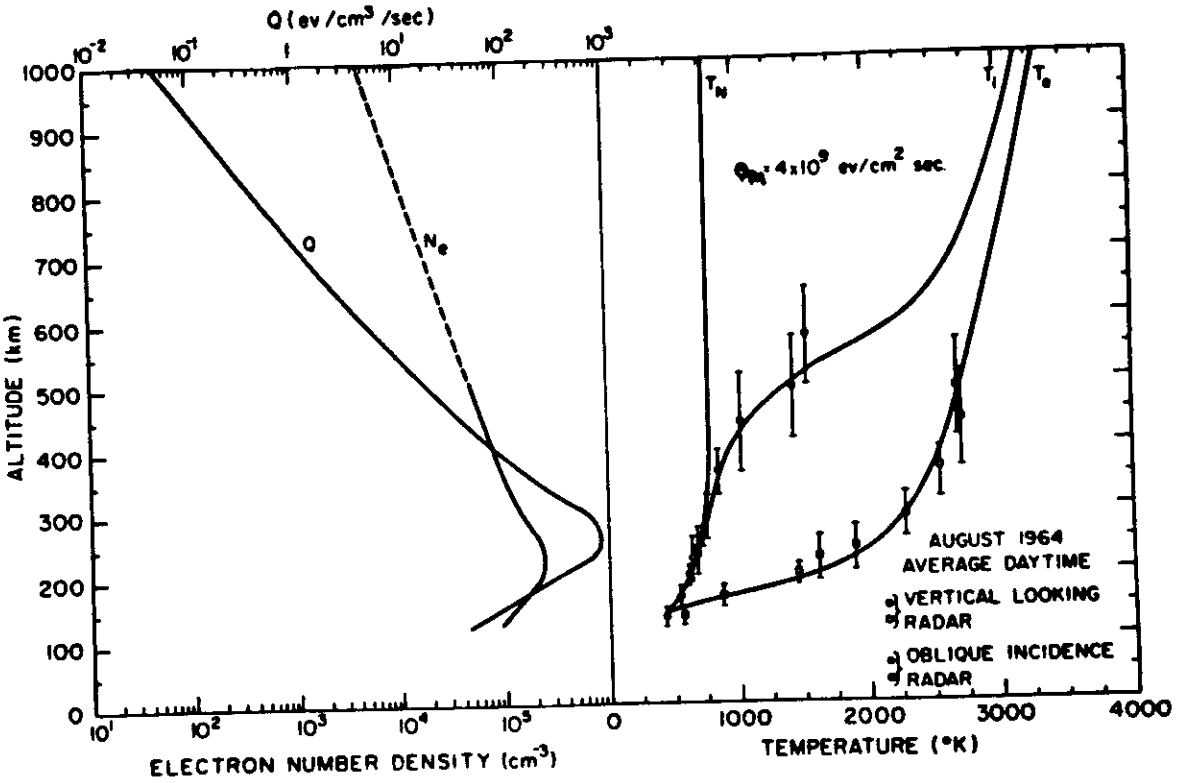
Q (ev/cm³/sec)
ALTITUDE (km)
ELECTRON NUMBER DENSITY (cm⁻³)
TEMPERATURE (°K)
Q
Ne
Tn
Ti
Te
Qpk = 4x10⁹ ev/cm² sec.
AUGUST 1964
AVERAGE DAYTIME
VERTICAL LOOKING RADAR
OBLIQUE INCIDENCE RADAR

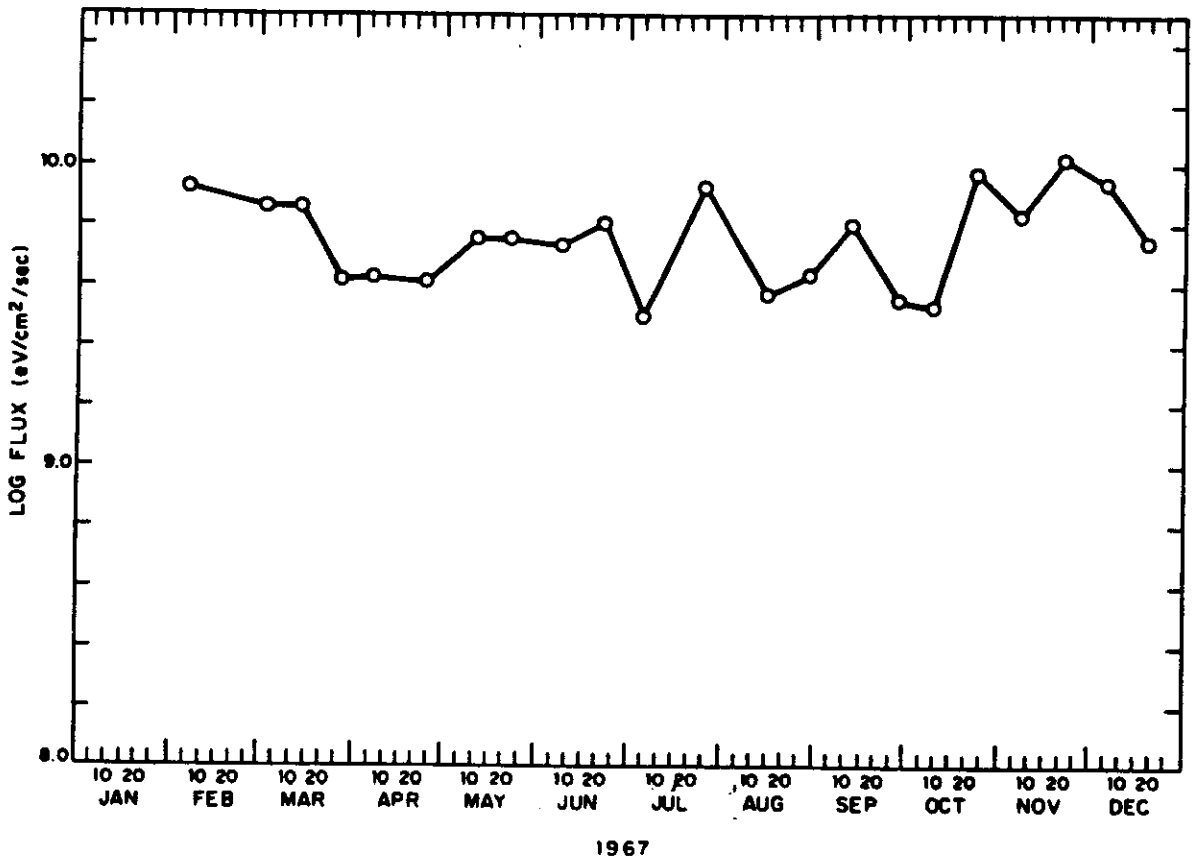
LOG FLUX (eV/cm²/sec)
10.0
9.0
8.0
10 20 JAN
10 20 FEB
10 20 MAR
10 20 APR
10 20 MAY
10 20 JUN
10 20 JUL
10 20 AUG
10 20 SEP
10 20 OCT
10 20 NOV
10 20 DEC
1967

Fig. 14a

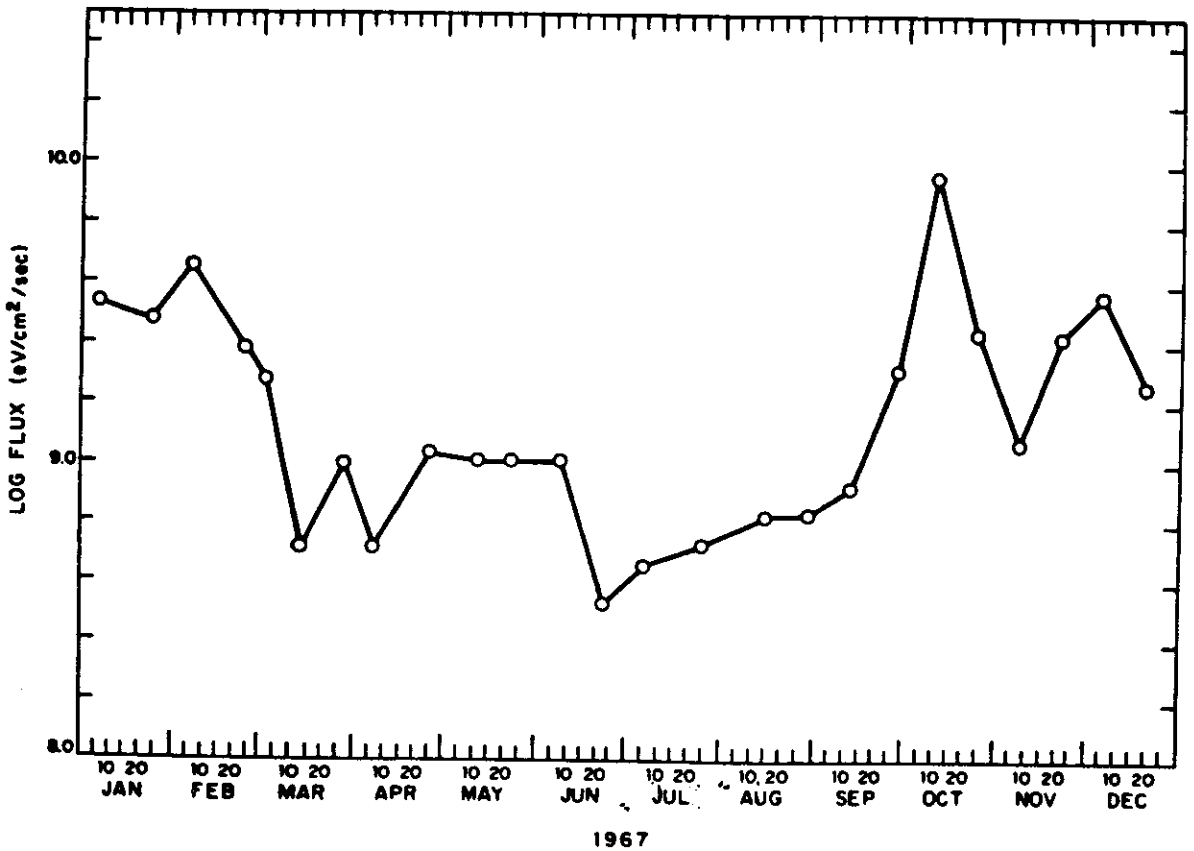
LOG FLUX (eV/cm²/sec)
10.0
9.0
8.0
10 20 JAN
10 20 FEB
10 20 MAR
10 20 APR
10 20 MAY
10 20 JUN
10 20 JUL
10 20 AUG
10 20 SEP
10 20 OCT
10 20 NOV
10 20 DEC
1967

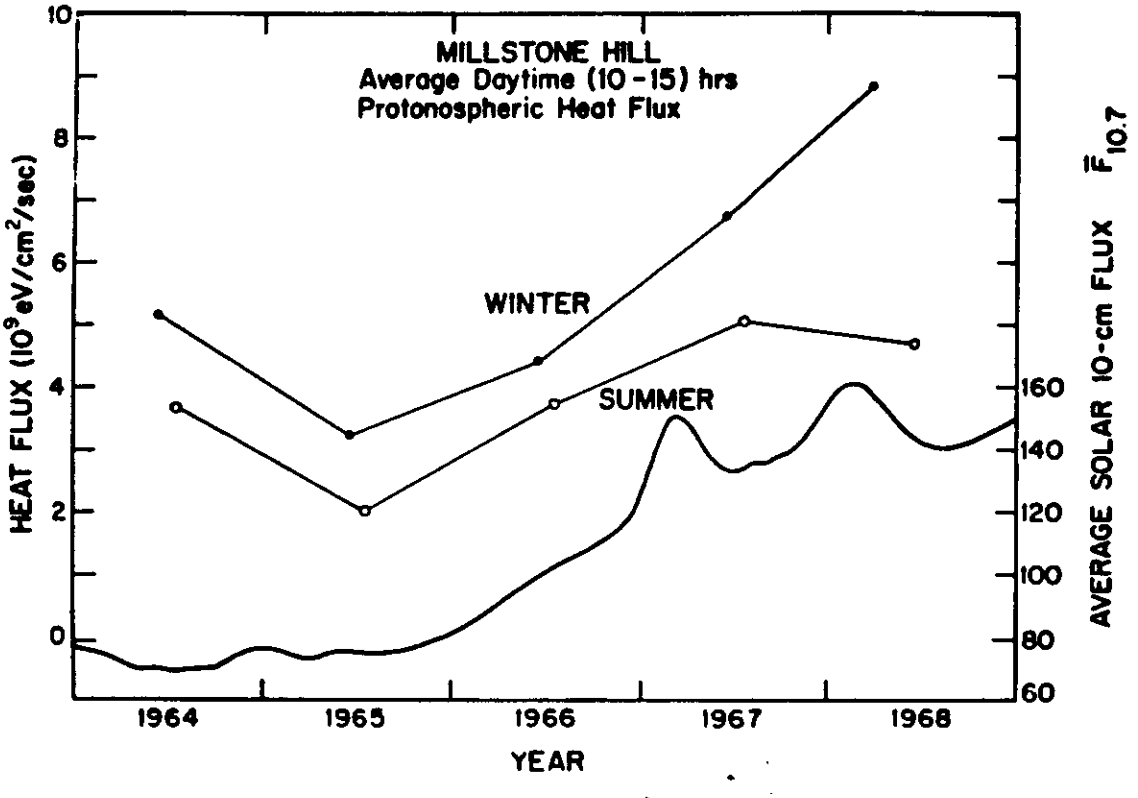
MILLSTONE HILL
Average Daytime (10-15) hrs
Protonospheric Heat Flux
WINTER
SUMMER
HEAT FLUX (10^9 eV/cm^2/sec)
AVERAGE SOLAR 10-cm FLUX $\bar{F}_{10.7}$
YEAR
1964
1965
1966
1967
1968

Fig. 15

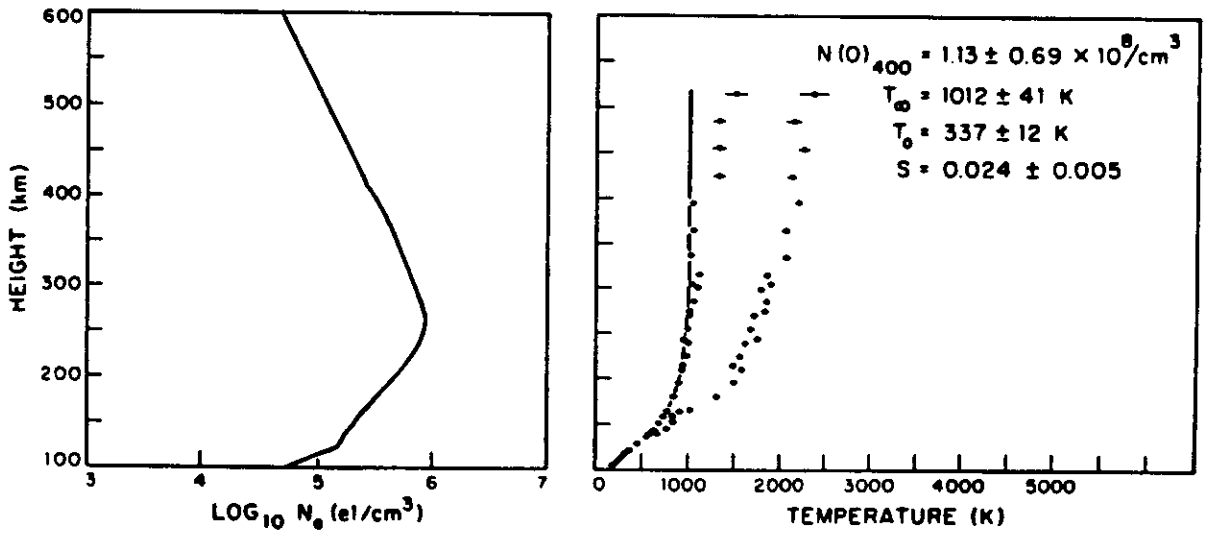
HEIGHT (km)
LOG_{10} N_e (el/cm^3)
$N(O)_{400}$ = 1.13 ± 0.69 × 10^8/cm^3
T_∞ = 1012 ± 41 K
T_0 = 337 ± 12 K
S = 0.024 ± 0.005
TEMPERATURE (K)

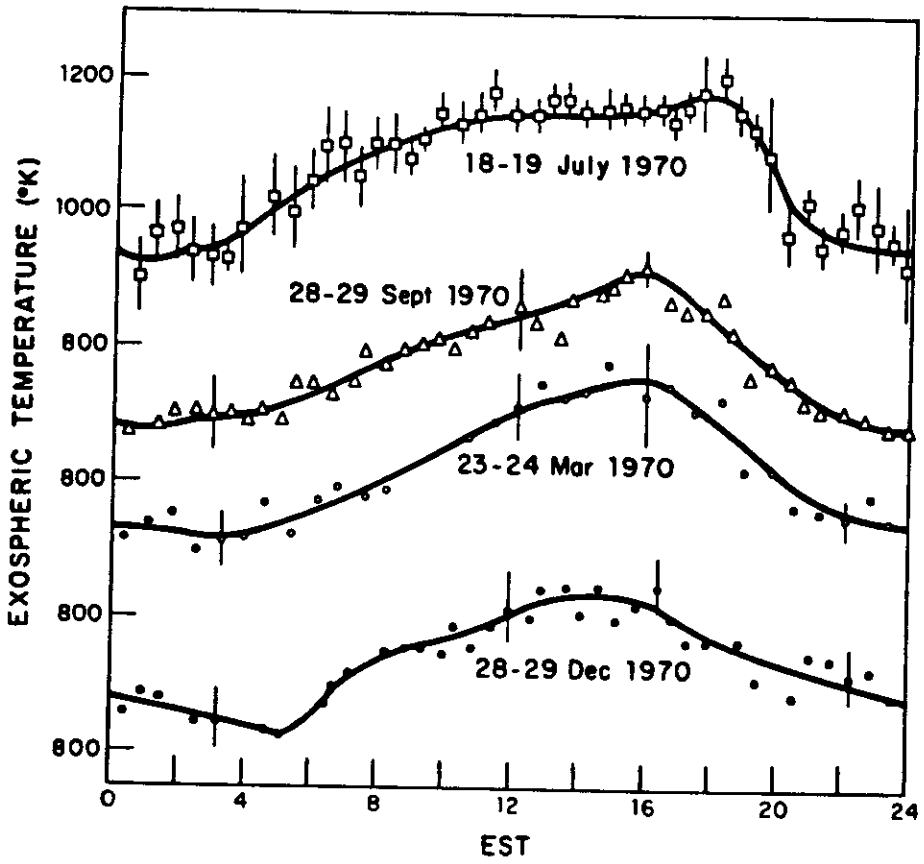
EXOSPHERIC TEMPERATURE (°K)
1200
1000
800
800
800
800
18-19 July 1970
28-29 Sept 1970
23-24 Mar 1970
28-29 Dec 1970
0
4
8
12
16
20
24
EST

Fig. 17

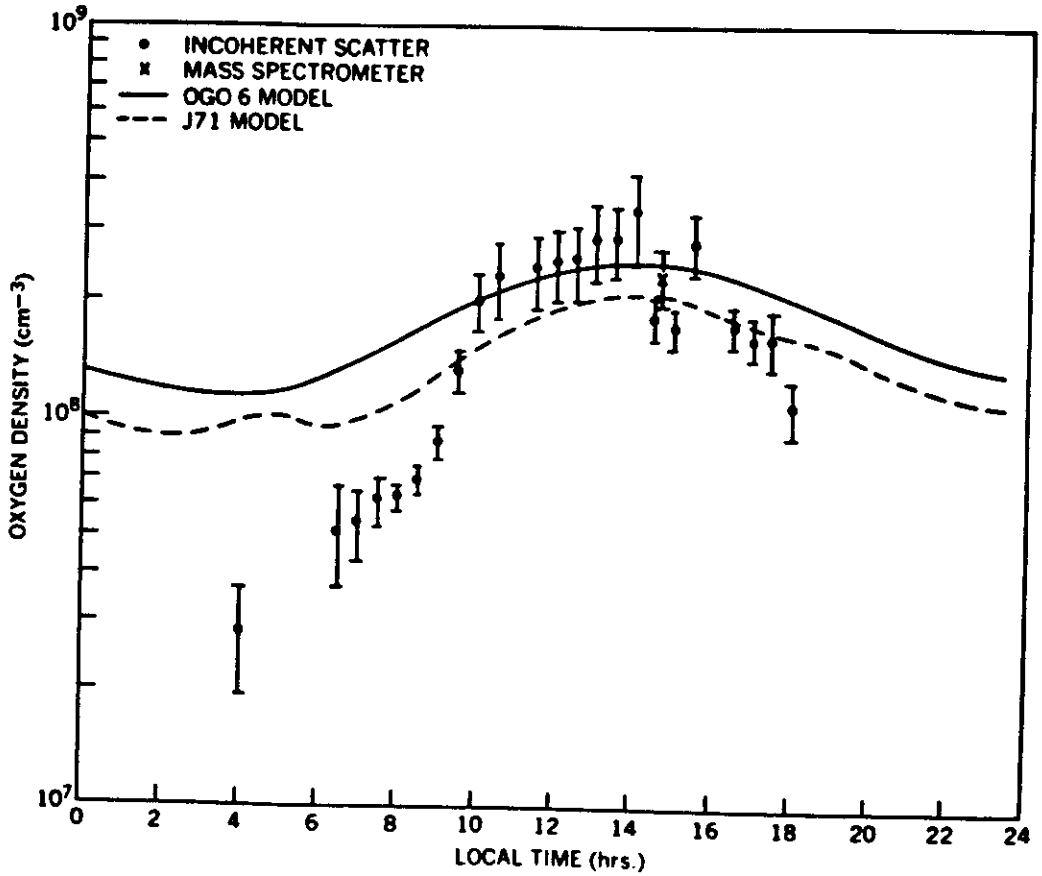
INCOHERENT SCATTER
MASS SPECTROMETER
OGO 6 MODEL
J71 MODEL
OXYGEN DENSITY (cm⁻³)
10⁹
10⁸
10⁷
0
2
4
6
8
10
12
14
16
18
20
22
24
LOCAL TIME (hrs.)

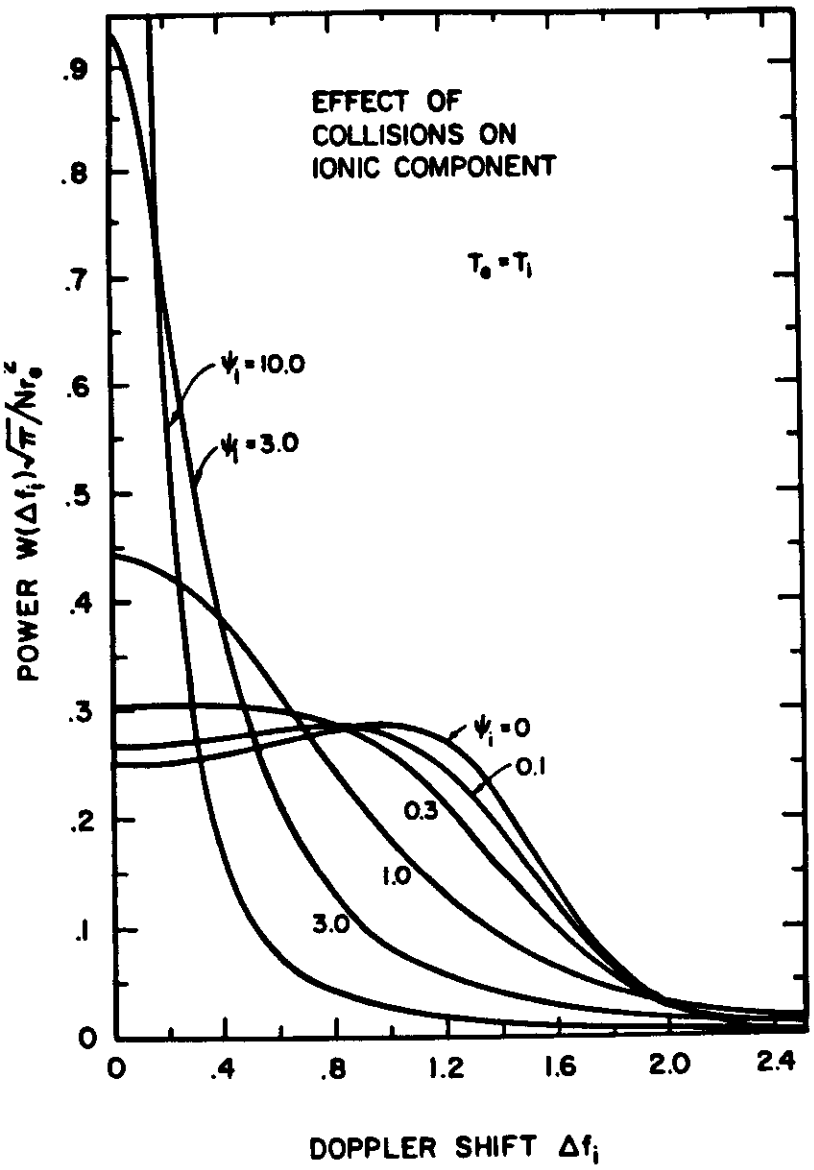

SAINT SANTIN - FEVRIER 1969

CONCENTRATION $[N_2]$ A 100 km

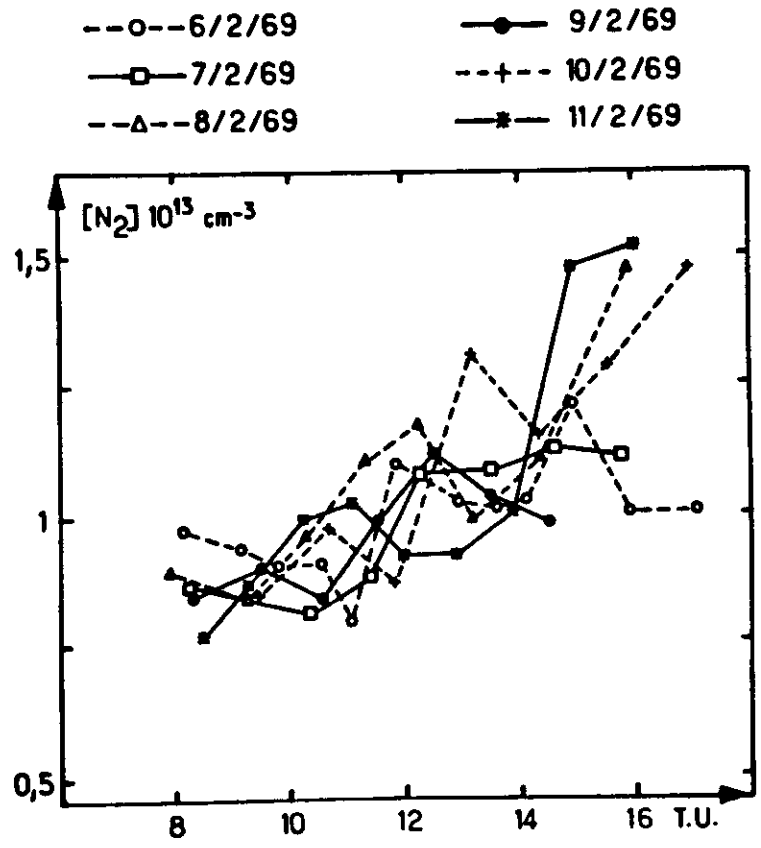

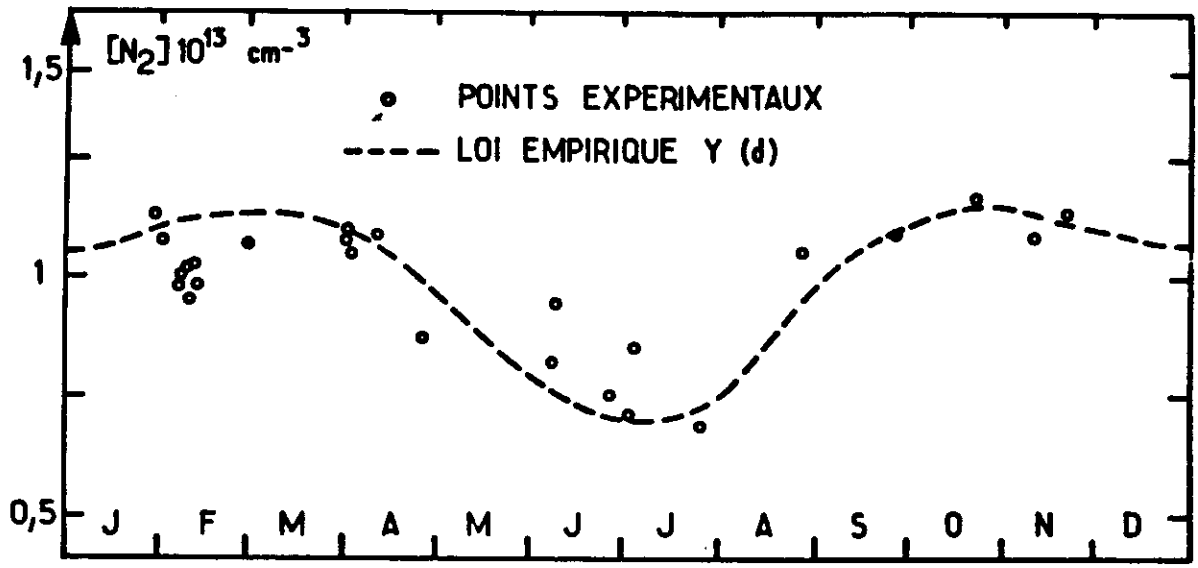
[N2] 10^13 cm^-3
POINTS EXPERIMENTAUX
LOI EMPIRIQUE Y (d)
1,5
1
0,5
J F M A M J J A S O N D

Fig. 21

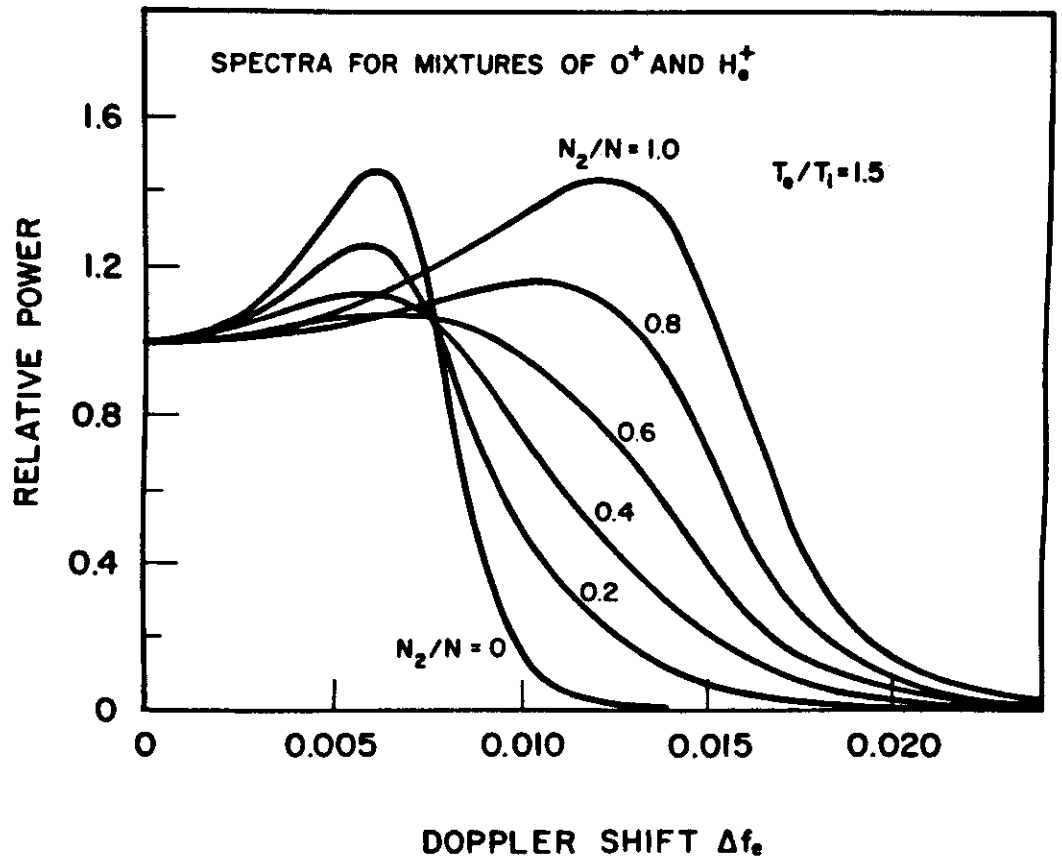
SPECTRA FOR MIXTURES OF O+ AND H+
N2/N = 1.0
Te/Ti = 1.5
0.8
0.6
0.4
0.2
N2/N = 0
RELATIVE POWER
1.6
1.2
0.8
0.4
0
0
0.005
0.010
0.015
0.020
DOPPLER SHIFT Δfe

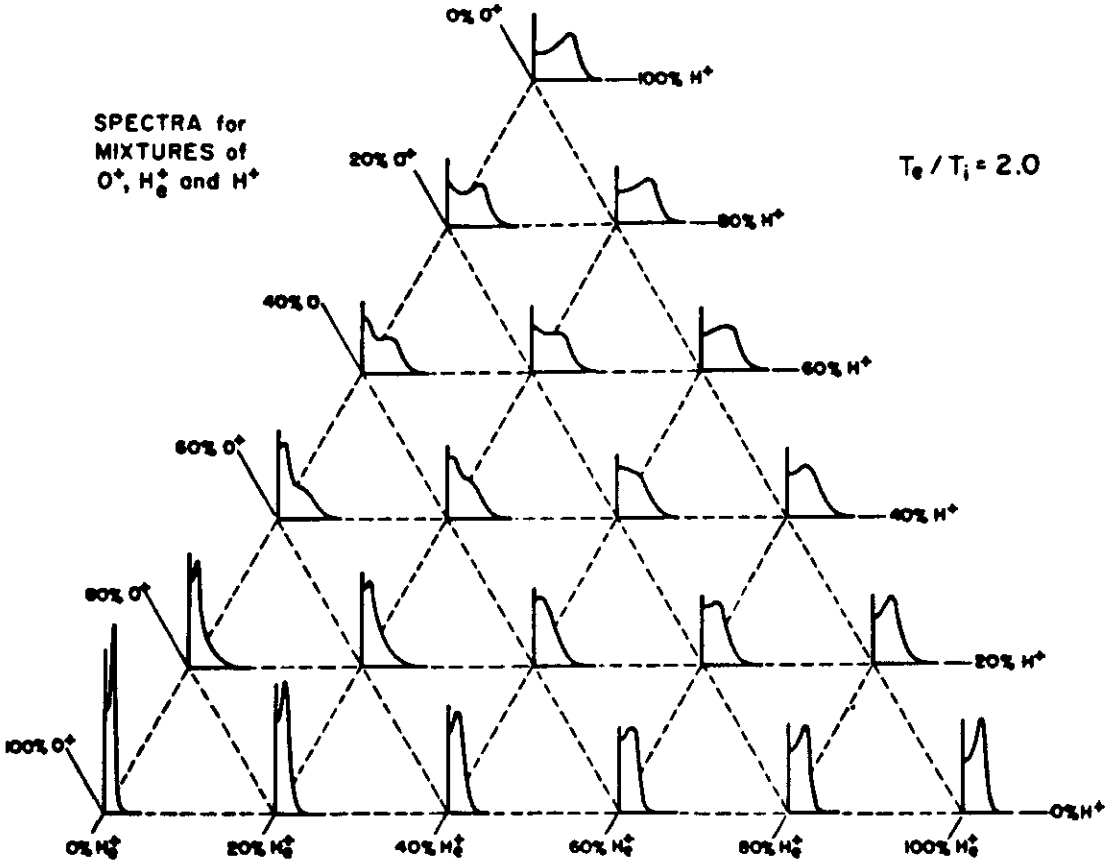
SPECTRA for
MIXTURES of
O^+, H_e^+ and H^+
$T_e / T_i = 2.0$
0% O^+
100% H^+
20% O^+
80% H^+
40% O^+
60% H^+
60% O^+
40% H^+
80% O^+
20% H^+
100% O^+
0% H^+
0% H_e^+
20% H_e^+
40% H_e^+
60% H_e^+
80% H_e^+
100% H_e^+

Fig. 23

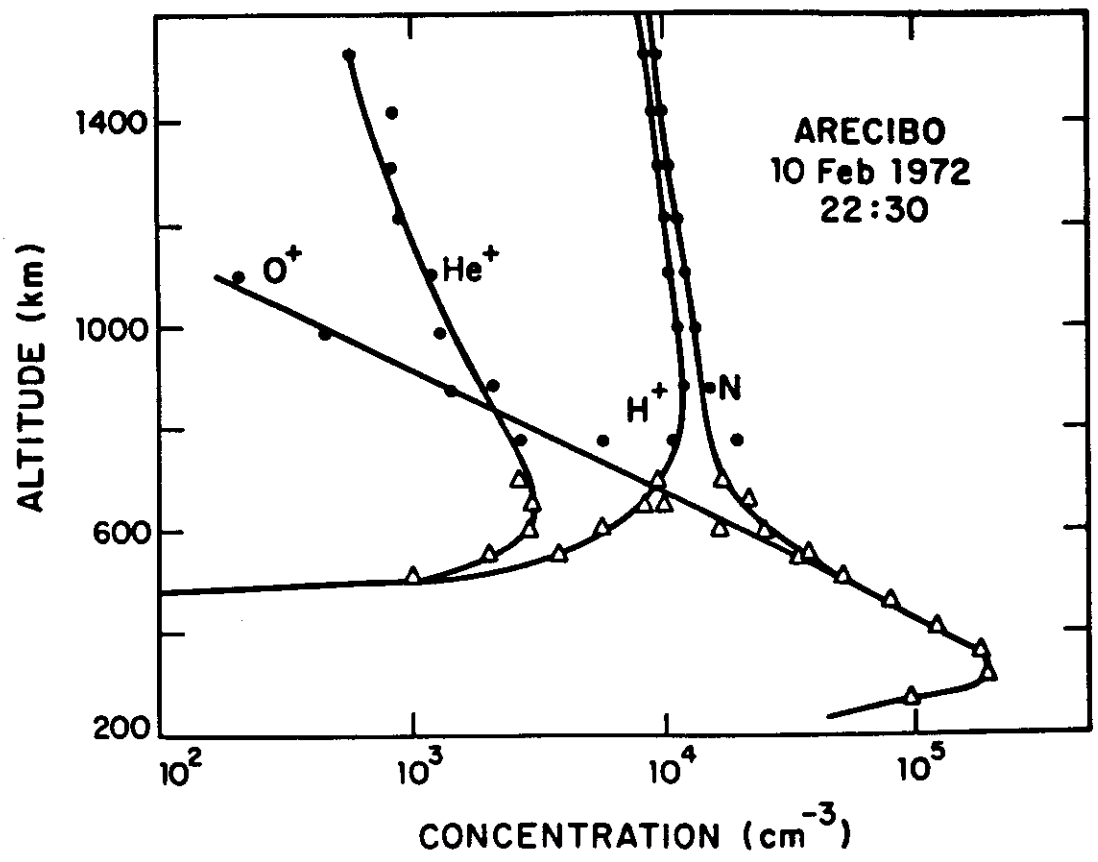
ARECIBO
10 Feb 1972
22:30
O^+
He^+
H^+
N
ALTITUDE (km)
1400
1000
600
200
10^2
10^3
10^4
10^5
CONCENTRATION (cm^{-3})

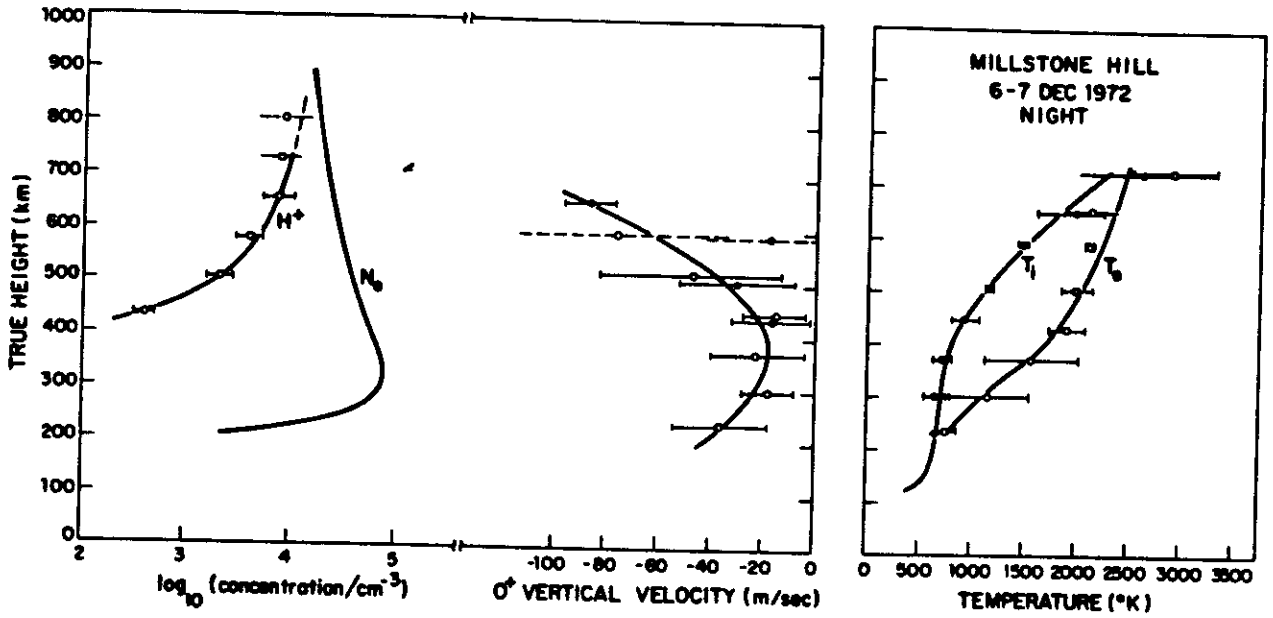
TRUE HEIGHT (km)
1000
900
800
700
600
500
400
300
200
100
0
H+
Ne
2
3
4
5
log10 (concentration/cm-3)
-100 -80 -60 -40 -20 0
O+ VERTICAL VELOCITY (m/sec)
MILLSTONE HILL
6-7 DEC 1972
NIGHT
Ti
Te
0 500 1000 1500 2000 2500 3000 3500
TEMPERATURE (°K)

Fig. 25

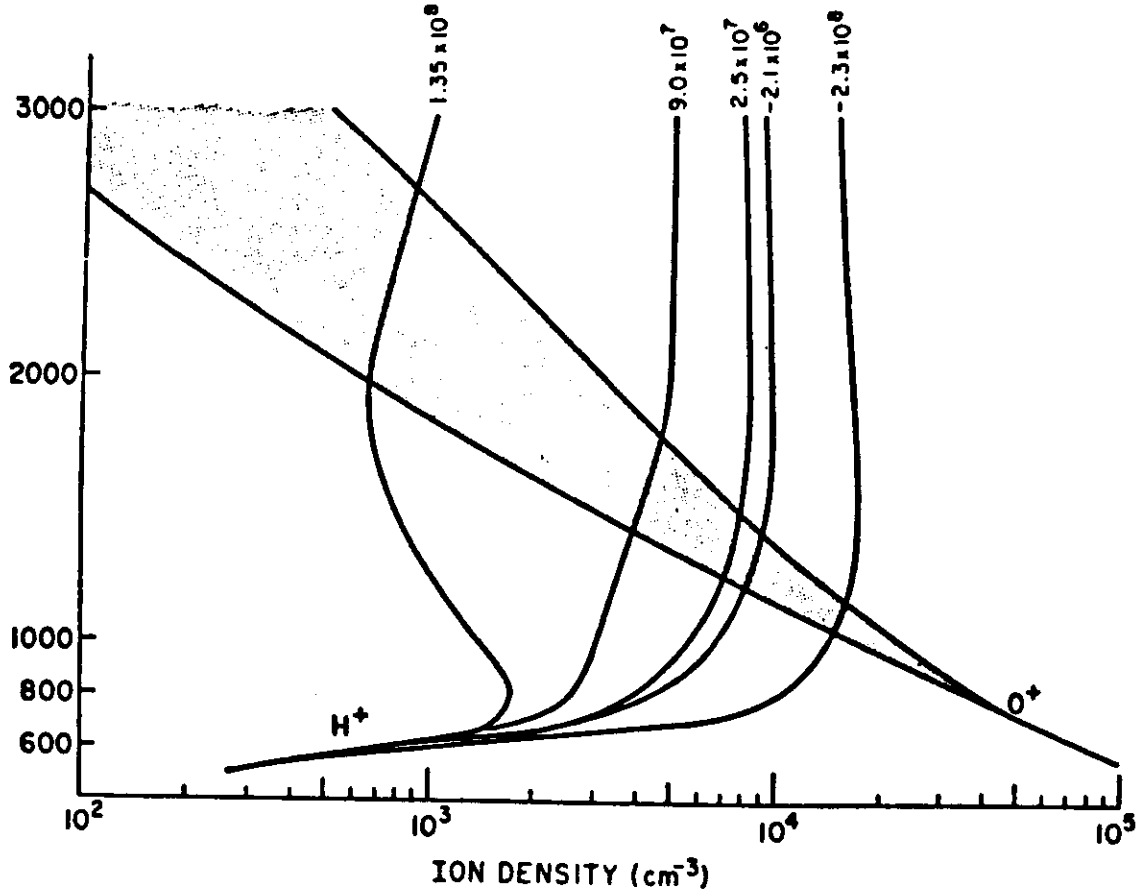
3000
2000
1000
800
600
1.35x10^8
9.0x10^7
2.5x10^7
-2.1x10^6
-2.3x10^8
H+
O+
10^2
10^3
10^4
10^5
ION DENSITY (cm-3)

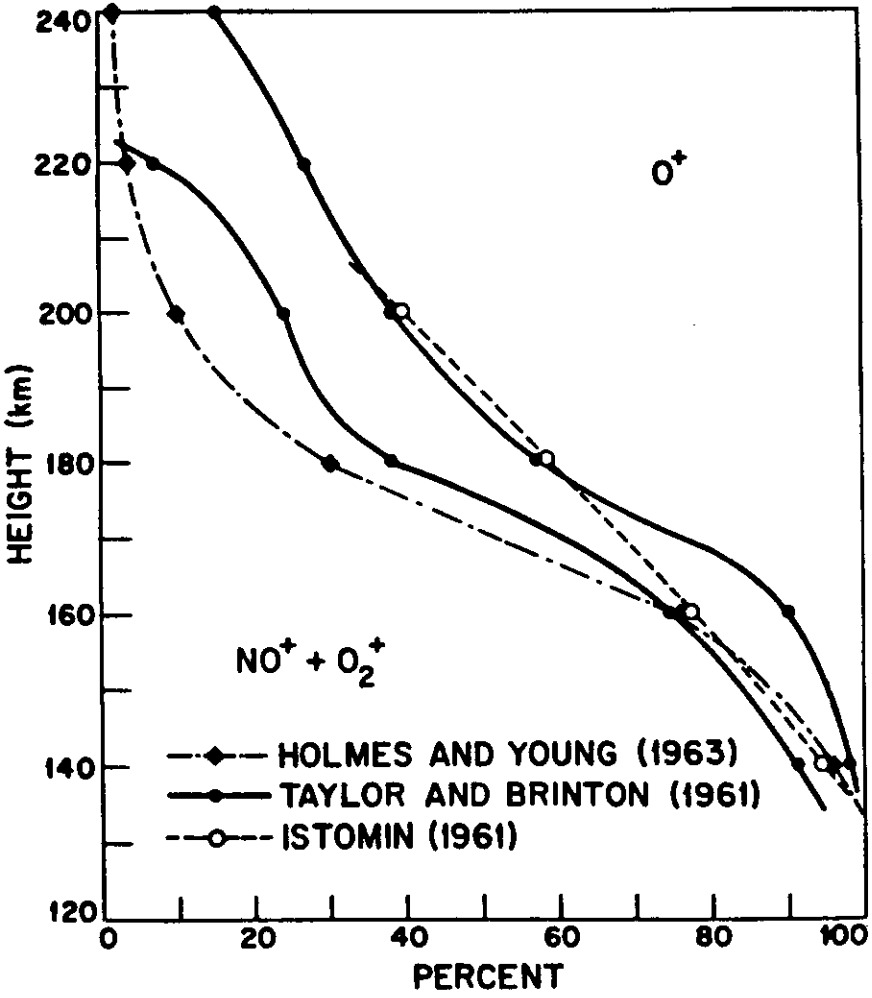
240
220
200
180
160
140
120
HEIGHT (km)
0
20
40
60
80
100
PERCENT
O+
NO+ + O2+
HOLMES AND YOUNG (1963)
TAYLOR AND BRINTON (1961)
ISTOMIN (1961)

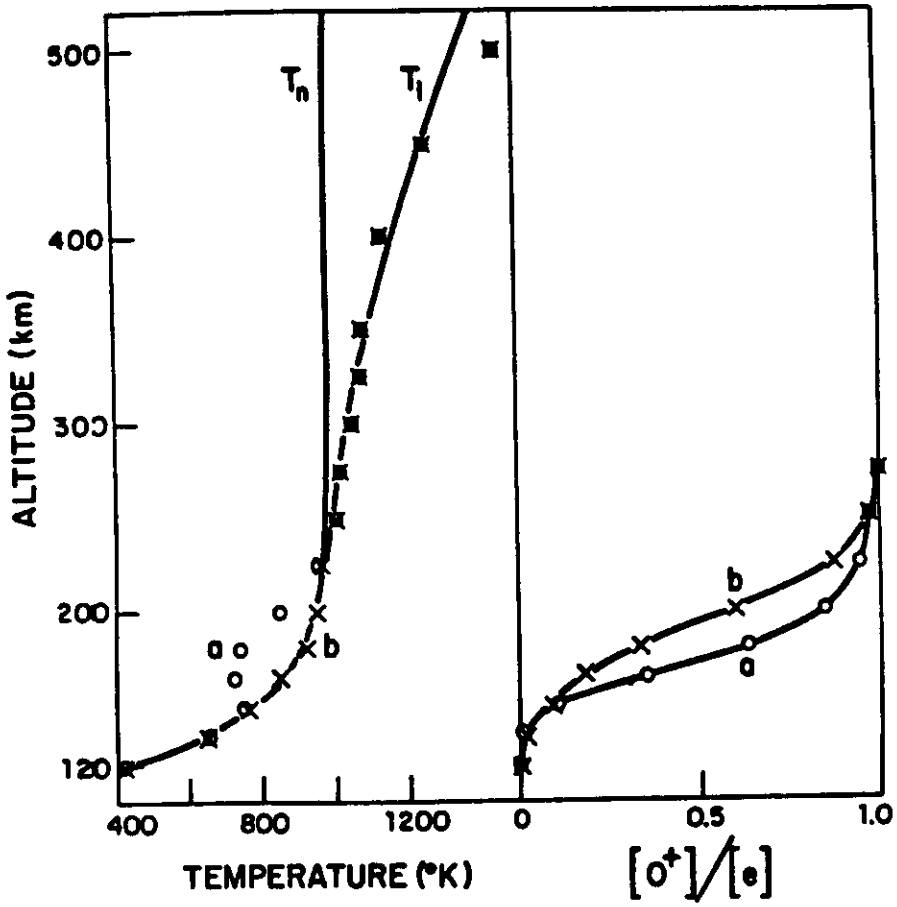
500
400
300
200
120
ALTITUDE (km)
Tn
Ti
a
b
400
800
1200
TEMPERATURE (°K)
0
0.5
1.0
[O+]/[e]

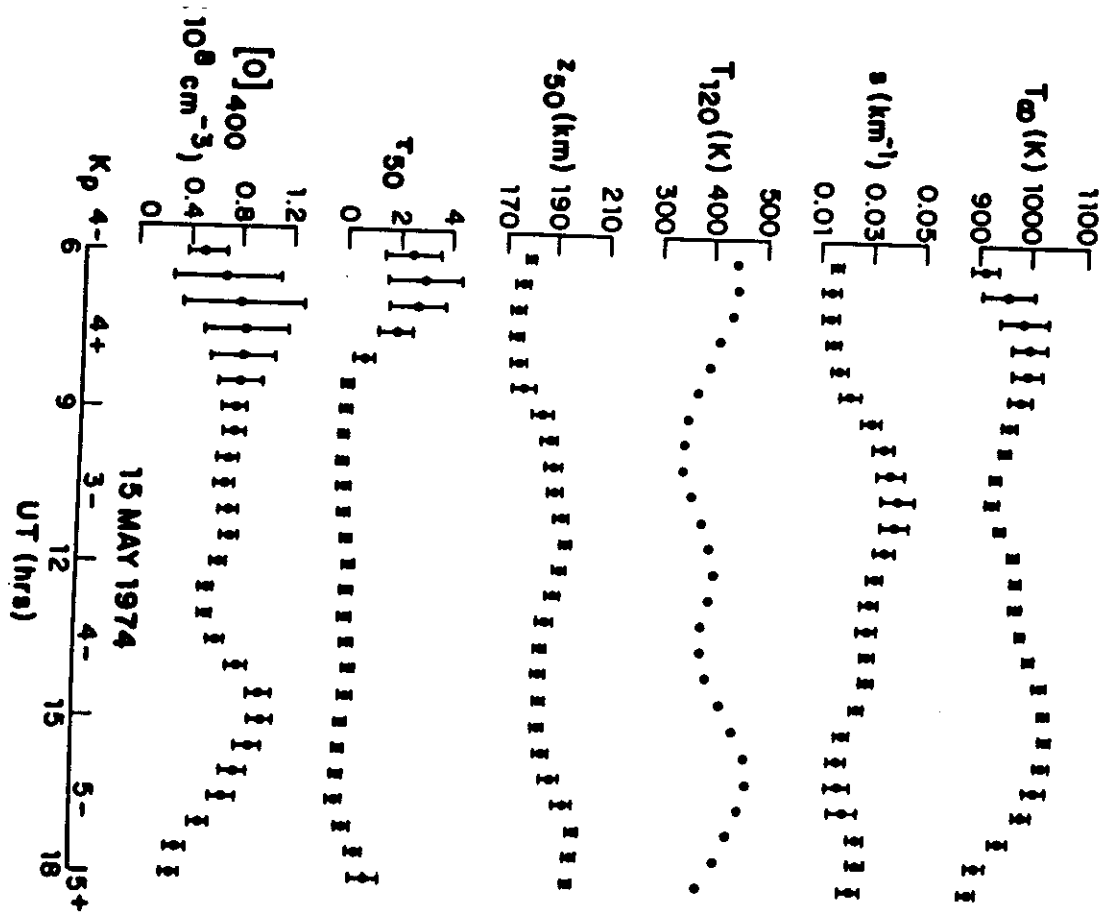
T_e (K)
1100
1000
900
α (km^{-1})
0.05
0.03
0.01
T_{120} (K)
500
400
300
z_{50} (km)
210
190
170
τ_{50}
4
2
0
$[O]_{400}$ (10^8 cm^{-3})
1.2
0.8
0.4
0
K_p
6
4+
9
3-
12
4-
15
5-
18
5+
UT (hrs)
15 MAY 1974

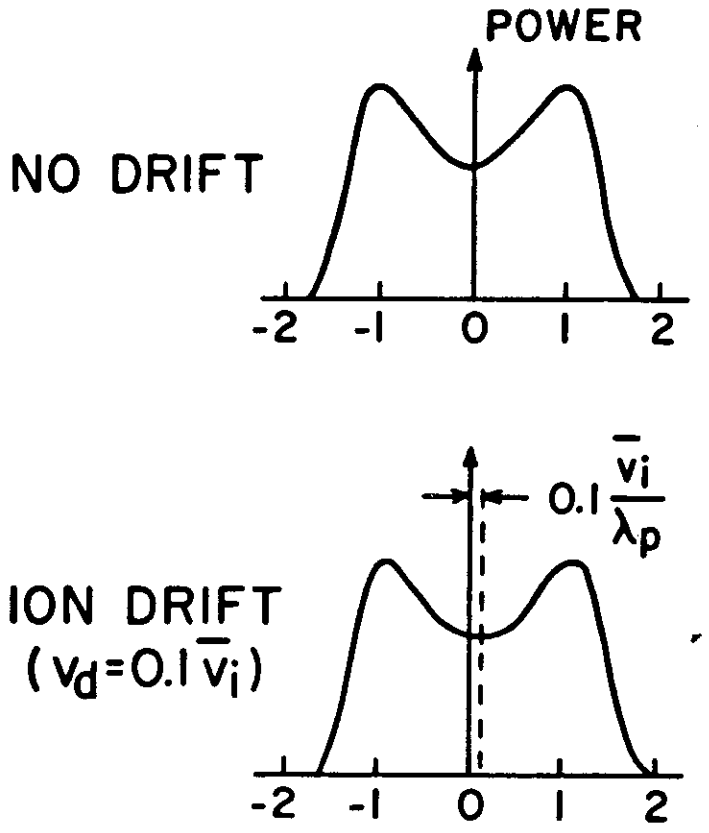
POWER
NO DRIFT
-2
-1
0
1
2
$0.1\frac{\bar{v}_i}{\lambda_p}$
ION DRIFT
($v_d = 0.1\bar{v}_i$)
-2
-1
0
1
2

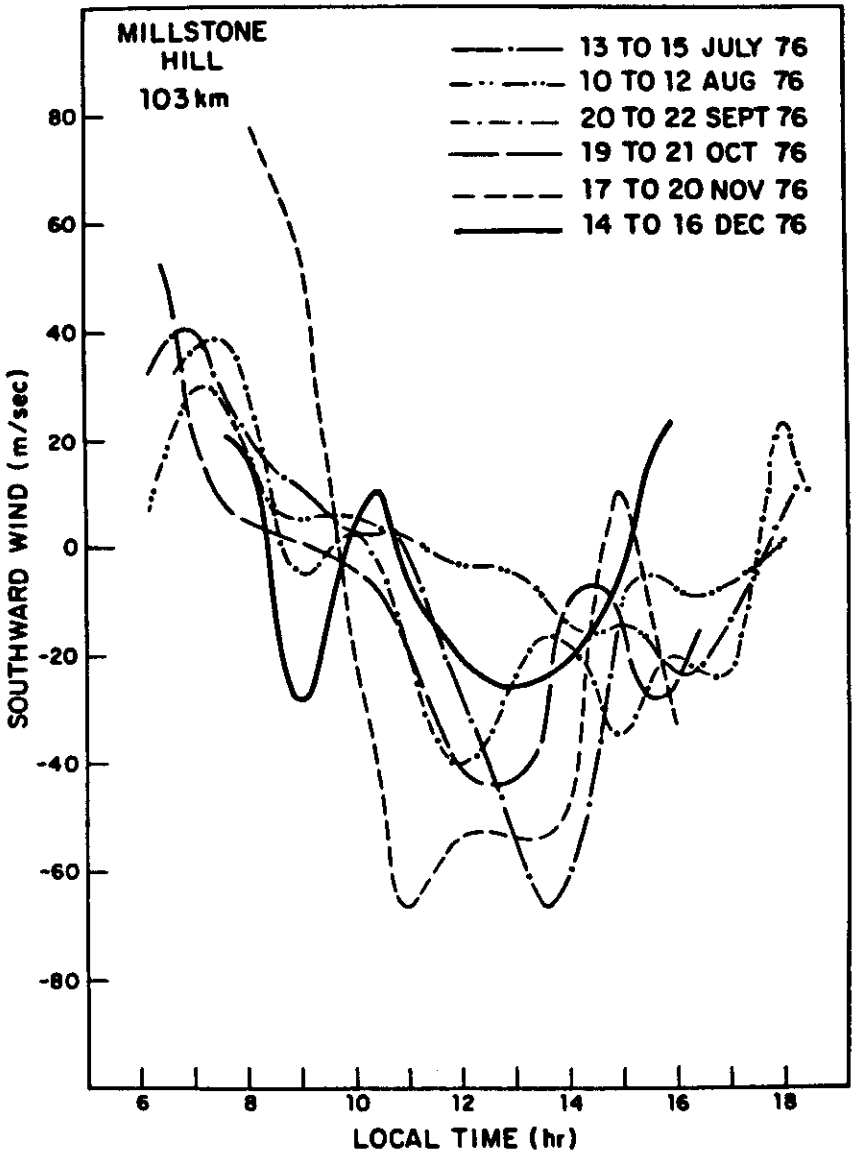
MILLSTONE
HILL
103 km
13 TO 15 JULY 76
10 TO 12 AUG 76
20 TO 22 SEPT 76
19 TO 21 OCT 76
17 TO 20 NOV 76
14 TO 16 DEC 76
SOUTHWARD WIND (m/sec)
80
60
40
20
0
-20
-40
-60
-80
6
8
10
12
14
16
18
LOCAL TIME (hr)

Fig. 31

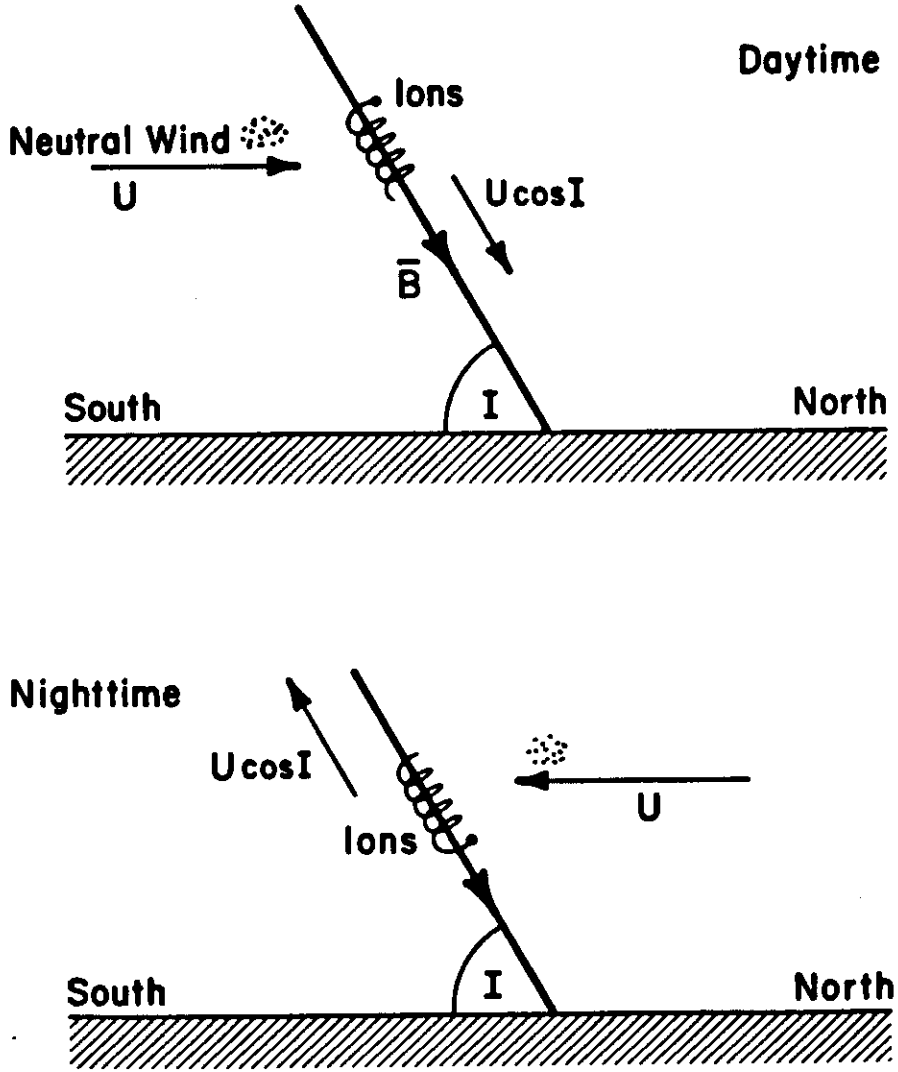
Daytime
Ions
Neutral Wind
U
UcosI
B
South
I
North
Nighttime
UcosI
U
Ions
South
I
North

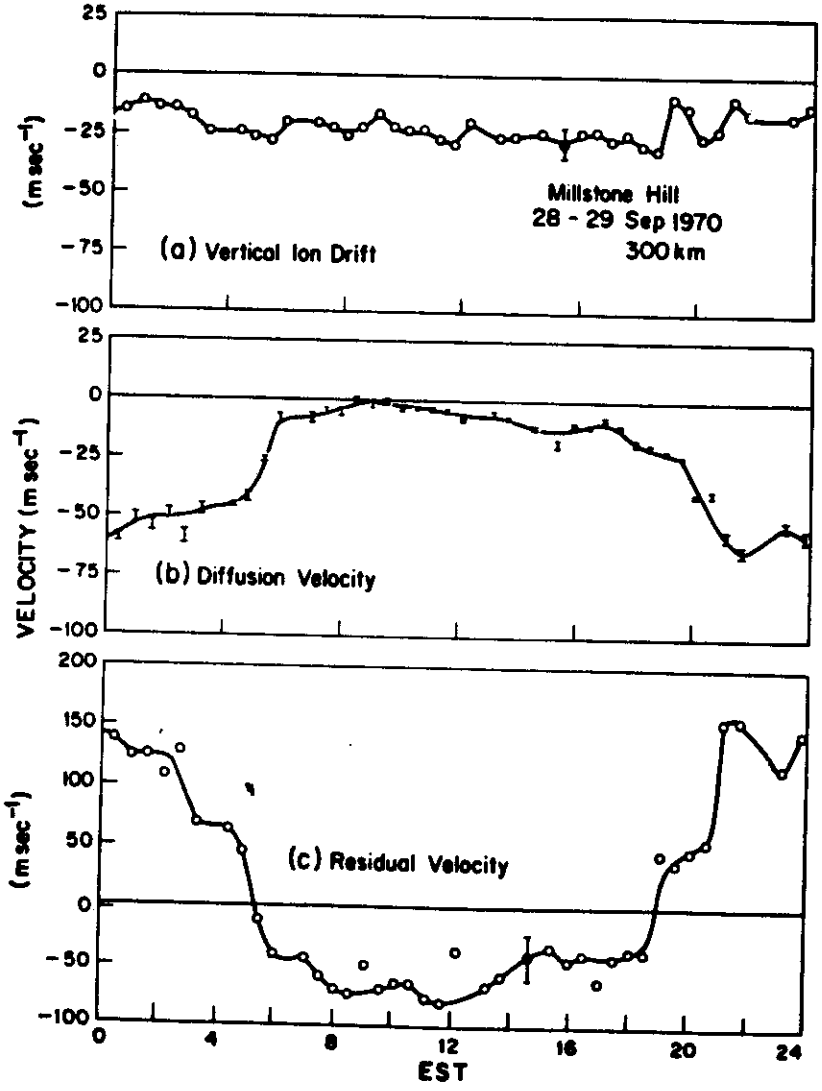
(m sec⁻¹)
Millstone Hill
28 - 29 Sep 1970
300 km
(a) Vertical Ion Drift
VELOCITY (m sec⁻¹)
(b) Diffusion Velocity
(m sec⁻¹)
(c) Residual Velocity
EST

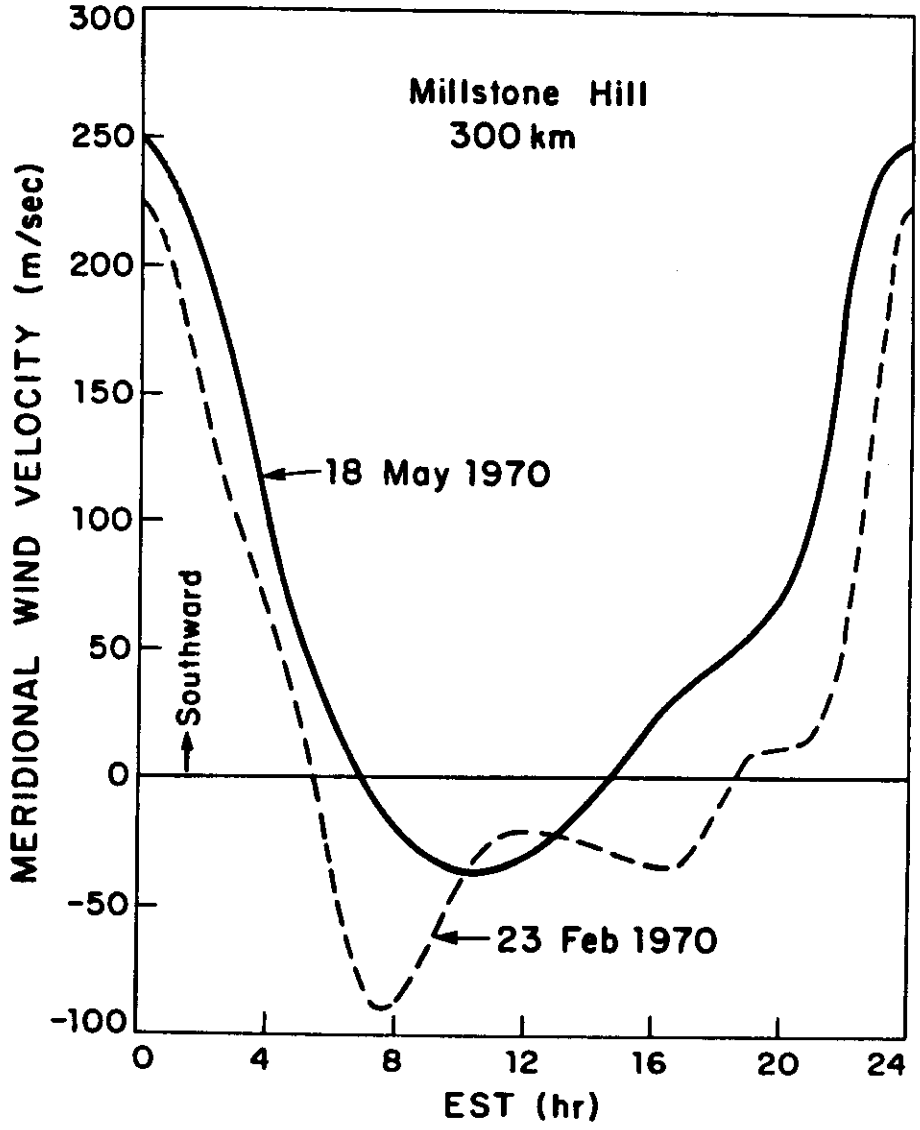
Millstone Hill
300 km
MERIDIONAL WIND VELOCITY (m/sec)
Southward
18 May 1970
23 Feb 1970
EST (hr)

Fig. 33

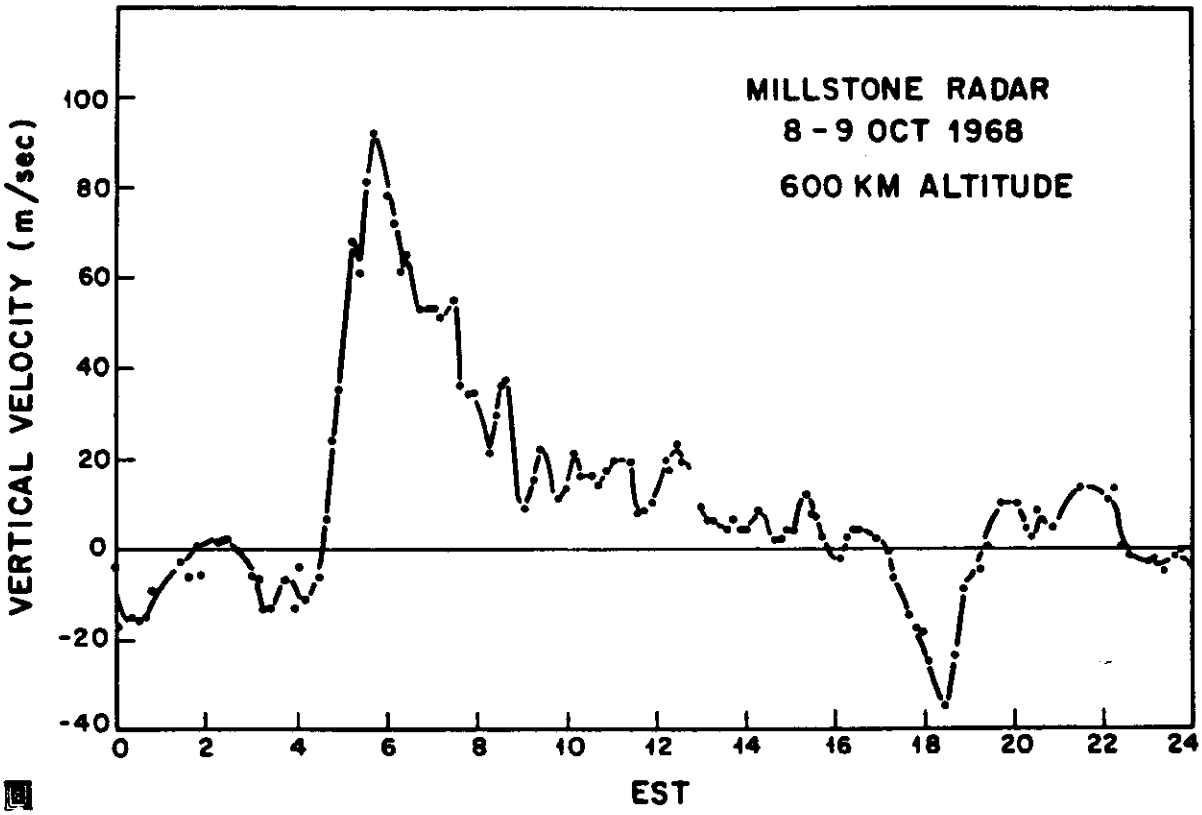
MILLSTONE RADAR
8 - 9 OCT 1968
600 KM ALTITUDE
VERTICAL VELOCITY (m/sec)
100
80
60
40
20
0
-20
-40
0
2
4
6
8
10
12
14
16
18
20
22
24
EST

Fig. 35

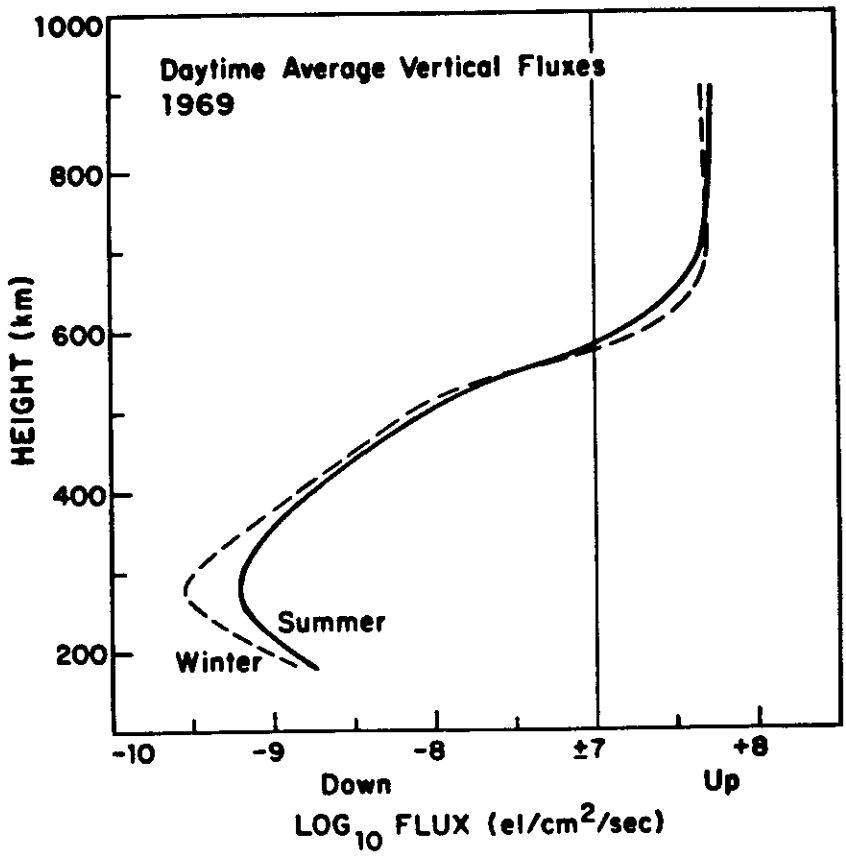
Daytime Average Vertical Fluxes
1969
HEIGHT (km)
1000
800
600
400
200
Summer
Winter
-10
-9
-8
±7
+8
Down
Up
LOG10 FLUX (el/cm2/sec)

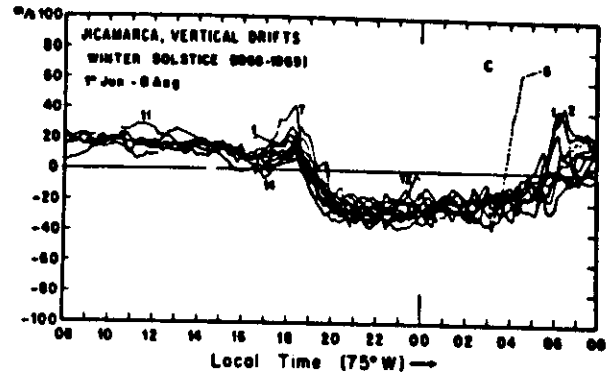
JICAMARCA, VERTICAL DRIFTS
WINTER SOLSTICE (1966-1969)
1st Jun - 8 Aug
C
Local Time (75°W)

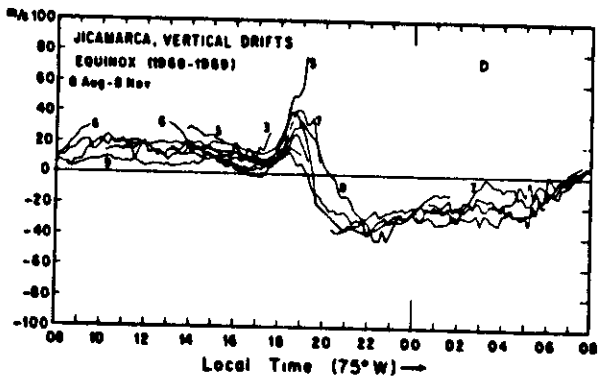
JICAMARCA, VERTICAL DRIFTS
EQUINOX (1966-1969)
8 Aug - 8 Nov
D
Local Time (75°W)

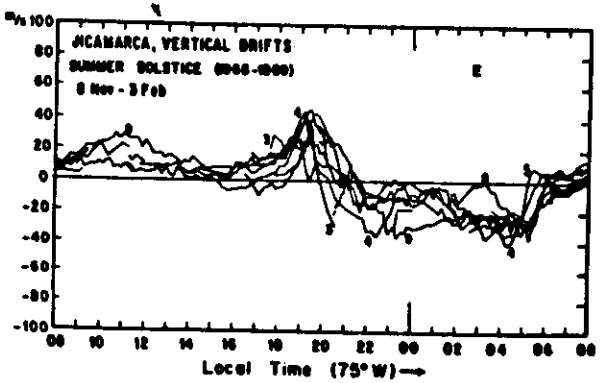
JICAMARCA, VERTICAL DRIFTS
SUMMER SOLSTICE (1966-1969)
8 Nov - 3 Feb
E
Local Time (75°W)

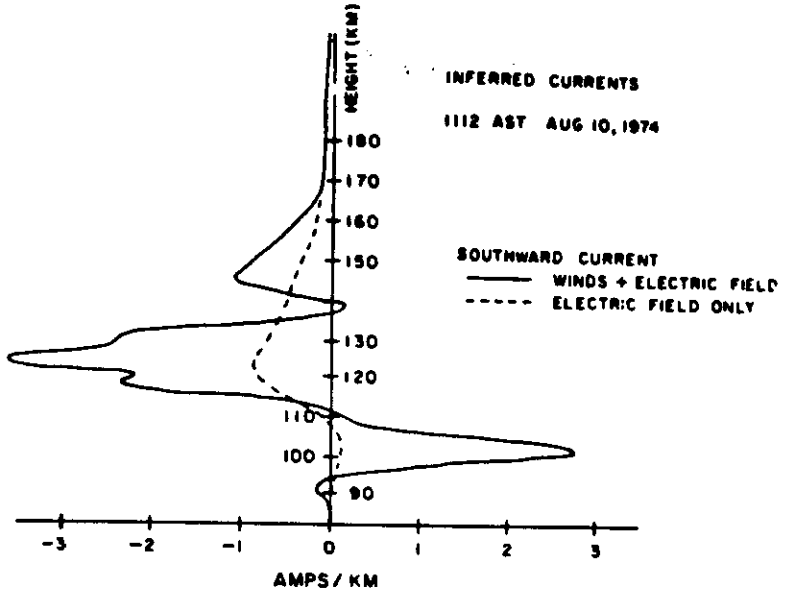
INFERRED CURRENTS
1112 AST AUG 10, 1974
SOUTHWARD CURRENT
WINDS + ELECTRIC FIELD
ELECTRIC FIELD ONLY
HEIGHT (KM)
AMPS / KM

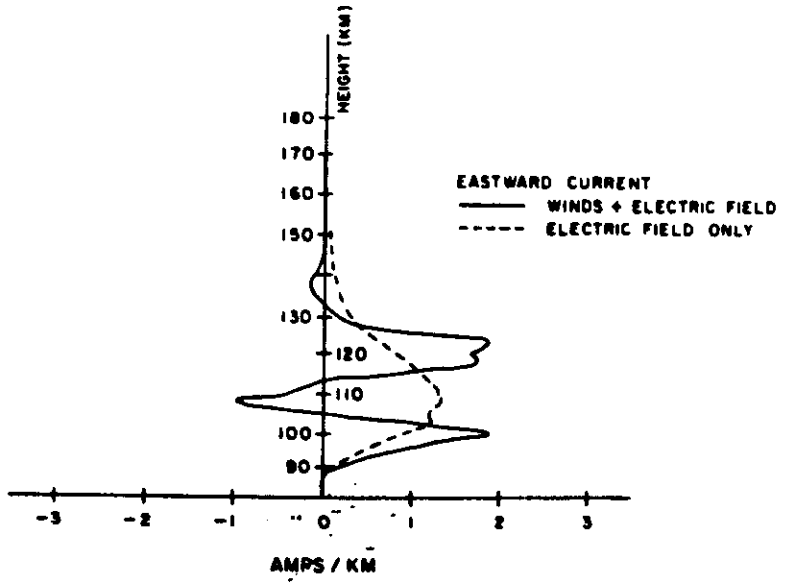
EASTWARD CURRENT
WINDS + ELECTRIC FIELD
ELECTRIC FIELD ONLY
HEIGHT (KM)
AMPS / KM

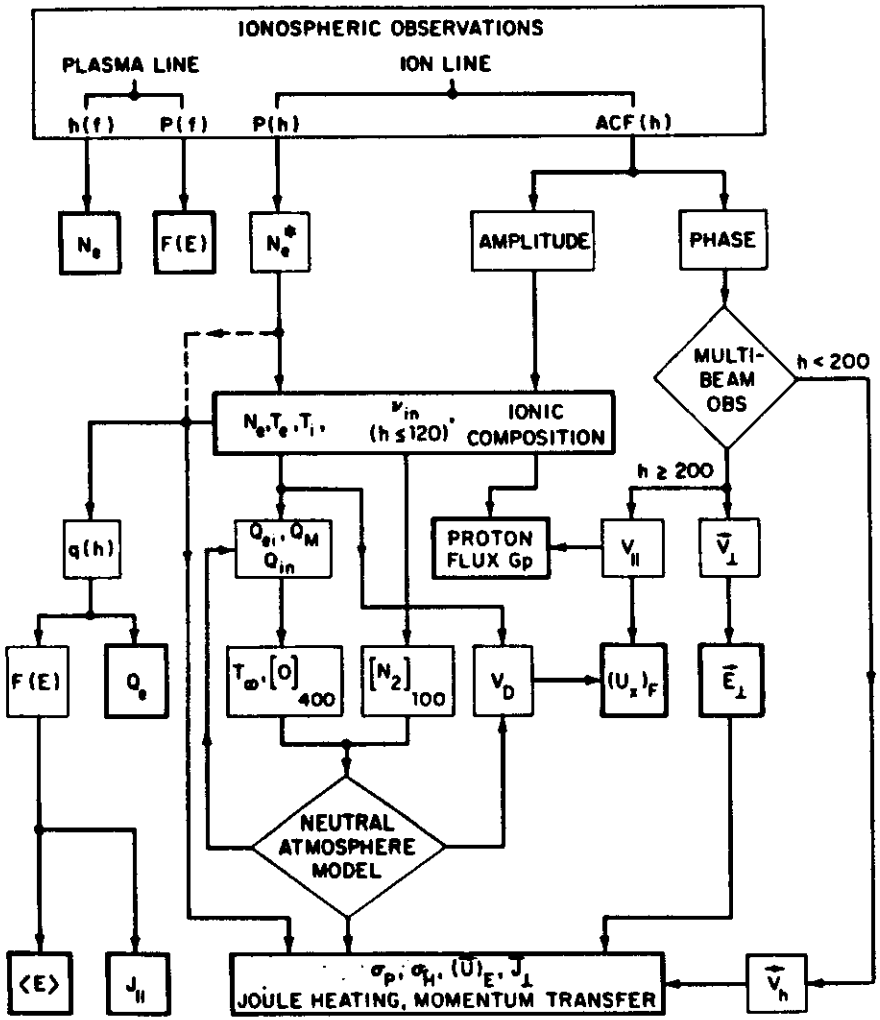
IONOSPHERIC OBSERVATIONS
PLASMA LINE
ION LINE
h(f)
P(f)
P(h)
ACF(h)
N_e
F(E)
N_e^*
AMPLITUDE
PHASE
MULTI-BEAM OBS
h < 200
$N_e, T_e, T_i,$ ν_{in} $(h \leq 120)$, IONIC COMPOSITION
h ≥ 200
q(h)
Q_{ei}, Q_M Q_{in}
PROTON FLUX Gp
$V_{\parallel}$
$\vec{V}_{\perp}$
F(E)
Q_e
$T_\infty, [O]_{400}$
$[N_2]_{100}$
V_D
$(U_x)_F$
$\vec{E}_{\perp}$
NEUTRAL ATMOSPHERE MODEL
<E>
$J_{\parallel}$
$\sigma_P, \sigma_H, (\vec{U})_E, \vec{J}_{\perp}$
JOULE HEATING, MOMENTUM TRANSFER
$\vec{V}_h$

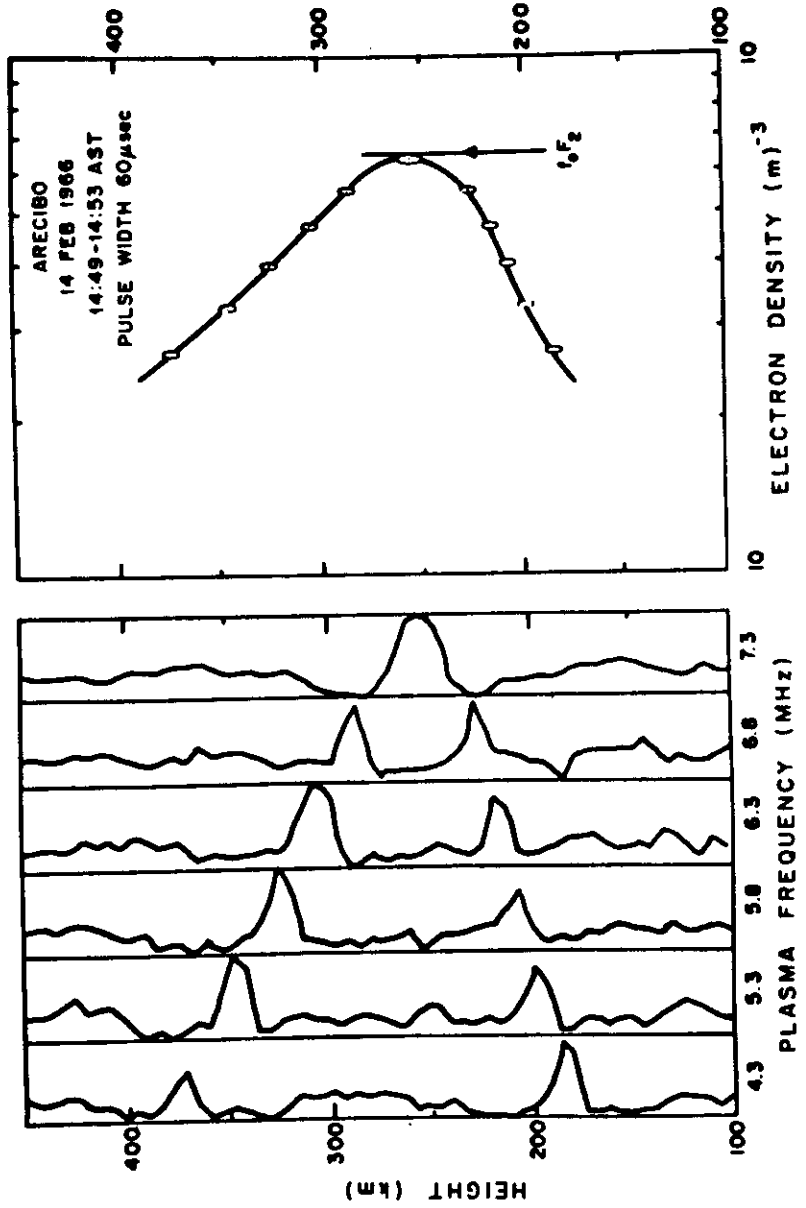
ARECIBO
14 FEB 1966
14:49-14:53 AST
PULSE WIDTH 60μsec
f_0F_2
400
300
200
100
10
10
ELECTRON DENSITY $(m)^{-3}$
7.3
6.8
6.3
5.8
5.3
4.3
PLASMA FREQUENCY (MHz)
HEIGHT (km)

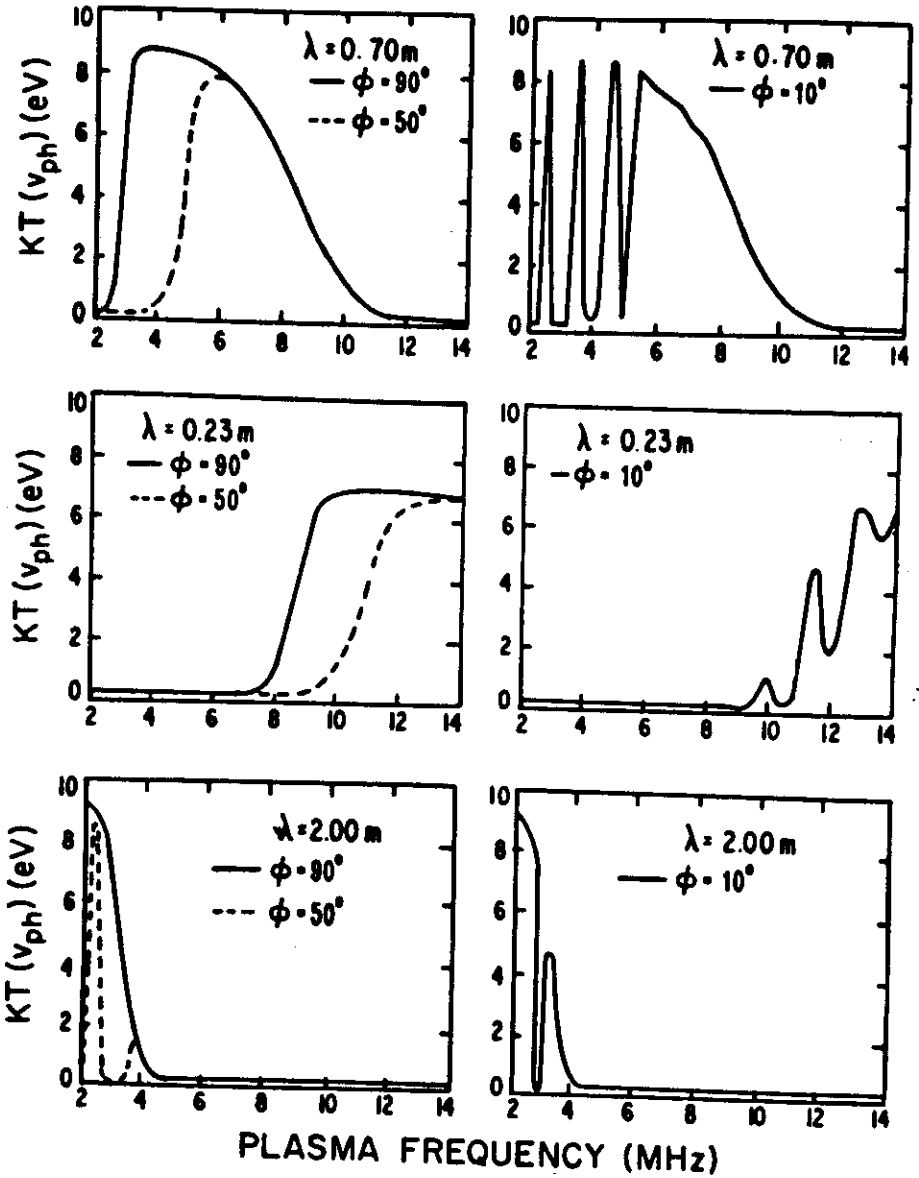
λ = 0.70 m
— ϕ = 90°
--- ϕ = 50°
λ = 0.70 m
— ϕ = 10°
λ = 0.23 m
— ϕ = 90°
--- ϕ = 50°
λ = 0.23 m
— ϕ = 10°
λ = 2.00 m
— ϕ = 90°
--- ϕ = 50°
λ = 2.00 m
— ϕ = 10°
KT (v_ph) (eV)
PLASMA FREQUENCY (MHz)

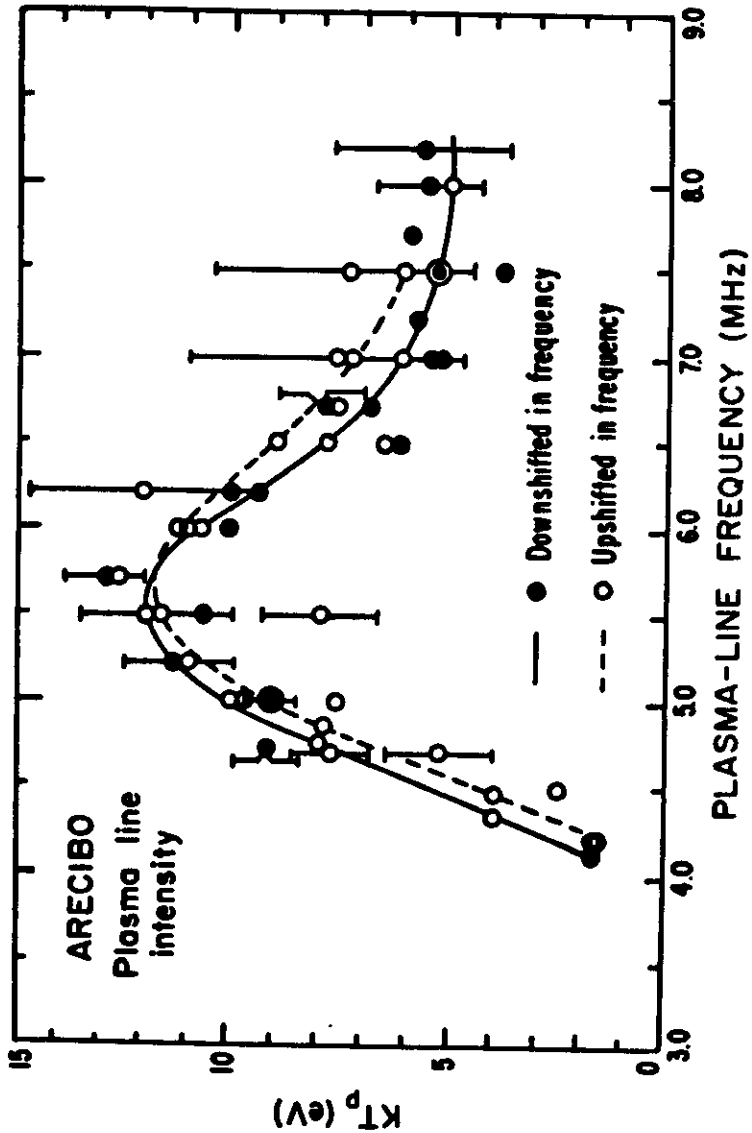
ARECIBO
Plasma line
intensity
● Downshifted in frequency
○ Upshifted in frequency
KT_p (eV)
PLASMA-LINE FREQUENCY (MHz)

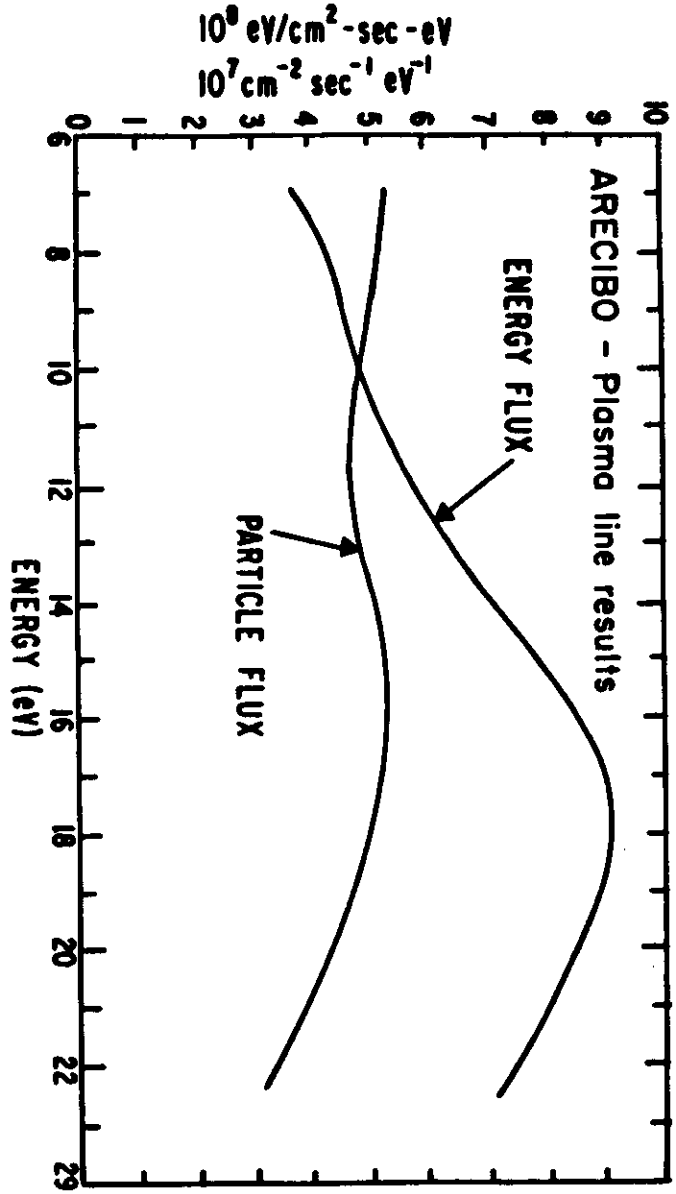

THERMAL FLUCTUATIONS IN A PLASMA.

T. Hagfors.

EISCAT Scientific Association, Kiruna, Sweden and
The University of Trondheim, Norway.

Abstract.

A derivation is presented of the fluctuation properties of a plasma near thermodynamic equilibrium. The derivation is based on the principle of superposition of dressed particles which allows the fluctuations to be derived from basic physical principles without prior knowledge of plasma physics.

The fluctuations in a magnetized plasma with unequal electron and ion temperatures are discussed in considerable detail, but the complications arising from ion-neutral collisions and from the presence of suprathermal particles are only briefly mentioned.

1.0. INTRODUCTION.

When spatial fluctuations or random refractive index fluctuations are present in a medium a wave cannot propagate through it without being randomly scattered into other directions. In most cases the spatial fluctuations are also time dependent and the time variation will be impressed as a modulation on the scattered wave.

Such scattering occurs with many types of waves and particle beams in a variety of physical situations. Here we shall be concerned only with the scattering of electromagnetic waves from a partly ionized plasma near thermodynamic equilibrium. We shall not deal with the much more difficult problem of turbulent plasmas.

There exists a profusion of theoretical work which derives the

properties of plasma density fluctuations [e.g. 1-6]. These density fluctuations are directly proportional to the refractive index fluctuations and are therefore of main interest to us here. The properties of the density fluctuation can be derived in many different ways, but it appears that the most direct method - requiring the least prior knowledge of plasma physics - is the one which relies on the superposition of independent dressed particles. For a development of the concept and a justification, please, refer to Rosenbluth and Rostoker [7].

2.0. RELATIONSHIP OF THE SCATTERING AND THE ELECTRON DENSITY FLUCTUATION.

Consider first the reradiation from a group of independent electrons in a volume V resulting from an incident plane monochromatic wave

$$\vec{E}(\vec{r},\ t) = \vec{E}_0 e^{i(\omega_0 t - \vec{\kappa}\cdot r)} \tag{2.1}$$

where

$$|\vec{\kappa}| = \omega_0/c$$

c = velocity of light $(3\cdot10^8 m/s)$

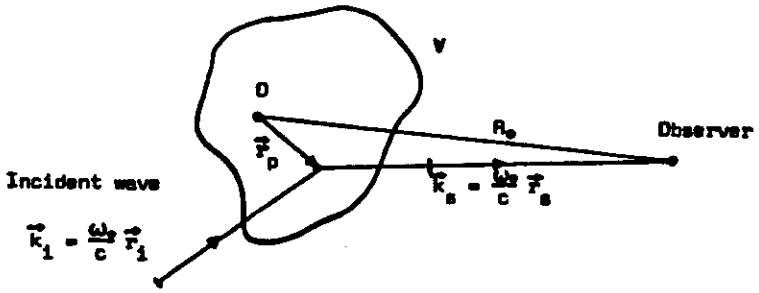

Fig. 1. Scattering by single electron.

The magnitude of the electric field from a single electron at $\vec{r}_p$ seen by the observer will be:

$$E_\phi = E_0 e^{i(\omega_0 t - \vec{k}_i\cdot\vec{r}_p(t))} \frac{1}{R_0} e^{-i\frac{\omega_s}{c}R_0} \sigma_0 e^{+i\vec{k}_s\cdot\vec{r}_p(t)} \tag{2.2}$$

where $\vec{k}_i$, $\vec{k}_s$ and R_0 are defined in Figure 1 and where σ_0 is the effective scattering "radius" of the electron defined by:

$$\sigma_0 = r_0\cdot\sin\alpha = \frac{e^2}{4\pi\varepsilon_0}\cdot\frac{1}{mc^2}\cdot\sin\alpha$$

$$= 2.91\cdot10^{-15}\cdot\sin\alpha \ (m) \tag{2.3}$$

where:

e = electron charge $(1.6\cdot10^{-19}C)$
m = electron mass $(9.1\cdot10^{-31}kg)$
ε_0 = dielectric constant of free space $(8.854\cdot10^{-12}F/m)$

The factor sinα takes into account the "coupling" between the incident wave and the scattered wave. When the incident wave is linearly polarized α is the angle between $\vec{E}_0$ and $\vec{k}_s$.

When many scattering electrons are present inside the volume V the observed field is given by the sum

$$E_{obs} = E_0 \frac{\sigma_0}{R_0} e^{i\omega_0(t-R_0/c)} \sum_{p=1}^{N} e^{i\vec{k}\cdot\vec{r}_p(t)} \tag{2.4}$$

where N is the total number of electrons in V and where:

$$\vec{k} = \vec{k}_s - \vec{k}_i \tag{2.5}$$

We next imagine the particle density to be expanded in a spatial Fourier series through:

$$n(\vec{r},\ t) = \frac{1}{V}\sum_{\vec{k}} n(\vec{k},\ t)e^{-i\vec{k}\cdot\vec{r}} \tag{2.6}$$

where

$$n(\vec{k},\ t) = \int_V d(\vec{r})n(\vec{r},\ t)e^{+i\vec{k}\cdot\vec{r}} \tag{2.7}$$

Since the scattering electrons must be considered point particles at $\vec{r}_p(t)$, p = 1,..N the density must be:

$$n(\vec{r},\ t) = \sum_{p=1}^{N} \delta(\vec{r}-\vec{r}_p(t)) \tag{2.8}$$

with a spatial spectrum

$$n(\vec{k},\ t) = \sum_{p=1}^{N} e^{+i\vec{k}\cdot\vec{r}_p(t)} = \sum_{p=1}^{N} n_p(\vec{k},\ t) \tag{2.9}$$

A comparison with (2.4) shows that the observed scattered field from the independent electrons may be expressed as:

$$E_{obs} = E_0 \frac{\sigma_0}{R_0} e^{i(t-R_0/c)\omega_0} \cdot n(\vec{k},\ t) \tag{2.10}$$

The complex amplitude of the received signal is:

$$A_{obs}(t) = \left(\frac{\sigma_0}{R_0} E_0\right) n(\vec{k},\ t) \tag{2.11}$$

The properties of the received signal can be described statistically by:

$$\left\langle A^*_{obs}(t) A_{obs}(t+\tau)\right\rangle = \left(\frac{\sigma_0 E_0}{R_0}\right)^2 \left\langle n^*(\vec{k},\ t) n(\vec{k},\ t+\tau)\right\rangle$$

$$= \left(\frac{\sigma_0 E_0}{R_0}\right)^2 n_0 \cdot V \left\langle n_p^*(\vec{k},\ t) n_p(\vec{k},\ t+\tau)\right\rangle \tag{2.12}$$

$$= \phi_p(\vec{r},\tau)$$

where n_0 is the mean electron density and where:

$$\left\langle n_p^*(\vec{k},\ t) n_p(\vec{k},\ t+\tau)\right\rangle = e^{i\vec{k}\cdot(\vec{r}_p(t+\tau)-\vec{r}_p(t))} \tag{2.13}$$

is the autocorrelation of density fluctuations associated with a single electron.

Similarly, the power spectrum received is determined from the Wiener-Khinchine's theorem

$$P_{obs}(\omega) = n_0 \cdot V \cdot P_{oe} \phi_p(\vec{k},\omega) \tag{2.14}$$

where P_{oe} is the power scattered by an individual electron under the same geometrical conditions and where:

$$\phi_p(\vec{k},\omega) = \int_{-\infty}^{+\infty} \left\langle n_p(\vec{k},\ t) n(\vec{k},\ t+\tau)\right\rangle e^{-i\omega\tau} d\tau =$$

$$= \int_{-\infty}^{+\infty} \left\langle e^{i\vec{k}(\vec{r}_p(t+\tau)-\vec{r}_p(t))}\right\rangle \cdot e^{-i\omega\tau} d\tau$$

$$= \int_{-\infty}^{+\infty} \rho_p(\vec{k},\ \tau) e^{-i\omega\tau} d\tau$$

We often need the integral:

$$G(\vec{k},\omega) = \int_{0}^{\infty} \rho_p(\vec{k},\tau) e^{-i\omega\tau} d\tau$$

With this function the spectrum of a particle becomes

$$\phi_p(\vec{k},\omega) = 2 \cdot \mathrm{Re}(G(\vec{k},\omega)).$$

3.0. PLASMA OF NON-INTERACTING PARTICLES.

It will become apparent in the next two sections that both the plasma response to an electric field as well as the thermal driving force can be described on the basis of the motion of non-interacting particles. It is, therefore, useful to study their motion in some detail. Both electrostatic interaction and some short-range collisional interactions can be accounted for.

We assume that the static magnetic field $\vec{B}_0$ is directed along the z-axis. It will be convenient to introduce "polarized" coordinates to describe the position of a particle:

Cartesian:	Polarized:	
$\vec{r} = \{x,\ y,\ z\}$	$\vec{r} = \{r_{+1},\ r_{-1},\ r_0\}$	(3.1)

The relationship between the two descriptions is

$$r_1 = \frac{1}{\sqrt{2}}(x+iy)$$

$$r_{-1} = \frac{1}{\sqrt{2}}(x-iy) \tag{3.2}$$

$$r_0 = z$$

The advantage of these polarized coordinates becomes evident when we state the equation of motion of a particle:

$$\frac{dv_\alpha}{dt} = -i\alpha\Omega v_\alpha \qquad (\alpha = \pm 1, 0) \tag{3.3}$$

$$\Omega = \frac{qB_0}{m}$$

where q and m are the charge and the mass of the particle (electron or ion) respectively. From this we determine the relationship between the velocity at time $t' = t-\tau$ in terms of the present velocity (at t)

$$\vec{v}(t-\tau) = \dot{\Gamma}(\tau)\vec{v}(t) \tag{3.4}$$

where $\dot{\Gamma}(\tau)$ is a diagonal matrix with elements.

$$(\dot{\Gamma}(\tau))_{\alpha\alpha} = e^{i\alpha\Omega\tau} = \dot{g}_\alpha(\tau) \tag{3.5}$$

The past particle position can be determined similarly in terms of present position and present velocity through

$$\vec{r}(t-\tau) = \vec{r}(t) - \Gamma(\tau)\vec{v}(t) \tag{3.6}$$

where $\Gamma(\tau)$ is a diagonal matrix which determines the particle helical motion. The elements are given by

$$(\Gamma(\tau))_{\alpha\alpha} = \frac{e^{i\alpha\Omega\tau} - 1}{i\alpha\Omega} = g_\alpha(\tau) \qquad (\alpha = \pm 1, 0) \tag{3.7}$$

The single particle autocorrelation, eq. (2.13) now becomes:

$$\rho_p(\vec{k},\tau) = \left\langle e^{i\vec{a}\cdot\vec{v}} \right\rangle \tag{3.8}$$

where

$$a_\alpha = k_\alpha \cdot g_{-\alpha} \tag{3.9}$$

The actual form of $\rho_p(\vec{k},\tau)$ depends on the statistical distribution of velocities, the magnetic field strength and the angle β between $\vec{k}$ and the magnetic field direction. For a Maxwellian velocity distribution:

$$f_0(\vec{v}) = (2\pi)^{-3/2} v_{th}^{-3} e^{-v^2/2v_{th}^2} \tag{3.10}$$

where

$$v_{th}^2 = T/m$$

T = kinetic temperature (in energy units)

and obtains

$$\rho_p(\vec{k},\tau) = e^{-\frac{1}{2}v_{th}^2|\vec{a}|^2}$$

$$= e^{-(kR)^2\left\{(\frac{\Omega\tau}{2})^2\cos^2\beta + \sin^2(\frac{\Omega\tau}{2})\sin^2\beta\right\}} \tag{3.11}$$

The gyration radius R is given by:

$$R = \frac{\sqrt{2}v_{th}}{\Omega}$$

It equals the ratio of the r.m.s. orbital velocity and the angular gyration frequency.

We note that for weak magnetic fields and arbitrary β, or for $\vec{k} \parallel \vec{B}_0$ (i.e. $\beta=0$) and arbitrary magnetic field strength the autocorrelation becomes

$$\rho_0(\vec{k},\tau) \to e^{-\frac{1}{2}(kv_{th}\tau)^2} \tag{3.12}$$

When $\vec{k}$ is exactly perpendicular to the magnetic field the autocorrelation for the plasma-density becomes periodic with period $T = 2\pi/\Omega$. The depth of modulation increases with R and decreases with the scale of the density fluctuation $\Lambda = 2\pi/k$, see Figure 2.

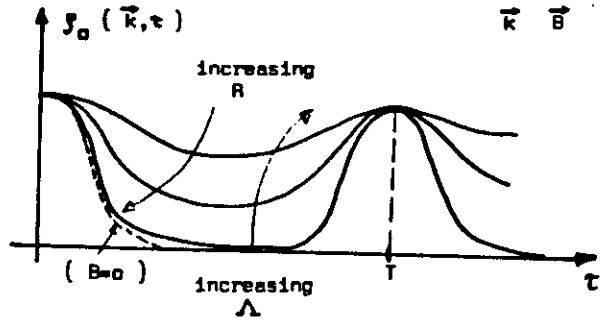

Fig. 2. Autocorrelation of density fluctuation when $\vec{k} \perp \vec{B}$

For intermediate angles between $\vec{k}$ and $\vec{B}_0$ the autocorrelation of the density fluctuation can be regarded a product of two factors, see 3.11.

$$\text{A)}\quad e^{-(kR)^2(\frac{\Omega\tau}{2})^2\cos^2\beta}$$

$$\text{B)}\quad e^{-(kR)^2\sin^2(\frac{\Omega\tau}{2})\cdot\sin^2\beta}$$

which are sketched in Fig. 3.

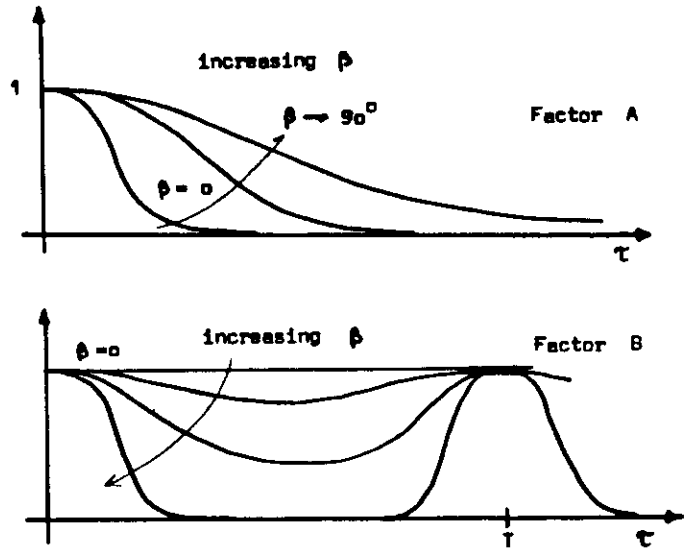

Fig. 3. The two factors which determine the autocorrelation of the independent particle density fluctuations.

The spectral function $\phi(\vec{k},\omega)$ becomes

$$\phi_p(\vec{k},\omega) = 2\mathrm{Re}\left\{G_p(\vec{k},\omega)\right\} \tag{3.13}$$

where

$$G_p(\vec{k},\omega) = \int_0^\infty e^{-\frac{1}{2}v_{th}^2|\vec{a}_p|^2 - i\omega\tau}\,d\tau \tag{3.14}$$

4.0. THE RESPONSE TO AN IMPRESSED CHARGE.

We shall now introduce particle correlations in the various plasma components (electrons, various types of ions) by considering the particles smeared out into a continuum and by assessing the response of this continuum to each discrete particle separately.

The plasma response to an electric field $\vec{E}(\vec{r},t)$ can be obtained by solving the Vlasov equation to first order in $\delta n(\vec{r},\vec{v},t)$ and $\vec{E}(\vec{r},t)$. The perturbation solution for any of the species is given by:

$$\delta n(\vec{r},\vec{v},t) = -\frac{n_0 q}{m}\int_{-\infty} \vec{E}(\vec{r},t')\frac{\partial f_0'}{\partial \vec{v}'}dt' \tag{4.1}$$

Here $\vec{E}(\vec{r},t)$ is a small electric field which we shall later assume set up by the fluctuating charges. The integration is carried out along the unperturbed particle orbits which were studied in Section 3.

We make the following substitutions:

$$t' = t-\tau$$

$$\vec{E}(\vec{r}',t') = \frac{1}{V}\sum_{\vec{k}}\vec{E}(\vec{k},t-\tau)e^{-i\vec{k}\cdot\vec{r}}\,e^{+i\vec{k}\cdot\vec{r}(\tau)\vec{v}} \tag{4.2}$$

$$\frac{\partial f_0}{\partial \vec{v}'} = \dot{\vec{r}}(\tau)\,\frac{\partial f_0(v')}{\partial \vec{v}}$$

Integrating over all possible $\vec{v}$ we obtain the induced density fluctuation:

$$n^1(\vec{k},t) = -\frac{n_0 q}{m}\int_{-\infty}^{\infty} d\tau\vec{E}(\vec{k},t-\tau)\int d(\vec{v})\dot{\vec{r}}(\tau)\,\frac{\partial f_0(\vec{v}')}{\partial \vec{v}}e^{i\vec{k}\cdot\vec{r}(\tau)\vec{v}} \tag{4.3}$$

We now take the Fourier transform with respect to time, and relate the electrical field to the <u>total</u> electric charge fluctuation $Q(\vec{k},\omega)$:

$$\vec{E}(\vec{k},\omega) = \frac{i\vec{k}}{\varepsilon_0 k^2}Q(\vec{k},\omega) \tag{4.4}$$

We only include the longitudinal electrostatic field. It is possible to show that the transverse field is unimportant in this context.

Substitution of 4.4 into 4.3 gives

$$n^1(\vec{k},\omega) = -\frac{in_0 q}{\epsilon_0 m \cdot k^2} Q(\vec{k},\omega) \int_0^\infty d\tau \cdot e^{-i\omega\tau} \int d(\vec{v}) \dot{\vec{a}}(\tau) \frac{\partial f_0}{\partial \vec{v}} e^{-i\vec{a}\cdot\vec{v}} \tag{4.5}$$

For each of the species we now introduce

$$\frac{n_{0\sigma} q_\sigma^2}{\epsilon_0 m_\sigma} = \omega_\sigma^2$$

and:
$$\chi_\sigma = +i \frac{\omega_\sigma^2}{k^2} \int_0^\infty d\tau\, e^{-i\omega\tau} \int d(\vec{v}) \dot{\vec{a}}_\sigma(\tau) \cdot \frac{\partial f_0}{\partial \vec{v}} e^{+i\vec{a}_\sigma \cdot \vec{v}} \tag{4.6}$$

Hence, we obtain for the fluctuation induced in species c:

$$n_\sigma^1(\vec{k},\omega) = -\frac{1}{q_\sigma} \chi_\sigma(\vec{k},\omega) \cdot Q(\vec{k},\omega) \tag{4.7}$$

We are now in a position to compute the density fluctuations in the plasma.

5. CALCULATION OF FLUCTUATIONS.

Let us now assume that we have a plasma of electrons and one type of singly charged ions.

For the electrons we put:	For the ions we put:
$\omega_\sigma^2 \to \omega_e^2$	$\omega_\sigma^2 \to \omega_i^2$
$q_\sigma \to -e$	$q_\sigma \to +e$
$m_\sigma \to m$	$m_\sigma \to M$
$\vec{a}_\sigma \to \vec{a}_e$	$\vec{a}_\sigma \to \vec{a}_i$
$f_{0\sigma} \to f_0$	$f_{0\sigma} \to F_0$
$\chi_\sigma \to \chi_e$	$\chi_\sigma \to \chi_i$
$n_\sigma \to n$	$n_\sigma \to N$

Consider first the fluctuation associated with a particular electron.

A. Intrinsic fluctuation $n_p(\vec{k},\omega)$, see Section 3.

B. Induced electron fluctuation (electron dressing on electron) $\quad n_e^1(\vec{k},\omega) = +\frac{\chi_e}{e} Q_e(\vec{k},\omega)$

C. Induced ion fluctuation (ion-dressing on electron) $\quad N_e^1(\vec{k},\omega) = -\frac{\chi_i}{e} Q_e(\vec{k},\omega)$

The total charge fluctuation associated with this single electron is

$$Q_e(\vec{k},\omega) = -e\left(n_p + \frac{\chi_e}{e} Q_e\right) + e\left(-\frac{\chi_i}{e} Q_e\right) \tag{5.1}$$

from which:

$$Q_e(\vec{k},\omega) = \frac{-e \cdot n_p(\vec{k},\omega)}{1 + \chi_e + \chi_i} \tag{5.2}$$

Since we are interested in the total electron-density fluctuation induced by electrons, not the charge fluctuation, we have:

$$\begin{aligned} n_e(\vec{k},\omega) &= n_p(\vec{k},\omega) + n^1(\vec{k},\omega) \\ &= n_p(\vec{k},\omega) + \frac{-\chi_e n_p(\vec{k},\omega)}{1+\chi_e+\chi_i} = \frac{n_p(\vec{k},\omega)(1+\chi_i)}{1+\chi_e+\chi_i} \end{aligned} \tag{5.3}$$

The mean power spectrum associated with the thermal excitation by electrons is, therefore, found by averaging over the electron velocity distribution. If the velocity distribution is Maxwellian (3.10), then the independent electron spectrum is given by 3.13 and the result is

$$|n_e(\vec{k},\omega)|^2 = \frac{|n_p(\vec{k},\omega)|^2 \, |1+\chi_i|^2}{|1+\chi_e+\chi_i|^2} = \frac{\Phi_e(\vec{k},\omega)\,|1+\chi_i|^2}{|1+\chi_e+\chi_i|^2} \tag{5.4}$$

where $\Phi_e(\vec{k},\omega)$ is the independent single electron mean power spectrum discussed in Section 3.
Next consider the more important fluctuation arising from the thermal motion of an ion:

A. Intrinsic fluctuation $N_p(\vec{k},\omega)$, see Section 3.

B. Induced electron fluctuation $n_i^1(\vec{k},\omega) = + \frac{\chi_e}{e} Q_i(\vec{k},\omega)$
(electron dressing on ion)

C. Induced ion fluctuation $N_i^1(\vec{k},\omega) = - \frac{\chi_i}{e} Q_i(\vec{k},\omega)$

Solving for the charge fluctuation $Q_i(\vec{k},\omega)$ we obtain:

$$Q_i(\vec{k},\omega) = \frac{eN_p(\vec{k},\omega)}{1 + \chi_e + \chi_i} \tag{5.5}$$

and the fluctuation induced in the electron density is given by:

$$n_i^1(\vec{k},\omega) = \frac{\chi_e N_p(\vec{k},\omega)}{1 + \chi_e + \chi_i} = n_i(\vec{k},\omega) \tag{5.6}$$

The total electron density fluctuation in the plasma therefore can be expressed in terms of the independent particle spectra for electrons and ions and the response functions of the plasma as follows:

$$\begin{aligned} |n(\vec{k},\omega)|^2 &= (|n_e(\vec{k},\omega)|^2 + |n_i(\vec{k},\omega)|^2) n_0 \cdot V \\ &= \frac{|1+\chi_i|^2 \phi_e(\vec{k},\omega) + |\chi_e|^2 \phi_i(\vec{k},\omega)}{|1 + \chi_e + \chi_i|^2} n_0 V \end{aligned} \tag{5.7}$$

Which is the form of the spectrum which has been widely used in the analysis of the incoherent scatter data.

Note that fluctuations in ion density, charge density, electric field, currents etc. can all be obtained by an analogous procedure. Note also that an extension to a multi-ionplasma is relatively trivial and that different temperatures for electrons and ions are allowed.

Collisions have not been considered but can, in some cases, be taken into account by regarding the particle motion, Section 3, as a stochastic rather than a deterministic process.

6.0. DISCUSSION OF RESULT.

The spectrum function 5.7 contains the χ_e and χ_i together with ϕ_e and ϕ_i. All of these functions are related to the autocorrelati: of independent particle fluctuations as follows:

Introduce for electrons (see 3.11):

$$\rho_0(\vec{k},\tau) = \rho_e(\vec{k},\tau) = e^{-\frac{1}{2}v_{th}^2 |\vec{a}|^2}$$

$$v_{th}^2 = \frac{T_e}{m}$$

$$a_{-\alpha} = k_{-\alpha} \cdot g_\alpha \qquad (g_\alpha \text{ computed with } \Omega = \Omega_e = - \frac{eB_0}{m})$$

$$D_e^2 = \frac{\epsilon_0 T_e}{n_0 \cdot e^2}$$

And for the ions:

$$\rho_0(\vec{k},\tau) = \rho_i(\vec{k},\tau) e^{-\frac{1}{2}v_{th}^2 |\vec{A}|^2}$$

$$v_{th}^2 = \frac{T_i}{M}$$

M = ionic mass

$$A_{-\alpha} = k_{-\alpha} \cdot g_\alpha \qquad (g_\alpha \text{ computed with } \Omega = \Omega_i = + \frac{eB_0}{M})$$

$$D_i^2 = \frac{\epsilon_0 T_i}{n_0 \cdot e^2}$$

With these definitions we obtain, see also 3.13 and 3.14:

$$\chi_e(\vec{k},\omega) = (\frac{1}{k\, D_e})^2 (1 + \omega \cdot \mathrm{Im}\{G_e(\vec{k},\omega)\} - i\omega \cdot \mathrm{Re}\{G_e(\vec{k},\omega)\})$$

$$\chi_i(\vec{k},\omega) = (\frac{1}{k\, D_i})^2 (1 + \omega \cdot \mathrm{Im}\{G_i(\vec{k},\omega)\} - i\omega \cdot \mathrm{Re}\{G_i(\vec{k},\omega)\})$$

and:

$$\phi_e(\vec{k},\omega) = 2 \cdot \mathrm{Re}\{G_e(\vec{k},\omega)\}$$

$$\phi_i(\vec{k},\omega) = 2 \cdot \mathrm{Re}\{G_i(\vec{k},\omega)\}$$

Here, from 3.14:

$$\mathrm{Re}\left\{G_e(\vec{k},\omega)\right\} = \int_0^\infty e^{-\frac{1}{2}v_{th}^2|\vec{a}|^2}\cos\omega\tau\, d\tau$$

$$\mathrm{Im}\left\{G_e(\vec{k},\omega)\right\} = -\int_0^\infty e^{-\frac{1}{2}v_{th}^2|\vec{a}|^2}\sin\omega\tau\, d\tau$$

with a similar definition for the ions.

When there is no magnetic field or when $\vec{k} \parallel \vec{B}_0$ one obtains:

$$\omega\mathrm{Re}\left\{G(\vec{k},\omega)\right\} = \sqrt{\frac{\pi}{2}}\, z\, e^{-\frac{1}{2}z^2}$$

$$1+\omega\mathrm{Im}\left\{G(\vec{k},\omega)\right\} = \begin{cases} 1 - z^2 + \frac{1}{3}z^4 - \frac{1}{15}z^6 \ldots\ldots & z \ll 1 \\ -\frac{1}{z^2} - \frac{3}{z^4} - \ldots\ldots & z \gg 1 \end{cases}$$

where we have put

$$z = \frac{\omega}{kv_{th}} = \frac{v_\phi}{v_{th}}$$

The only difference in the electronic and the ionic functions comes from the difference in thermal velocities.

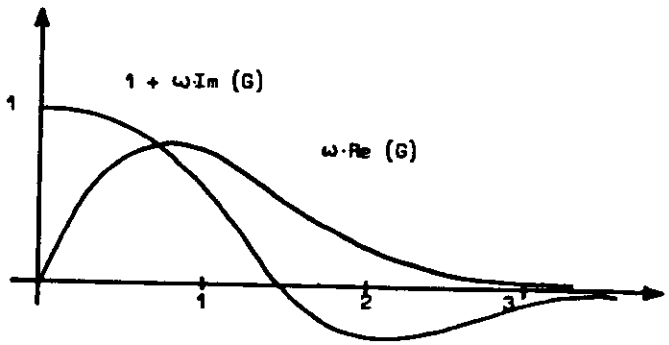

Fig. 4. Plasma dispersion functions.

For values of ω such that $\omega < kV_{th}$ χ_i and χ_e are of the same order of magnitude.
However, $\phi_e/\phi_i \sim \mathrm{Re}\left(G_e\right)/\mathrm{Re}\left(G_i\right) \sim v_{th}/v_{th} \sim \sqrt{m/M}$

It follows that as long as kD_e and kD_i $\gg 1$ the dominant excitation of density waves at low frequencies must stem from the ion excitation, see the numerator of (5.7). In the denominator $\chi_e = (\frac{1}{kD_e})^2$ whenever $\omega < kV_{th}$. It follows that the low frequency part of the spectrum simplifies to:

$$|n(\vec{k},\omega)|^2 = 2n_0 V \frac{\mathrm{Re}\left\{G_i(\omega,\vec{k})\right\}}{\left|1 + \frac{T_e}{T_i}(1 - i\omega G_i(\omega,\vec{k}))\right|^2}$$

For $T_e = T_i$ the factor multiplying $\mathrm{Re}\left\{G_i(\omega,\vec{k})\right\}$ starts at $\frac{1}{4}$ at $\omega = 0$. As T_e/T_i increases above unity the depression near $\omega = 0$ increases and a near line spectrum develops, see Figure 5.

When kD_e and kD_i became much larger than unity, then the electronic part of the spectrum will dominate and we obtain a Gaussian spectrum with a width corresponding to the thermal motion of electrons, see Fig. 6.

A resonance occurs near the electron plasma frequency ω_e. This can be established by looking for a zero in the denominator of (5.7) near the plasma frequency. Since χ_i has vanished near ω_e we have:

$$1 + (\frac{1}{kD_e})^2\left\{1 + \omega\mathrm{Im}(G_e) - i\omega\mathrm{Re}(G_e)\right\} = 0$$

In Order for a resonance to develop it is necessary that $\omega_e > kv_{th}$.

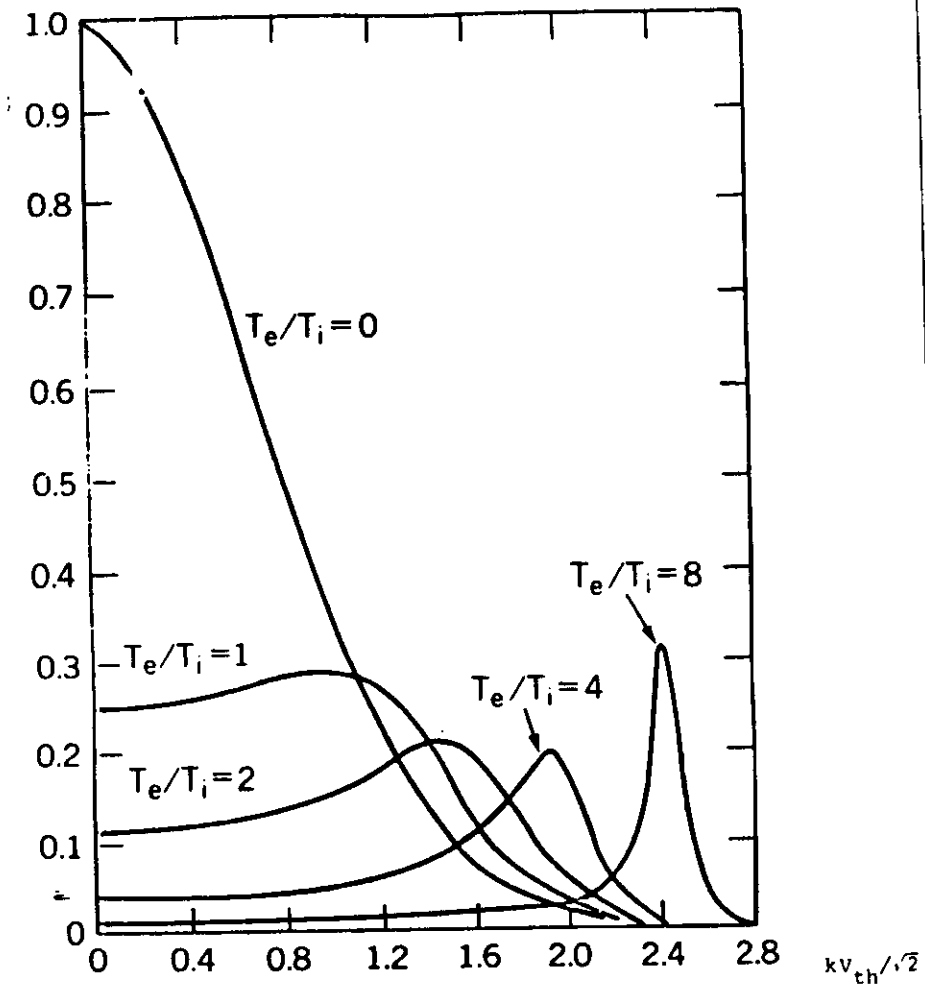

Fig. 5. Variation in the ionic spectrum with T_e/T_i.

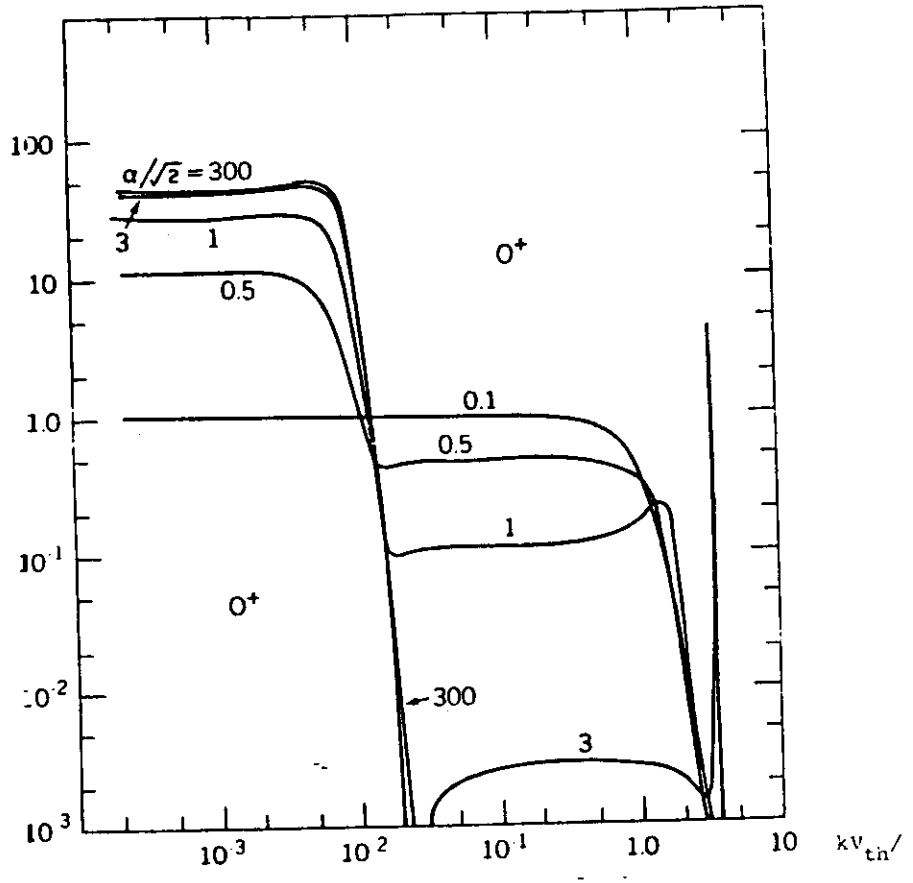

Fig. 6. Equilibrium spectra for various values of $(kD) = \sqrt{2}/a$.

As ω is close to ω_e the expansion of the plasma dispersion functions for large arguments can be used and we obtain

$$1 + \left(\frac{1}{kD_e}\right)^2 \left\{ -\frac{(kv_{th})^2}{\omega^2} - 3\frac{(kv_{th})^4}{\omega^4} \right\} = 0 \qquad (6.11)$$

Where we have neglected the imaginary part. The solution is the familiar expression:

$$\omega^2 = \omega_p^2(1 + 3(kD_e)^2) \qquad (6.12)$$

The spectral peak associated with this oscillation is apparent in Figure 6. The peak can be strongly ennanced by the presence of photoelectrons or other suprathermal charged particles. The actual enhancement level involves the short-range Coulomb collisions as well as the angular distribution of the suprathermal electrons and the derivation must be omitted here.

Let us now briefly turn to the effect of the magnetic field. As far as the ions are concerned the gyrofrequency Ω_i satisfies the relation:

$$kV_{th} >> \Omega_i$$

This means that the correlation function

$$e^{-(kR)^2(\frac{\Omega\tau}{2})^2\cdot\cos^2\beta}$$

becomes modulated with a periodicity $T_i = 2\pi/\Omega_i$.

In practice, however, these modulations are blurred out because of the diffusion of the ions away from their deterministic orbits. Very close to perpendicularity with the magnetic field (i.e. $b = 90^o$) the spectrum may become very narrow if the radius of gyration of the electrons is so small that the electrons are prevented from participating in the fluctuations of the ions.

With a magnetic field the resonance associated with the plasma frequency becomes modified. When $\omega_p >> \Omega_e^2$, when $kR < 1$ and when β is not too close to 90^o one obtains:

$$\omega^2 = \omega_p^2(1 + 3(kD_e)^2) + \Omega_e^2\cdot\sin^2\beta \qquad (6.13)$$

An additional resonance, which can also be observed, arises because of the presence of the magnetic field:

$$\omega_h^2 = m/M + \cos^2\beta\ \Omega_e^2\cdot\omega_p^2/(\omega_p^2 + \Omega_e^2) \qquad (6.14)$$

which can be derived from cold plasma theory. When $\omega_p^2 > \Omega_e^2$ and $\beta \to 90^o$ one obtains:

$$\omega_h^2 = \Omega_e\Omega_i$$

which is sometimes referred to as the lower hybrid frequency. The strength of these lines depend on the relative magnitudes of plasma frequency and gyrofrequency, on the presence of suprathermal electrons (or ions) etc.

The total power residing in the electron plasma oscillation at thermal equilibrium is determined by integrating the spectrum through the electron lines with the result that

$$\int_{\text{electron line}}\phi\ d\omega = \frac{(kD_e)^2}{1+(kD_e)^2}$$

whereas the power in the ion line becomes:

$$\int_{\text{ion}}\phi\ d\omega = \frac{1}{(1+(kD_e)^2)\,(1+\frac{T_e}{T_i}+(kD_e)^2)}$$

Hence, whenever kD_e is small the ion contribution dominates.

CONCLUSION.

An attempt has been made in this presentation to give a simple derivation from first principles of the fluctuation phenomena which form the basis of incoherent scatter observations. No attempt has been made to discuss all the methods and all the theoretical results which have been presented in the literature. Rather, emphasis has been placed on the presentation of a self-contained model which is good enough to derive most of the commonly used results without requiring any prior knowledge of plasma physics.

REFERENCES.

1. Dougherly, J.F. and D.T. Farley, Proc. Roy. Soc. (London) A 259 (1960) 79-99.

2. Fejer, J.A. Can J. Phys. 38, (1960) 1114-1133.

3. Salpeter, E.E. Phys. Rev. 120, (1960) 1528-1535.

4. Hagfors, T. J. Geophys. Res. 66 (1961) 982-984.

5. Salpeter, E.E. J. Geophys. Res. 66 (1961) 982-984.

6. Perkins, F.W. and E.E. Salpeter, Phys. Rev. A 139, (1965) 55-62.

7. Rosenbluth, M.N. and N. Rostoker, Phys. Fluids 5 (1962) 776-788.

Scattering of E. M. Waves from Dielectric Density Fluctuations (*)

Ronald F. Woodman, Arecibo Observatory, Arecibo, P. R.

Racars are used for remote probing of the upper atmosphere. Monstatic and bi-static configurations have been used. The echoes are obtained from the scattering of the illuminating wave by fluctuations in the dielectric properties of the medium under study.

The fluctuations in the local dielectric constant of a medium are direct consequence of fluctuations in the density of the medium or more properly on the density of that component or components in the medium responsable for its dielectric behaviour, e.g. electron density in a ionized gas, "air" density and water vapor in the lower atmosphere, etc.

In the case the medium is in the thermodynamic equilibrium, the fluctuations are reduced to a minimum (thermal level). In such a case, and for a ionized plasma, we refer to the technique as Incoherent Scatter. These fluctuations are never at the zero level due to the discret nature of matter (Summations of delta functions will always produce fluctuations).

Density fluctuations are statistically characterized by the density space-time correlation function $\rho(r,\tau, \underset{\sim}{x})$ define as

$$\rho(\underset{\sim}{r},\tau; \underset{\sim}{x}) \equiv \langle n(\underset{\sim}{x},t)\, n(\underset{\sim}{x} + \underset{\sim}{r},\, t + \tau)\rangle \qquad (1)$$

where $n(\underset{\sim}{x},t)$ is the microscopic random density of the medium at position $\underset{\sim}{x}$ in space and time t. In (spatially) homogeneous medium ρ is independent of $\underset{\sim}{x}$ and $\rho(\underset{\sim}{r},\tau) \equiv \rho(\underset{\sim}{r},\tau; \underset{\sim}{x})$.

(*) Lecture presented at the M.P.I. EISCAT School, Jan. 1979, Oberstdorf, W.G.

Hagfors has treated the problem of how to find $\rho(\underset{\sim}{r}, \tau)$ for a ionized medium in thermodynamic equilibrium (or quasi-thermodynamic for the case $T_e \neq T_i$). Farley has described the different techniques for obtaining stimates of $\rho(\underset{\sim}{r}, \tau; \underset{\sim}{x})$ from the scatter echoes.

We shall develop here the functional relationship that exists between the statistical characterization of the signal received in a radar experiment and the fluctuations in the medium characterized by $\rho(\underset{\sim}{r}, \tau; \underset{\sim}{x})$. The fluctuations need not to be at the thermal level, so we are not limited to the incoherent scatter problem. We should point out that the usefulness of large radars for the study of the upper atmosphere is not limited to incoherent scatter. Proof of which is found in the large number of papers produced by the Jicamarca Observatory by studying backscatter echoes from E-region, F-region irregularities and from turbulent fluctuations in the neutral atmosphere. In fact, some smaller radars are built (STARE, SOUSSY and the TS radars) which depend on the enhanced reflectivity produced either by instabilities or turbulence. This could be the case in EISCAT when observing auroral phenomena or the effects of artificial heating. It will also be the case when studying neutral dynamics using backscatter signals from turbulent fluctuations.

Said functional relationship can be found in the literature but it is usually derived under very simplified conditions with assumptions which are not necessarily valid. The derivation is usually heuristic and in many cases difficult to assess the range of validity of the derived expressions. Such approach is, of course, useful for didactic purposes and when the purpose of the paper is on other aspects of the problem. Derived expressions in the literature are usually derived for a specific technique (out of the many described here by Farley) and for specific conditions (e.g. homogeneous media, continuous

illumination, slow varying echoes, narrow pulses etc.). We shall derive here the functional relationship between the statistical properties of the echoes and the statistical properties of the medium under very general conditions.

We shall consider an experimental configuration as depicted in figure 1.

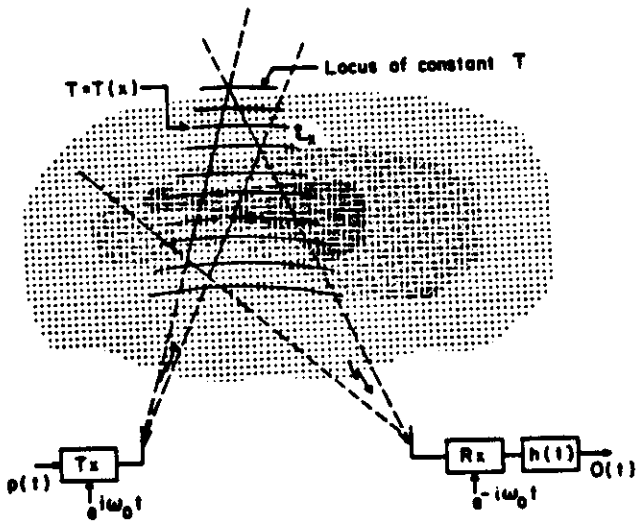

Figure 1

The medium under study is illuminated by a e.m. wave of frequency ω_o, modulated by an arbitrary complex signal p(t), scattered e.m. waves are received at a different location (or at same as a particular case), coherently detected, properly filtered and decoded (if necessary). We are interested in evaluating the complex autocorrelation of the signal received, O(t), i.e. :

$$C(\tau,t) \equiv < O(t)\ O^{*}\ (t+\tau) > \qquad (2)$$

in terms of the space and time density correlation of the medium.

The signal O(t) is a random process, usually non-stationary, is fully characterized by its time autocorrelation function $C(\tau, t)$. The dependance on t can normally be associated with a given range, h, corresponding to the delay.

We assume: (1) that there is only primary scattering (first Born approximation valid), i.e. the medium is transparent, the illuminating field at a point $\underset{\sim}{x}$ within the medium is due to the primary illuminating field and the scattered fields at $\underset{\sim}{x}$ are negligible; (2) the system is linear, i.e. if $O_1(t)$ is received for $\rho_1(t)$ and $O_2(t)$ for $\rho_2(t)$. Then $\alpha O_1(t) + \beta\ O_2(t)$ is received for a exitation $\alpha\rho_1(t) + \beta\ \rho_2(t)$. The linearity of the propagation in the medium are guaranty by the linearity of Maxwell equations.

The linearity of the system allows us to evaluate the output signal as the linear superposition of the contributions of each differential volume, $d^3\underset{\sim}{x}$ with density $n(\underset{\sim}{x},t)$. This differential contribution can be evaluated in terms of the linear operators depicted in figure 2.

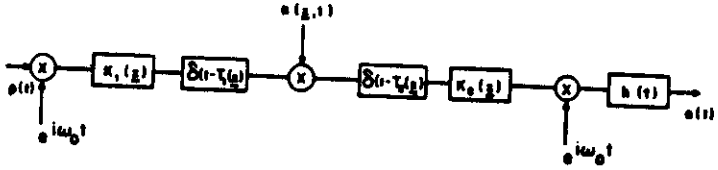

Figure 2

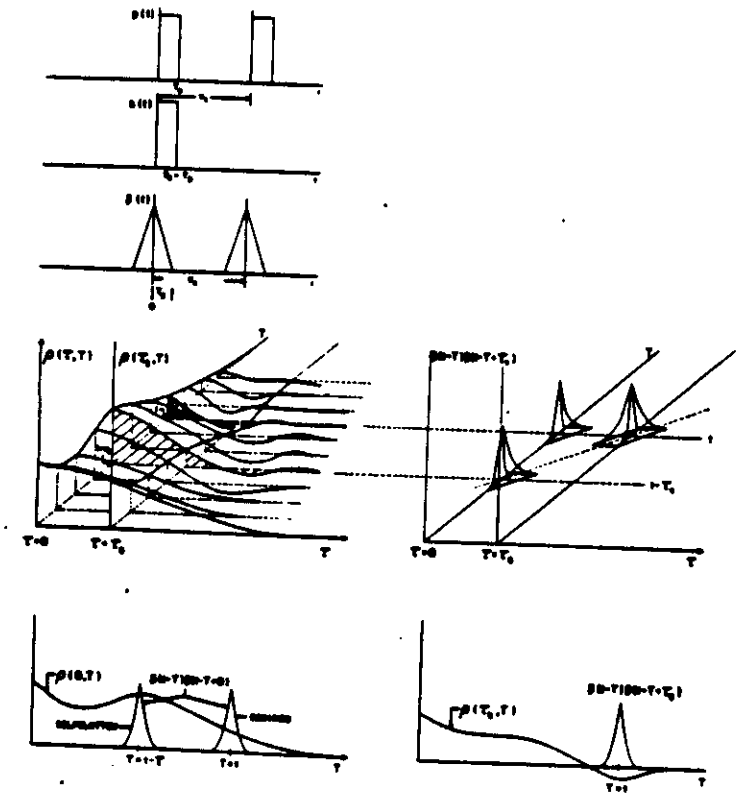

Figure 3

Here we have modelled the propagation of the transmitter to the scattering point by a delay operator with delay $T_1(\underset{\sim}{x})$ and an amplitude factor $K_1(\underset{\sim}{x})$ which represent the effect of antenna gain and other system parameters. The scattered signal is proportional to the local instantaneous (random) density $n(\underset{\sim}{x}, t)$ of the medium times the volume $d^3\underset{\sim}{x}$. The dielectric properties of the medium the receiver, antenna, and other propagation properties are contained in a constant gain (in time) $K_2(\underset{\sim}{x})$. There is a delay block with delay $T_2(\underset{\sim}{x})$, a detector and a filter before we finally get our output from the differential contribution from $n(\underset{\sim}{x}, t)$. The filter is characterized by the complex input response h(t) and includes any decoding scheme. Decoding is a convolution operation and can be considered as part of the filter.

The evaluation of the delay functions $T_1(\underset{\sim}{x})$, $T_2(\underset{\sim}{x})$ and the constant terms $K_1(x), K_2(x)$ does not concern us here and are assumed to be known. The output of the system can then be written as

$$o(t,\underset{\sim}{x})d^3\underset{\sim}{x} = d^3\underset{\sim}{x} \int dt' \; K(\underset{\sim}{x}) \; p(t' - T(\underset{\sim}{x})) \; e^{-i\underset{\sim}{w}_o T(x)} \; n(\underset{\sim}{x}, t' - T_2(\underset{\sim}{x})) \; h(t - t')$$

where we have already operated on the "signal" with the delay operators $\delta(t - T_1(\underset{\sim}{x}))$ and $\delta(t - T_2(\underset{\sim}{x}))$. Here we have used $T(\underset{\sim}{x}) = T_1(\underset{\sim}{x}) + T_2(\underset{\sim}{x})$ for the total delay and $K(\underset{\sim}{x}) = K_1(\underset{\sim}{x}) \cdot K_2(\underset{\sim}{x})$. The total signal output is then

$$O(t) = \int d^3\underset{\sim}{x} \; o(t,x) \qquad (4)$$

and the autocorrelation, $C(\tau,t) \equiv \langle O(t)\, O^*(t+\tau)\rangle$, can then be written as

$$C(\tau, t) = \int d^3\underset{\sim}{x}\, d^3\underset{\sim}{x}'dt'dt''K(\underset{\sim}{x})\, K(\underset{\sim}{x}')\, p(t' - T(\underset{\sim}{x}))\, p^*(t'' - T(\underset{\sim}{x}'))e^{-i\omega_o(T(\underset{\sim}{x}) - T(\underset{\sim}{x}'))}$$
$$h(t - t')\, h^*(t + \tau - t'')\, p(\underset{\sim}{x}' - \underset{\sim}{x},\, t''-t' - (T_2(\underset{\sim}{x}) - T_2(\underset{\sim}{x}'));\, \underset{\sim}{x}) \qquad (5)$$

It is convenient to write this expression in terms of variables

$$\underset{\sim}{r} = \underset{\sim}{x}' - \underset{\sim}{x}$$
$$\tau' = t'' - t'$$

$$C(\tau,t) = \int d^3\underset{\sim}{x}\, d^3\underset{\sim}{r}\, dt'\, d\tau'\, K(\underset{\sim}{x})\, K^*(\underset{\sim}{x}+\underset{\sim}{r})\, p(t'- T(\underset{\sim}{x}))\, p^*(t'+\tau' - T(\underset{\sim}{x}+\underset{\sim}{r}))$$
$$\cdot e^{-i\omega_o(T(\underset{\sim}{x}) - T(\underset{\sim}{x}+\underset{\sim}{r}))}\, h(t-t')\, h^*(t+\tau-t'-\tau')\, p(\underset{\sim}{r},\tau'-(T_2(\underset{\sim}{x})-T_2(\underset{\sim}{x}+\underset{\sim}{r}));\underset{\sim}{x}) \qquad (6)$$

This expression is simplified considerably if we take advantage of the fact that in most cases the characteristic length of the density correlation function, r_c , (equal to the Debye length in the I.S. case) is much smaller than the characteristic length of $K(\underset{\sim}{x})$ and the characteristic length, ct_p , corresponding to the width of the pulse $p(t)$. This allows us to replace $K(\underset{\sim}{x}+\underset{\sim}{r})$ by $K(\underset{\sim}{x})$ and $p(t - T(\underset{\sim}{x}+\underset{\sim}{r}))$ by $p(t - T(\underset{\sim}{x}))$ in the integrand with no appreciable effect on the integral.

Also, the difference in propagation time $T_2(\underset{\sim}{x}) - T_2(\underset{\sim}{x}+\underset{\sim}{r})$ is of the order of r_c/c for points within a correlated volumne. This is much smaller than the characteristic time of the decay of the correlation function unless one is dealing with relativistic plasma. Therefore we can ignore this term in the time argument of the correlation function. In addition, the oscillatory nature of the exponential, with a wavelength comparable to the wavelength of the probing wave, makes the integrant unsensitive to any possible long scale structure of the correlation function across the surfaces of constant T.

Furthermore, the almost linear behaviour of $T(\underset{\sim}{x}+\underset{\sim}{r})$ on $\underset{\sim}{r}$ for $|\underset{\sim}{r}| < r_c$ allows us to linearly expand $T(\underset{\sim}{x}+\underset{\sim}{r})$ in the exponent around $\underset{\sim}{x}$ and write:

$$\omega_o T(\underset{\sim}{x}+\underset{\sim}{r}) = \omega_o\, T(\underset{\sim}{x}) + \omega_o\, \nabla_{\underset{\sim}{r}}\, T(\underset{\sim}{x}) \cdot \underset{\sim}{r}$$
$$= \omega_o\, T(\underset{\sim}{x}) + \underset{\sim}{k}(\underset{\sim}{x}) \cdot \underset{\sim}{r} \qquad (7)$$

where $\underset{\sim}{k}(\underset{\sim}{x}) = \underset{\sim}{k}_1(\underset{\sim}{x}) - \underset{\sim}{k}_2(\underset{\sim}{x})$, and $\underset{\sim}{k}_1(\underset{\sim}{x})$ and $\underset{\sim}{k}_2(\underset{\sim}{x})$ are the local wave number of the incident and scattered wave, respectively. With this approximations we can write:

$$C(\tau,t) = \int d^3\underset{\sim}{x}\, dt'd\tau'\, K^2(\underset{\sim}{x})\, p(t' - T(\underset{\sim}{x}))\, p^*(t' + \tau' - T(\underset{\sim}{x})) \cdot$$
$$h(t - t')\, h^*(t + \tau - t' - \tau')\ \hat{\rho}\,(\underset{\sim}{k}(\underset{\sim}{x}),\tau';\, \underset{\sim}{x}) \qquad (8)$$

where $\hat{\rho}=(\underset{\sim}{\xi}, \tau; \underset{\sim}{x})$ is the spatial Fourier transform of $\rho(\underset{\sim}{r}, \tau; \underset{\sim}{x})$ defined by

$$\rho\ (\underset{\sim}{\xi},\tau;\underset{\sim}{x}) = \int d^3\underset{\sim}{r}\ e^{-i\underset{\sim}{\xi}\cdot\underset{\sim}{r}}\ \ (\underset{\sim}{r},\tau;\underset{\sim}{x}) \qquad (9)$$

Notice that as far as $\underset{\sim}{r}$ space is concerned $\underset{\sim}{x}$ can be considered as a constant parameter. Also notice that the output of the experiment depends only on the Fourier component evaluated at a particular set of wave numbers $\underset{\sim}{k}(\underset{\sim}{x})$ which for most cases is a constant. It is equal to $2\underset{\sim}{k}_1$ in the backscatter case. Equation (8) is the general expression we are after, it involves only two basic assumptions and one approximation regarding the length scale of $\rho(\underset{\sim}{r})$. It can be used as the starting point for simpler expressions applicable to the particular cases.

Next we consider a few particular cases as illustrative examples.

Case 1. Continuous exitation

In the case of a cw bi-static experiment, e.g. the French incoherent scatter radar, we have that: $p(t) = a$ where a is a constant.

In such a case the output of the experiment is time stationary and the correlation function, $C(\tau)\equiv C(\tau,t)$, is given by

$$C(\tau) = a^2\int d^3\underset{\sim}{x}\ K^2(\underset{\sim}{x})\int d\tau'\ \ \hat{\rho}(\underset{\sim}{k}(\underset{\sim}{x}),\ \tau;\ \underset{\sim}{x})\ \phi_{hh}(\tau-\tau') \qquad (10)$$

where the second integral is the usual convolution of the correlation function of the input signal to a filter by the autocorrelation function $\hat{\phi}_{hh}(\tau)$, of the filter characteristic. The spatial integral represents a weighted average of the contributions of each differential volume, weighted by the beam patterns of the antenna (and the $1/R^2$ dependance).

For homogenous media and constant $\underset{\sim}{k}(\underset{\sim}{x}) = \underset{\sim}{k}$, the spatial integral is independent of ρ and defines a volume, V, and we have

$$C(\tau) = a^2K^2\ V\int \hat{\rho}(\underset{\sim}{k},\tau)\ \phi_{hh}\ (\tau-\tau')d\tau' \qquad (11)$$

Above equations, if expressed in the frequency domain, take a even simpler form where the convolution integral is transform to a product of frequency functions.

Case 2. Filter time scale smaller than characteristic time of ρ.

In this case the integrant is different from zero for small values of the argument of $h(\cdot)$, i.e. when

$$t \simeq t'$$

$$\tau \simeq \tau' + t' - t$$

Thus, $\hat{\rho}(\underset{\sim}{k}(\underset{\sim}{x}),\tau';x)$ can be taken out of the τ' integral evaluated at $\tau' = \tau$. We can then write (8) as

$$C(\tau,t) = \int d^3\underset{\sim}{x}\ \ K^2(\underset{\sim}{x})\ \ \hat{\rho}(\underset{\sim}{k}(\underset{\sim}{x}),\tau;\underset{\sim}{x})\ \bar{p}(t-T(\underset{\sim}{x}))\,\bar{p}^*(t+\tau-T(\underset{\sim}{x})) \qquad (12)$$

where $\bar{p}$ is defined as

$$\bar{p}(t) = \int dt'p(t')h(t-t') \qquad (13)$$

that is the pulse shape passed through the filter or decoder. In optimum designs h(t) is identical to p(t), and $\bar{p}(t)$ is then the autocorrelation of the pulse shape. In multiple pulse experiments the filter is identical to a pulse element of the sequence, and $\bar{p}(t)$ is a sequence of autocorrelated pulses.

Surface of constanct delay, T = T(x), can be used as one of the variables of integration (e.g. range in a backscatter case with plane wave fronts) and a suitable set of two transverse coordinates, $\underset{\sim}{s}$, for the remaining two. We can then write:

$$d^3\underset{\sim}{x} = d^2\underset{\sim}{s}\, c\,dT \tag{14}$$

where c is the local phase velocity of light taken to be a constant for simplicity, $d^2\underset{\sim}{s}$ is a surface differential. Equation (2) takes then the form

$$C(\tau,t) = c\int d^2\underset{\sim}{s}\int dT\, K^2(\underset{\sim}{s},T)\, \hat{\rho}(\underset{\sim}{k}(\underset{\sim}{x}),\tau;\underset{\sim}{s},T)\, \bar{p}(t-T)\, \bar{p}^*(t-T+\tau)\cdot \tag{15}$$

Case 3. Backscattering from a (Quasi-) Homogeneous and Isotropic medium

This case illustrates the effect of decoding and filtering on the dependence of the autocorrelation function. The assumptions involved allow us to replace $\hat{\rho}(\underset{\sim}{k}(\underset{\sim}{x}),\tau';\underset{\sim}{x})$ by $\hat{\rho}(\underset{\sim}{k},\tau')$ and to take it out of the spatial integral. For quasi-homogeneous cases we can take $\hat{\rho}(\underset{\sim}{k},\tau;\underset{\sim}{x})$ with the value it has at the center of the volumne, which

corresponds to the particular delay t of the measurement. Therefore we will write $\hat{\rho}_t(\underset{\sim}{k},\tau')$ to extend the generality.

We can also perform the spatial integral in terms of the variables $\underset{\sim}{s}$ and T. Only $K^2(\underset{\sim}{x})$ is a function of $\underset{\sim}{s}$ and we can perform the integral with respect to this variable. If K^2 is a factor which groups all the dimensional factors in $K^2(\underset{\sim}{x})$ then the spatial integral gives us $K^2A(T)$, where A(T) is a equivalent area defined by the $\underset{\sim}{s}$ dependence of the beam pattern. On most cases of interest A(T) is a slow varing function of T, slower than the pulse length and can be taken out of the integral evaluated at the sampling delay t. Considering above we write equation (8) as

$$C(\tau,t) = cK^2A(t)\int d\tau'dt'dT\, \hat{\rho}_t(\underset{\sim}{k},\tau')\, p(t'-T)\, p^*(t'+\tau'-T)\, h(t-t')h(t+\tau-\tau'-t')$$

$$= cK^2A(t)\int d\tau'\rho_t(\underset{\sim}{k},\tau')\int dt'\, h(t-t')\, h^*(t-t'+\tau-\tau')\int dT\, p(t'-T)\, p^*(t'+\tau'-T) \tag{16}$$

or:

$$C(\tau,t) = cK^2A(t)\int d\tau'\ \hat{\rho}_t(\underset{\sim}{k},\tau')\, \phi_{pp}(\tau')\, \phi_{hh}(\tau-\tau') \tag{17}$$

where $\phi_{pp}(\tau)$ is the autocorrelation function of the pulse shape and $\phi_{hh}(\tau)$ the autocorrelation function of the filter and decoding system.

Illustrative Examples

In order to gain a better understanding of the significance of the formulas derived for case 2 and 3 we have constructed figure 3 and 4 respectively, corresponding to two often used pulse schemes. Case 1 does not need of a illustration since in this case the spectrum of the

signal received is just the product of the spectrum of the medium with the systems filter characteristics.

Figure 3 depicts the different shapes of the functions involved for a double-pulse experiment, in a backscatter mode, in which two narrow pulses are sent, τ_s appart. In this case the experiment provides information on the correlation function, $\hat{\rho}(\underset{\sim}{k},\tau)$, at only one delay, $\tau=\tau_s$, corresponding to the pulse separation. In practice the correlation function is evaluated only at this delay. To obtain the value of the correlation function at other delays, another pair of pulses is sent with the proper spacing.

Notice that $C(\tau, t)$ is different from zero only in the vecinity of τ_s, the usefull part, and in the vecinity of $\tau = 0$ corresponding to a power measurement. Such power measurement is not usefull since it contains not only the contribution from the desired height but also the "self-clutter" contribution from $t - \tau_s$, as illustrated in the two-dimentional plot of $\bar{p}(t-T)\ \bar{p}^{\dagger}(t - T + \tau)$.

Multiple pulse schemes can be illustrated in a similar fashion, the main difference being that several delays can be stimated in a single sequence and that the self-clutter is larger and coming from several different altitudes.

Figure 4, illustrates the case in which a long pulse (as compared to the medium correlation times) is sent. The receiver impulse response is narrow and considered square for the sake of simplicity. Two effects are clear from the picture, the medium correlation function is multiplied by a triangular function, $\phi_{pp}(\tau)$, and the result convolved

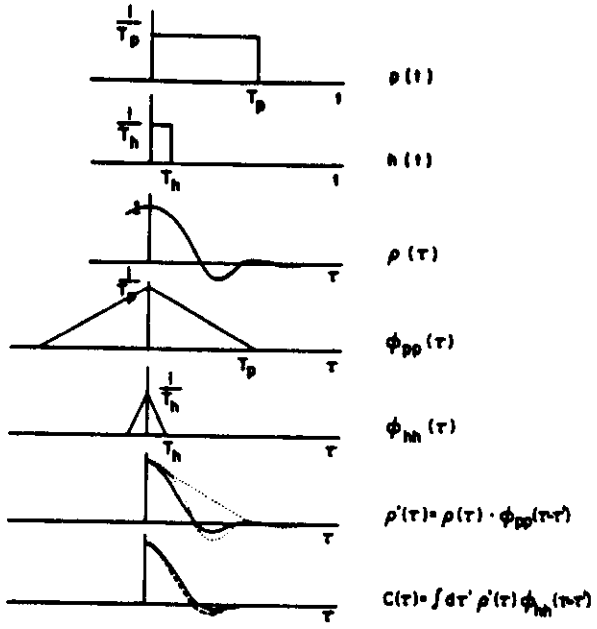

Figure 4

with a narrower function, $\phi_{hh}(\tau)$, given by the self convolution of the filter input response.

January 31, 1979

DIGITAL TECHNIQUES USED IN RADAR SCATTERING STUDIES OF THE IONOSPHERE AND ATMOSPHERE

D.T. Farley
School of Electrical Engineering, Cornell University
Ithaca, New York 14853 (USA)

In radar scattering measurements from the ionosphere or neutral atmosphere, one seeks to measure the statistical properties of one random variable, the received scattered signal, in the presence of another, the noise, which is often stronger. Depending upon the desired parameters, altitude region, necessary resolution in space and time, etc., a measurement may be limited by peak transmitter power, average power, sampling rate, or computer processing speed. Numerous digital techniques have been developed to deal with these limitations and to cope with various systematic distortions of the data. For example, long pulses can be 'compressed' by phase coding (e.g., Barker codes, or complementary code pairs for slowly varying media) to increase the effective peak power, frequency stepping can increase the average power and sampling rate without causing range ambiguity, and various coarse quantisation schemes can speed up the data processing. But pulse compression is limited by the correlation time of the medium, frequency stepping by the pulse length and receiver recovery time (and perhaps computing speed and available hardware), and coarse quantization by the decrease in effective S/N and perhaps dynamic range. In some situations it may actually pay

to widen the receiver bandwidth well beyond that of the signal, if the sampling rate and associated processing speed can be increased accordingly.

The techniques for processing wideband signals (such as incoherent scatter from the ionosphere) and narrowband signals (such as scatter from the stratosphere) are different. (Scatter from auroral plasma waves may fall in either category.) In the first case good range resolution in an extended medium is required (at least for a monostatic radar), and the only practical alternative is to measure the auto-correlation function (ACF) of the signal; in the narrowband case one normally measures the power spectrum directly via an on-line FFT of the signal samples. The latter case is straightforward, but for the former a variety of pulse schemes are possible. When range resolution is important one can transmit groups of several (the more the better) closely but unequally spaced pulses, each of which may be phase-coded (compressed). A set of n pulses can yield $n(n-1)/2$ different lags on the ACF.

The on-line digital data processing problem is not trivial since (even with the recent advent of ultra high speed array processors) computing speed is the ultimate limiting factor in some measurements. Special purpose hardware may help, and it may pay to process the data in a less than statistically optimum way if the loss of information per sample is more than compensated for by the increased number of samples processed. One-bit processing is an extreme example. With coarse quantization, even when less extreme,

sampling at greater than the Nyquist rate is generally advisable. In practice, ACF's are almost never processed completely optimally, from a statistical point of view. When the scattered signal from a slowly varying medium, such as the stratosphere, is weak, a mixture of coherent (adding voltages) and incoherent integration can sometimes ease computing requirements for spectral calculations by as much as an order of magnitude or more. For spectral measurements from the troposphere and stratosphere it may be advisable not to use a tapered windowing function on the data if the scattered signal is mixed with a very strong 'ground clutter' return at zero Doppler shift. In correcting ACF's for filter distortions it is convenient to work in the frequency domain, in which case the maximum entropy method (MEM) should be used in the transformation. However, it is even better not to correct the data, but rather to suitably distort the theoretical values before attempting to fit them to the data. The latter procedure is more expensive, however, because many corrections must be made in the course of the search for the best fit.

RADAR PROBING OF THE ATMOSPHERE

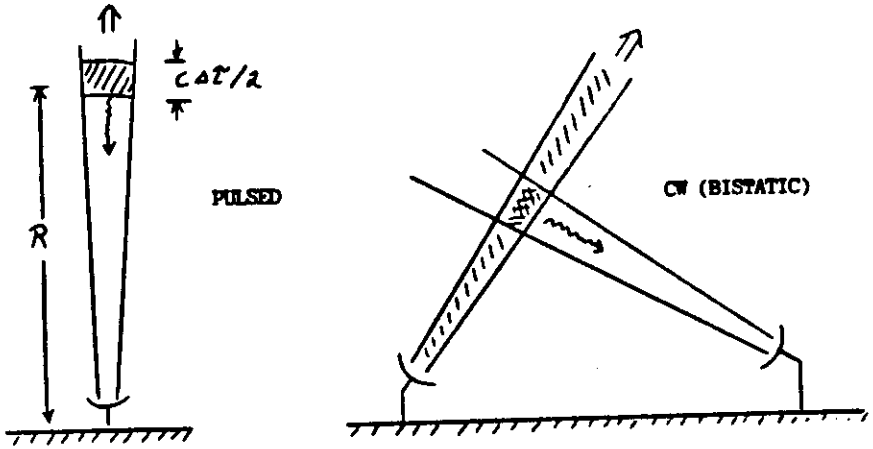

CONCENTRATE ON PULSED CASE

ASSUME TARGET IS "SOFT" (FILLS BEAM), IN WHICH CASE

$$\frac{\text{Signal}}{\text{Noise}} = \frac{P_{rec}}{k T_{syst} B_{rec}} \qquad P_{rec} \propto P_t A_{eff} \sigma(R) \Delta\tau / R^2$$

$$B_{rec} \sim \Delta\tau^{-1} \text{ (short pulse)}$$

$$\sim \Delta f_{medium} \text{ (long pulse)}$$

SCATTERED SIGNAL IS GAUSSIAN RANDOM VARIABLE (AS IS NOISE)

HOW BEST EXTRACT SIGNAL FROM NOISE AND DETERMINE STATISTICAL PROPERTIES OF SIGNAL, ESPECIALLY THE AUTO-CORRELATION FUNCTION (ACF) OR POWER SPECTRUM?

TECHNIQUES DIFFER, DEPENDING PARTICULARLY ON WHETHER MEDIUM IS VARYING SLOWLY OR RAPIDLY ("UNDERSPREAD" OR "OVERSPREAD"; NARROWBAND OR WIDEBAND SIGNAL; CORRELATION TIME LONG OR SHORT COMPARED TO INTERPULSE PERIOD

GOAL SHOULD BE TO PROCESS DATA IN REAL TIME (i.e., OUTPUT SHOULD BE $N_e(h,t)$, $T_e(h,t)$, $T_i(h,t)$ etc.)

TOPICS TO CONSIDER

1. PULSE COMPRESSION

   BARKER CODES? LONGER NON-REPETITIVE CODES?
   CYCLIC CODES (FOR BISTATIC)? COMPLEMENTARY CODE PAIRS?
   POSSIBLE PROBLEMS: GROUND CLUTTER, RANGE SIDELOBES, MEDIUM DECORRELATION

2. FREQUENCY STEPPING

   PERMITS HIGH PRF AND CAN REDUCE INTEGRATION TIME

3. COHERENT INTEGRATION (SUM VOLTAGES, NOT POWERS)

   VERY USEFUL FOR NARROWBAND SIGNALS
   SIMPLIFIES (SPEEDS) COMPUTER PROCESSING
   CAN BE INTERCHANGED WITH PULSE DECODING

4. COARSE QUANTIZATION

   PERMITS VERY HIGH SAMPLING AND PROCESSING RATES
   USUALLY REQUIRES SPECIAL PURPOSE HARDWARE
   DISADVANTAGE: CAUSES SOME INCREASE IN STATISTICAL UNCERTAINTY, BUT THIS CAN BE PARTLY OVERCOME BY OVERSAMPLING

5. ACF AND FFT TECHNIQUES

   USE OF DOUBLE AND MULTIPLE PULSES
   USE MEM IN ACF PROCESSING?
   USE TAPERED "WINDOW" IN FFT PROCESSING?

6. FARADAY ROTATION MEASUREMENTS USING INCOHERENT SCATTER

   MAIN PROBLEM IS TO COMPENSATE FOR NUMEROUS POTENTIAL SYSTEMATIC ERRORS

WIDE BANDWIDTH SIGNALS ("OVERSPREAD")

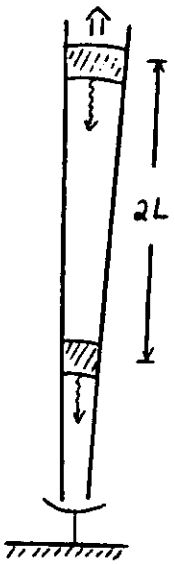

RANGE ALIASING: SIGNALS FROM h AND h + L MIXED

L = c(IPP)/2

WIDEBAND means

IPP > MEDIUM DECORRELATION TIME

PRF/2 < MAXIMUM DOPPLER SHIFT

EXAMPLES: RADAR ECHOES FROM MARS
INCOHERENT SCATTER FROM IONOSPHERE

INCOHERENT SCATTER

SCATTER FROM THERMAL FLUCTUATIONS IN PLASMA DENSITY

QUANTITATIVE THEORY WELL UNDERSTOOD

POWER SPECTRUM OF FORM

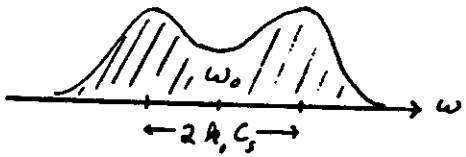

MATCH DATA TO THEORY (LEAST SQUARE FIT) TO DEDUCE PLASMA PARAMETERS (N_e, T_e, T_i, V_{drift}, etc)

MORE PRACTICAL TO MEASURE ACF THAN SPECTRUM (EXCEPT IN BISTATIC CASE)

TECHNIQUES FOR ACF MEASUREMENT

LONG SINGLE PULSE

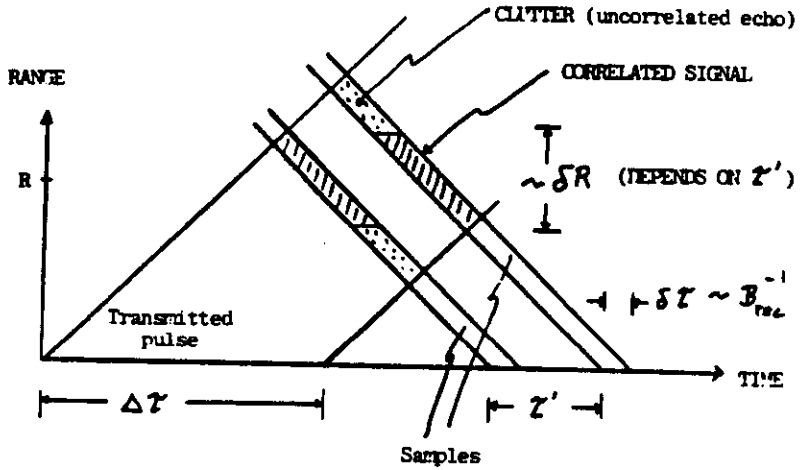

MANY SUCH PAIRS GIVE

$$\langle V(R,t)\, V^*(R, t+\tau') \rangle \longrightarrow \rho(R,\tau')$$

MEASURED ACF WEIGHTED BY TRIANGULAR FUNCTION $W = 1 - \tau'/\Delta\tau$

SO KEEP $\tau' \leq \Delta\tau/2$

δR (AND PERHAPS R) DEPENDS ON τ'

USE AT HIGH ALTITUDES WHERE TIME CONSTANTS ARE SHORT AND GOOD RANGE RESOLUTION IS NOT NEEDED

SIMILAR TO BISTATIC (CW) MEASUREMENT SINCE

B(transmitted pulse) < B(medium) = $\Delta f_{Doppler}$

ROUGHLY EQUIVALENT TO ANALYSIS WITH COMB FILTER BANK

ACF (continued)

DOUBLE OR MULTIPLE PULSE

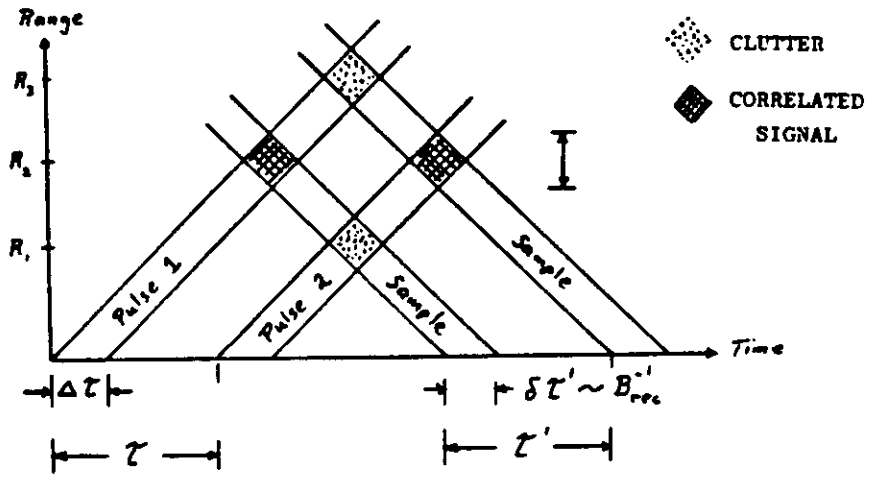

SAMPLE PRODUCTS $\rightarrow \langle V(R_2, t) V^*(R_2, t+\tau') \rangle \rightarrow \rho(R_2, \tau')$

TRANSMIT (CYCLICLY) DIFFERENT SPACINGS AND SAMPLE AT ALL RANGES TO DETERMINE COMPLETE $\rho(R, \tau')$
OR USE MULTIPLE τ, τ', AS WE SHALL SEE

GOOD RANGE AND LAG RESOLUTION POSSIBLE

CLUTTER (ECHOES FROM UNWANTED RANGES) ADDS TO NOISE

CAN HAVE $\tau \neq \tau'$ AND/OR $\Delta\tau \neq \delta\tau'$ (UNMATCHED FILTER)
BUT NOT RECOMMENDED (LIKELY TO GIVE SYSTEMATIC ERRORS)

BEST IF $\tau \geq \Delta\tau + \delta\tau'$; IF NOT, CAREFUL WITH WEIGHTING AND ALTITUDE CORRESPONDING TO SHORTEST LAG

CLUTTER ECHOES CAN BE ELIMINATED IF PULSES 1 AND 2 HAVE ORTHOGONAL POLARIZATIONS (WITH MATCHING RECEIVER SYSTEM)

ACF (continued)

HIGHLY DESIRABLE TO EXTEND THIS IDEA TO MULTIPLE PULSES

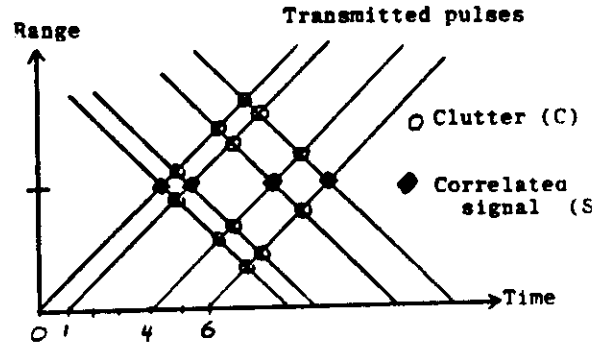

EXAMPLE: 4 PULSES AT t = 0, 1, 4, 6 PRODUCES
lags = 0, 1, 2, 3, 4, 5, 6

IN GENERAL: n PULSES $\rightarrow$ n(n-1)/2 DIFFERENT LAGS

SOME "MISSING" LAGS FOR n > 4

CLUTTER POWER $\sim$ (n-1) x SIGNAL POWER

SAME ADVICE AS IN DOUBLE PULSE CASE FOR
τ vs τ', $\Delta\tau$ vs $\delta\tau'$, τ vs $\Delta\tau + \delta\tau'$

BEST TO MAKE n AS LARGE AS POSSIBLE, CONSISTENT WITH THE VARIOUS CONSTRAINTS OF PULSE LENGTH, ETC., IF COMPUTER CAN HANDLE THE INCREASED PROCESSING. OR USE FREQUENCY STEPPING? (SEE LATER)

STATISTICS IMPROVE EVEN THOUGH CLUTTER INCREASES —
ESPECIALLY IF S/N $\ll$ 1 AND HENCE C $\lesssim$ N

CANNOT USE ORTHOGONAL POLARIZATION TECHNIQUE TO ELIMINATE CLUTTER

CANNOT USE MULTIPLE FREQUENCIES OR ORTHOGONAL CODES EITHER (ELIMINATES CLUTTER, BUT ALSO SIGNAL!)

SAME IDEA USED IN "NON-REDUNDANT" ANTENNA ARRAYS FOR APERTURE SYNTHESIS. SOME REDUNDANCY OK IN ANTENNA ARRAY CASE, BUT NOT FOR RADAR ACF MEASUREMENT (GIVES RANGE ALIASING)

ACF'S - ADDITIONAL COMMENTS

RESOLUTION: IN GENERAL

ALTITUDE RESOLUTION DETERMINED BY

PULSE DURATION OR B_{rec}^{-1}, WHICHEVER IS LARGER

LAG RESOLUTION IS APPROXIMATELY

PULSE DURATION OR B_{rec}^{-1}, WHICHEVER IS SMALLER

MEASURE ONLY A FEW LAGS?

MEASURING ONLY A SINGLE LAG IN THE (COMPLEX) ACF IS SUFFICIENT TO DETERMINE THE FIRST MOMENT OF THE DOPPLER SPECTRUM, AND HENCE THE MEAN DRIFT (IF YOU KNOW THE SHAPE OF THE SPECTRUM)

SIMILARLY, TWO LAGS WILL GIVE THE FIRST TWO MOMENTS, ETC

CHOOSING TECHNIQUE; OPTIMIZING

USUALLY BEST TO ASSUME S/N << 1, SINCE IN OPPOSITE LIMIT THERE ARE GENERALLY NO PROBLEMS EVEN IF MEASUREMENT IS NOT OPTIMUM

PULSE COMPRESSION

IDEAL CASE

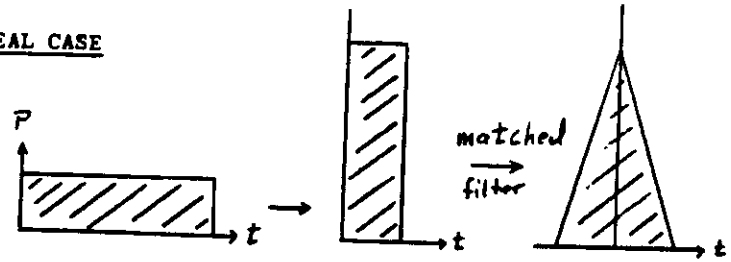

CAN USE FREQUENCY "CHIRPING" OR PHASE CODING

IN PRACTICE USE BINARY PHASE CODING; DECODE WITH COMPUTER OR SPECIAL PURPOSE DIGITAL OR ANALOG DEVICES

BARKER CODES

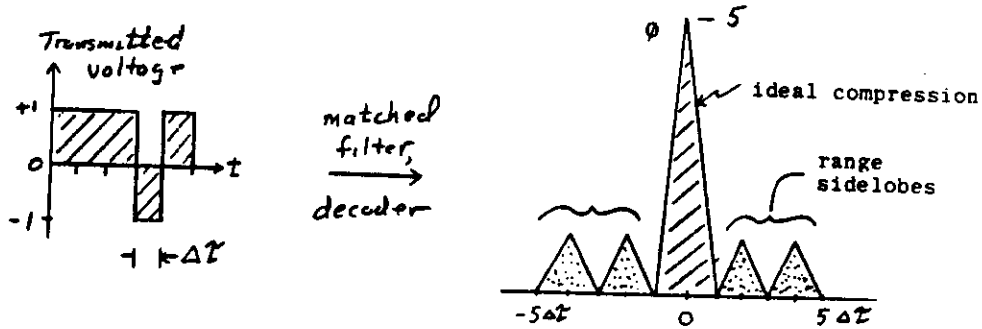

φ = AMBIGUITY FUNCTION (FOR NO DOPPLER)
= VOLTAGE FROM SMALL STATIONARY TARGET
= ACF OF CODE

TARGET MUST REMAIN COHERENT FOR $n\Delta\tau$ (UNCOMPRESSED DURATION)

GROUND CLUTTER DURATION $\gtrsim$ UNCOMPRESSED PULSE

MAX COMPRESSION WITH BARKER CODE (UNITY SIDELOBES) IS 13:1

OTHER LONGER SIMILAR NON-CYCLIC CODES AVAILABLE

e.g., $n = 28 \longrightarrow$ MAX SIDELOBE OF 2

COMPRESSION (continued)

CYCLIC CODES WITH $n = 2^p - 1$ AND CYCLIC AMBIGUITY FUNCTIONS USEFUL FOR BISTATIC CASE AND RADAR ASTRONOMY SINCE

a) LARGE CYCLIC RANGE SIDELOBES CAUSE NO PROBLEM
b) SIDELOBES BETWEEN MAIN PEAKS HAVE UNITY AMPLITUDE
(n:1 compression ratio)

MULTIPLE CODED PULSES FOR ACF?

USE DOUBLE OR MULTIPLE BARKER CODED PULSES? YES
IMPROVES RANGE RESOLUTION BY COMPRESSION FACTOR
USUALLY IMPROVES TIME DELAY (LAG) RESOLUTION BY SAME AMOUNT
(DOESN'T FOR THIN TARGET)
BUT MAY PUT RESTRICTIONS ON MEASURABLE LAGS SINCE MINIMUM SPACING SHOULD BE $\geq 2 \times$ DURATION OF UNCOMPRESSED PULSE

e.g., TRANSMIT

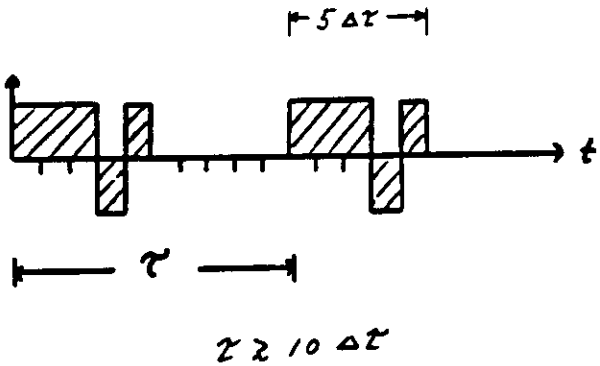

COMPLEMENTARY CODE PAIRS?

VERY USEFUL FOR SUFFICIENTLY NARROWBAND SIGNALS (DISCUSSED LATER)

FREQUENCY STEPPING

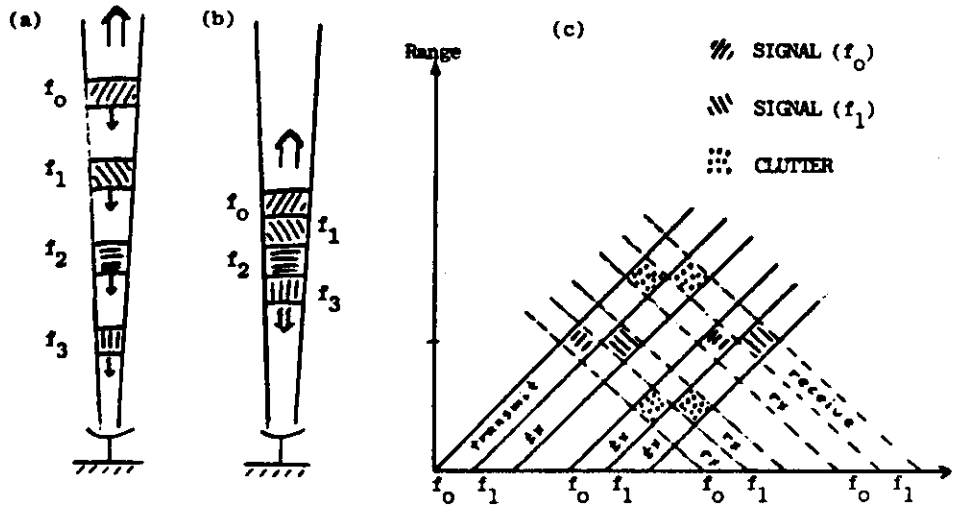

(a) AND (b) ILLUSTRATE 2 WAYS OF MAKING RAPID POWER PROFILES. SCATTERED SIGNALS AT THE DIFFERENT FREQUENCIES ARE UNCORRELATE AND HENCE GIVE INDEPENDENT SAMPLES. USEFUL WHEN $S/N \gtrsim 1$

PICKING CLOSELY SPACED FREQUENCIES IN CASE (b) CORRESPONDS TO PULSE COMPRESSION (CHIRPING) IF DATA IS PROCESSED APPROPRIATELY. USEFUL IF $S/N << 1$

(c) ILLUSTRATES THE USE OF FREQUENCY STEPPING IN AN ACF MEASUREMENT EFFECTIVE SAMPLING RATE IS INCREASED; INTEGRATION TIME IS REDUCED. CAN BE EXTENDED IN AN OBVIOUS WAY TO MULTIPLE PULSES (LAGS) AND/OR MULTIPLE FREQUENCIES.

FREQUENCY STEPPING MAY ALLOW MORE EFFECTIVE USE OF THE AVERAGE POWER CAPABILITIES OF THE TRANSMITTER. REQUIRES SIMULTANEOUS RECEPTION ON MULTIPLE RECEIVERS FOR MAXIMUM EFFECTIVENESS. PARTICULARLY APPROPRIATE WHEN $S/N \gtrsim 1$. PULSE COMPRESSION USUALLY BETTER IN THE OPPOSITE LIMIT.

COARSE QUANTIZATION

PERMITS VERY FAST SAMPLING AND ACF PROCESSING WITH SIMPLE SPECIAL PURPOSE HARDWARE (MANY PARALLEL CHANNELS)

USEFUL FOR VERY WIDE BANDWIDTH SIGNALS

INCREASES STATISTICAL UNCERTAINTY PER SAMPLE SOMEWHAT, BUT SAMPLING RATES ARE GREATLY INCREASED

OVERSAMPLING (> NYQUIST RATE) WILL REDUCE STATISTICAL UNCERTAINTY

ACF MAY BE SLIGHTLY DISTORTED, BUT CORRECTIONS ARE SIMPLE

POWER INFORMATION MAY BE LOST (UNLESS S/N << 1)

OUTPERFORMS ARRAY PROCESSOR SYSTEMS (167 ns mult-add time) FOR SOME APPLICATIONS (e.g., SINGLE PULSE HIGH ALTITUDE ACF)

USING WIDER BANDWIDTH THAN NECESSARY MAY REDUCE FILTER DISTORTIONS. INCREASING BANDWIDTH CAUSES NO LOSS OF STATISTICAL ACCURACY IF SAMPLING AND PROCESSING RATES CAN BE INCREASED TO MATCH

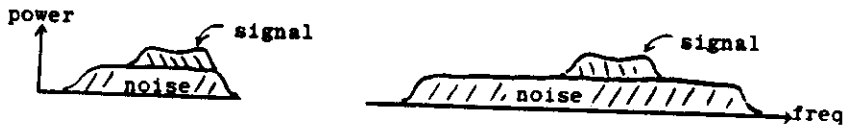

EXAMPLES: 1-bit x multi-bit (NO DISTORTION, RETAINS POWER INFO)

3-level x 3-level (+1, 0, -1)

1-bit x 1-bit (+1, -1)

LAST REQUIRES 1.6-2.5 TIMES MORE INTEGRATION TIME THAN FULL MULTI-BIT x MULTI-BIT

INCOHERENT SCATTER DATA ANALYSIS

MEASUREMENT

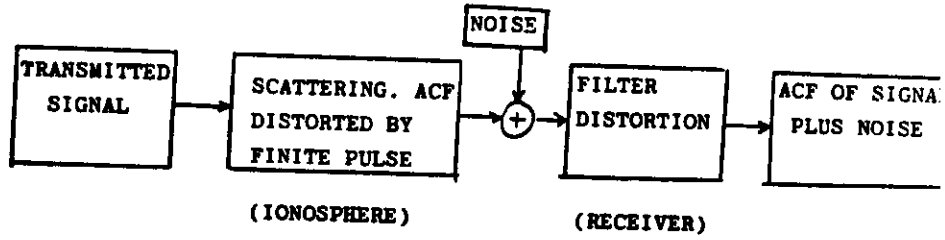

CORRECT DATA, THEN ANALYZE?

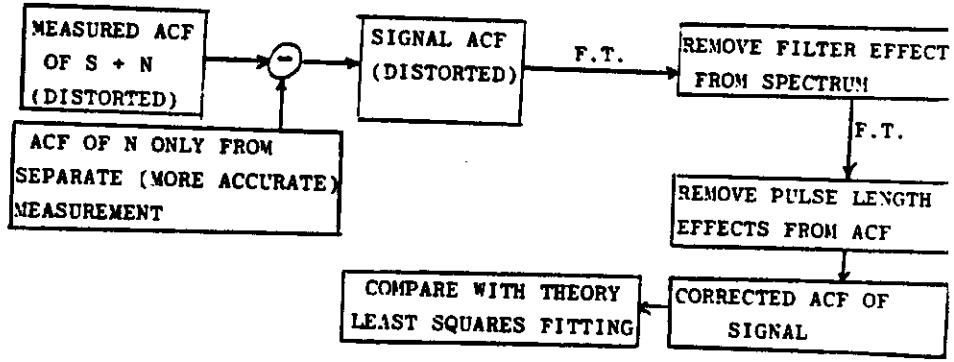

DIFFICULTIES WITH THIS PROCEDURE:

DISCRETE FOURIER TRANSFORMS (FT)
TRUNCATED ACF'S
MISSING LAGS IN ACF?
ERRORS WHICH VARY WITH LAG?

USE OF MAXIMUM ENTROPY METHOD (MEM) HELPS, BUT BETTER STILL TO USE DIFFERENT APPROACH

ANALYSIS (continued)

BETTER IDEA: LEAVE DATA ALONE (AND DISTORTED)
CORRECT (DISTORT) THEORY TO MATCH

REQUIRES MORE COMPUTING, BUT SINCE THEORY HAS NO ERROR, NO GAPS
NO TRUNCATION, THERE ARE NO PROBLEMS WITH TRANSFORMS

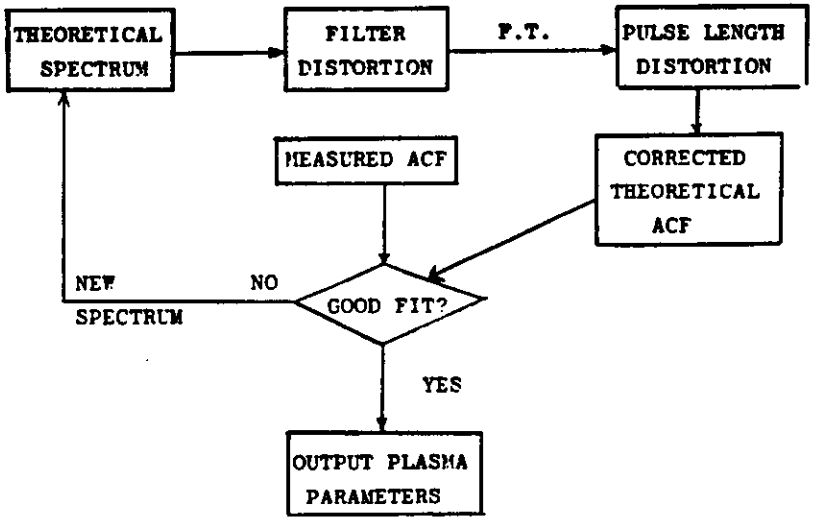

ADDITIONAL POINT ON DATA PROCESSING:

QUANTIZATION NOISE ~ ½ BIT AND IS USUALLY NEGLIGIBLE, SO DON'T USE TOO MANY BITS (SLOWS COMPUTING). NOTE THAT 7 BITS + SIGN GIVES MORE THAN 40 dB OF DYNAMIC RANGE, WHICH SHOULD BE MORE THAN ENOUGH. GOOD RESULTS CAN BE OBTAINED WITH ONLY 1 BIT!

PROCESSING AND ANALYSIS GOAL:

COMPLETE ANALYSIS AND REDUCTION TO PLASMA PARAMETERS IN REAL TIME IF POSSIBLE. SAVES TIME; SAVES STORAGE; ALLOWS (POSSIBLY AUTOMATIC?) RADAR ADJUSTMENT TO OPTIMIZE DATA COLLECTION

FARADAY ROTATION MEASUREMENTS USING INCOHERENT SCATTER

AT PROPER FREQUENCY CAN BE VERY USEFUL SINCE ROTATION RATE GIVES THE ABSOLUTE ELECTRON DENSITY PROFILE CONVENIENTLY

$$dR/dh \propto B f^{-2} \cos\theta N(h)$$

IF FREQUENCY IS TOO HIGH, GET LITTLE ROTATION AND LOSE SENSITIVITY

BUT IF FREQUENCY IS TOO LOW, CAN GET TOO MUCH ROTATION
(FARADAY DISPERSION - SUBSTANTIAL ROTATION WITHIN PULSE LENGTH

ALSO, MANY POTENTIAL SYSTEMATIC ERRORS, BUT ALL CAN BE COMPENSATED FOR, AS AT JICAMARCA

NARROWBAND ("UNDERSPREAD") SIGNALS

MAXIMUM DOPPLER < OR << ½ PRF
MEDIUM CORRELATION TIME > OR >> INTERPULSE PERIOD (IPP)

PULSE-TO-PULSE CORRELATION EXISTS

FFT PROCESSING MOST CONVENIENT

EXAMPLES

SCATTER FROM IONOSPHERIC PLASMA INSTABILITIES (AURORA)
(MAY BE UNDER OR OVERSPREAD)

SCATTER FROM TURBULENCE IN TROPOSPHERE, STRATOSPHERE, AND MESOSPHERE

TWO ADDITIONAL TECHNIQUES NOW AVAILABLE:

1. PULSE COMPRESSION USING COMPLEMENTARY CODE PAIRS GIVES HIGH COMPRESSION RATIOS WITH NO NEARBY RANGE SIDELOBES
2. COHERENT INTEGRATION (SUMMING VOLTAGE RETURNS, NOT POWERS, FROM SUCCESSIVE PULSES) CAN GREATLY SIMPLIFY COMPUTER PROCESSING

COMPLEMENTARY CODES

BASIC IDEA:

TRANSMITTED SEQUENCE
(4:1 COMPRESSION)

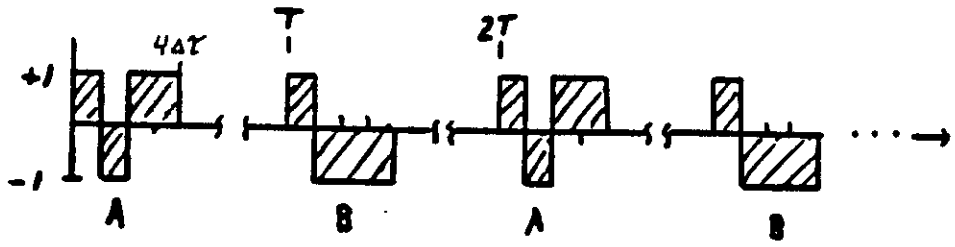

DECODE BY CROSS-CORRELATING WITH A,B TO GIVE

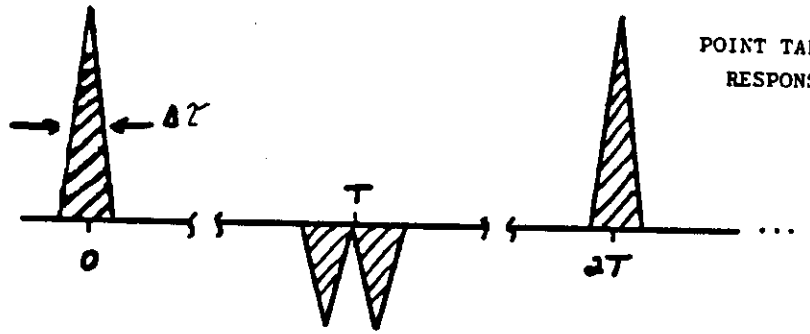

POINT TARGET
RESPONSE

NO NEARBY RANGE SIDELOBES (BETTER EVEN THAN BARKER CODE)
CAN BE IMPORTANT IN TROPOSPHERE-STRATOSPHERE MEASUREMENTS WHERE SIGNAL STRENGTH FALLS OFF 2-3 dB/km

ONLY WORKS IF ECHO MAINTAINS COHERENCE OVER TIME >> T
(vs $n\Delta\tau$ FOR BARKER CODE)

RANGE SIDELOBES (AMBIGUITY) AT ~ T, 2T, ETC
NOT A PROBLEM IF ECHOES FROM CORRESPONDING RANGES ARE WEAK OR DO NOT MAINTAIN REQUIRED COHERENCE

COMPLEMENTARY CODE PAIRS (OFTEN SEVERAL) EXIST FOR
n = 2, 4 (example shown), 8, 10, 16, 20, 32, 40, ...

COMPLEMENTARY CODES (continued)

MORE ELABORATE SCHEME:

TRANSMIT $A,B,A,\bar{B},A,B,A,\bar{B},\ldots$

DECODE BY CROSS-CORRELATING WITH $A,B,A,\bar{B}$ TO GIVE SINGLE PEAK AT 0 AND FIRST SIDELOBE AT $2T-(n-1)\Delta\tau$

OR CROSS-CORRELATE WITH $B,A,\bar{B},A$ TO GIVE SINGLE PEAK AT T AND FIRST SIDELOBE AT $3T-(n-1)\Delta\tau$

EXAMPLE (n=2)

TRANSMIT

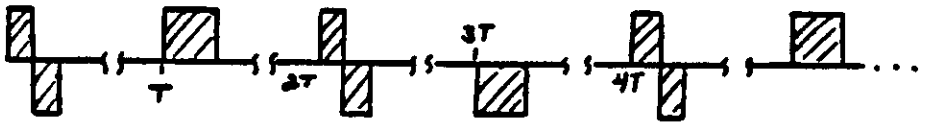

DECODED POINT TARGET RESPONSE

ALTERNATE DECODING

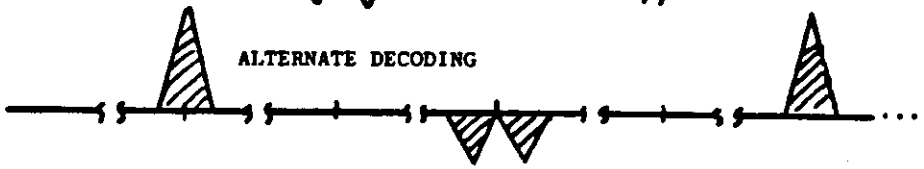

COMPLEMENTARY CODES (continued)

EXTENDING THIS IDEA WILL PUSH THE FIRST RANGE SIDELOBE OUT TO 3T OR BEYOND. FOR EXAMPLE

$A,B,A,\bar{B},A,B,\bar{A},B,A,B,A,\bar{B},\ldots$ → FIRST SIDELOBE AT $\sim 3T$

CAN BE USEFUL TO MAKE SEQUENCE SYMMETRIC (EQUAL NUMBER OF +1's AND -1's

AUTOMATICALLY ELIMINATES DC DUE TO RECEIVER AND/OR DIGITIZER BIAS

POSSIBLE FOR

$A,B,A,B,\ldots$	n=4, 16, 64,...
$A,B,A,\bar{B},A,B,\ldots$	n=2, 8, 32,....
$A,B,A,\bar{B},A,B,\bar{A},B,A,B,\ldots$	n=4, 16, 64,...

NOTE THAT IT MAY BE POSSIBLE TO COHERENTLY INTEGRATE (SUM VOLTAGES) MANY SAMPLES BEFORE DECODING (IF MEDIUM COHERENCE TIME IS LONG ENOUGH), THEREBY SAVING MANY COMPUTATIONS

ANOTHER POSSIBLY USEFUL IDEA:

TRANSMIT A AND B SIMULTANEOUSLY ON ORTHOGONAL POLARIZATIONS (IF TRANSMITTER WILL PERMIT). MEDIUM MUST THEN REMAIN CORRELATED ONLY FOR LENGTH OF UNCOMPRESSED PULSE, NOT INTERPULSE PERIOD

BETTER THAN BARKER CODE: NO RANGE SIDELOBES
NO LIMIT TO COMPRESSION RATIO

NARROWBAND SCATTER AND DETECTABILITY

IT CAN BE SHOWN THAT, FOR A QUASI-COHERENT TARGET, PULSE COMPRESSION, COHERENT INTEGRATION, SPECTRAL PROCESSING, ETC. ENTER INTO THE DETECTABILITY (DEFINED AS THE RMS FRACTIONAL ERROR IN THE SIGNAL POWER ESTIMATE) ONLY THROUGH THE TERM

$$(\Delta R)(P_{av})$$

THE PRODUCT OF THE RANGE RESOLUTION AND AVERAGE TRANSMITTER POWER

IN OTHER WORDS, LONG HIGHLY COMPRESSED PULSES AT A LOW PRF GIVE THE SAME RESULTS AS UNCOMPRESSED OR SLIGHTLY COMPRESSED PULSES AT A HIGH PRF. (THIS IS NOT TRUE FOR INCOHERENT SCATTER, REMEMBER)

OPTIMUM CHOICE DEPENDS ON PRACTICAL DETAILS SUCH AS

- IMPORTANCE OF GROUND CLUTTER
- RANGE AMBIGUITY PROBLEMS
- RANGE GAPS DUE TO RECEIVER CUTOFF ("DEAD" TIME DURING WHICH RECEPTION IS IMPOSSIBLE)
- COMPUTER LIMITATIONS
- TRANSMITTER LIMITATIONS

SPECTRAL ANALYSIS AND WINDOWING

NO TAPERING OF DATA BLOCKS IN TIME SERIES BEFORE FFT

⟶ SPECTRUM CONVOLVED WITH SIN X/X FUNCTION

BUT THIS FUNCTION HAS ZEROS AT FREQUENCIES EQUAL TO THE FREQUENCY STEPS IN THE SAMPLED SPECTRUM; HENCE RESPONSE AT EXACTLY ZERO DOPPLER (e.g., GROUND CULTTER) IS NOT BROADENED

FIRST MAX (AT 1.5 FREQUENCY STEPS) IS DOWN BY 13.5 dB - OFTEN GOOD ENOUGH

MAY BE ADVISABLE TO USE TAPERED WINDOW IN SOME CASES, HOWEVER. GROUND CLUTTER MAY HAVE APPRECIABLE SPECTRAL WIDTH

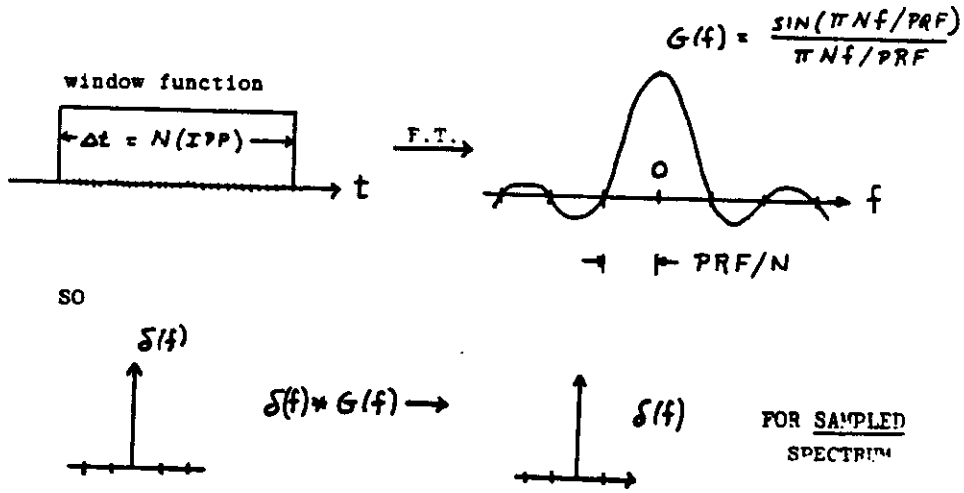

NOT RELEVANT, HOWEVER, WHEN GROUND CLUTTER APPRECIABLY BROADENED BY ATMOSPHERIC FLUCTUATIONS

SUMMARY

TOPIC	WIDEBAND SIGNALS (INCOHERENT SCATTER)	NARROWBAND SIGNALS (TROPOSPHERE ETC SCATTER)
PULSE COMPRESSION (PHASE CODES)	BARKER 28 BIT CYCLIC COMPLEMENTARY CODES ON ORTHOG. POLARIZ.? *EXTENDS GROUND CLUTTER*	COMPLEMENTARY CODE PAIRS AND MORE ELABORATE SCHEMES BASED ON THESE USEFUL ALSO FOR BISTATIC FOR VERY GOOD RANGE RESOLUTION *EXTENDS GROUND CLUTTER*
ACF MEASUREMENT	SINGLE PULSE DOUBLE PULSE DOUBLE PULSE (O & X) MULTIPLE PULSES *CAREFUL WITH PULSE SPACINGS, SAMPLING INTERVALS, FILTERS IN MULTIPULSE CASE*	POSSIBLE, BUT SINCE HAVE PULSE-TO-PULSE CORRELATION, EASIER TO CALCULATE FFT
FFT	NOT POSSIBLE SINCE NO PULSE-TO-PULSE CORRELATION (OVERSPREAD)	STRAIGHTFORWARD FFT USING SUCCESSIVE SAMPLES FROM EACH ALTITUDE TAPER DATA BLOCKS?
FARADAY ROTATION	GIVES ABSOLUTE N(h) CHOOSE PROPER FREQUENCY SPECIAL SCHEMES TO AVOID SYSTEMATIC ERRORS	
FREQUENCY STEPPING	COMBINE WITH POWER, ACF, OR FFT MEASUREMENT TO REDUCE INTEGRATION TIME WHEN S/N $\gtrsim$ 1. MULTIPLE RECEIVERS	
COHERENT INTEGRATION	NOT POSSIBLE	GREATLY REDUCES COMPUTER PROCESSING INTERCHANGE WITH PHASE DECODING?

	WIDEBAND	NARROWBAND
DATA ANALYSIS	DISTORT THEORY RATHER THAN CORRECT MEASURED ACF BEFORE FITTING FOR HIGHEST ACCURACY *MORE COMPUTING REQUIRED*	NO COMPARABLE THEORY FOR DETAILED COMPARISON
QUANTIZATION	8 BITS USUALLY PLENTY. MUCH INFORMATION CAN BE OBTAINED EVEN IN "HARD LIMITED" (1 BIT) CASE. OVERSAMPLING WORTHWHILE WHEN ONLY 1 OR 2 BITS USED	

SOME SELECTED REFERENCES

General

Evans, J.V., Theory and practice of ionosphere study by Thomson scatter radar, PIEEE, 57, 496-530, 1969.

Evans, J.V., and T. Hagfors (eds.), Radar Astronomy, McGraw Hill, 1968.

Farley, D.T., Radio wave scattering from the ionosphere, Chpt 14 in Methods of Experimental Physics: Volume 9B (R. Lovberg and H. Grien, eds.), Academic Press, 1971.

Incoherent Scatter ACF Measurements

Austin, G.L., Pulse compression systems for use with meteorological radars, Radio Sci., 9, 29-33, 1974.

Farley, D.T., Mulitple pulse incoherent scatter correlation function measurements, Radio Sci., 7(6), 661-666, 1972

Hagen, J.B., and D.T. Farley, Digital correlation techniques in radio science, Radio Sci., 9(8,9), 775-784, 1973.

Moffet, A.T., Minimum redundancy linear arrays, IEEE Trans. Ant. Prop., AP-16, 172-175, 1968.

Rino, C.L., M.J. Baron, G.H. Burch, and O. de la Beaujardiere, A multiple correlator design for incoherent scatter radar, Radio Sci., 9, 1117-1127, 1974.

Woodman, R.F., and T. Hagfors, Methods for the measurement of vertical ionospheric motions near the magnetic equator by incoherent scatter, J. Geophys. Res., 74, 1205-1212, 1969.

Zamlutti, C.J., and D.T. Farley, Incoherent scatter multiple-pulse measurements at Arecibo, Radio Sci., 10, 573-580, 1975.

Faraday Rotation Using IS

Farley, D.T., Faraday rotation measurements using incoherent scatter, Radio Sci., 4, 143-152, 1969.

Pulse Compression

Cook, C.E., and M. Bernfeld, Radar Signals, Academic Press, 1967.

Ioannidis, G., and D.T. Farley, Incoherent scatter observations at Arecibo using compressed pulses, Radio Science, 7, 763-766, 1972.

Golay, M.J.E., Complementary series, IRE Trans. Info Th., IT-7, 82-87, 1961.

Gray, R.W., and D.T. Farley, Theory of incoherent scatter measurements using phase-coded pulses, Radio Sci., 8, 123-131, 1973.

Rabiner, L.R., and B. Gold, Theory and Application of Digital Signal Processing, Prentice-Hall, 1975.

Analysis

Bergland, G.D., A guided tour of the fast Fourier transform, IEEE Spectrum, 6, 41-52, 1969.

Morris, L.R., A comparative study of time efficient FFT and WFTA programs for general purpose computers, IEEE Trans. Ac. Speech Sig. Proc., ASSP-26, 141, 1978.

Swartz, W.E., Analytic partial derivatives for least-squares fitting incoherent scatter data, Radio Sci., 13, 581-589, 1978.